VILNIUS UNIVERSITY
CENTER FOR PHYSICAL SCIENCES AND TECHNOLOGY

DAINIUS PAVILONIS

MAGNETORESISTANCE AND ELECTRICAL RESISTANCE RELAXATION IN La-Sr(Ca)-Mn-O NANOSTRUCTURED FILMS

Doctoral dissertation
Physical sciences, physics (02P)

Vilnius, 2017

The dissertation work was carried out at Center for Physical Sciences and Technology from 2012 to 2016.

Scientific supervisor - prof. dr. Nerija Žurauskienė (Center for Physical Sciences and Technology, physical sciences, physics - 02P)

VILNIAUS UNIVERSITETAS
FIZINIŲ IR TECHNOLOGIJOS MOKSLŲ CENTRAS

DAINIUS PAVILONIS

NANOSTRUKTŪRIZUOTŲ La-Sr(Ca)-Mn-O SLUOKSNIŲ MAGNETOVARŽA IR ELEKTRINĖS VARŽOS RELAKSACIJA

Daktaro disertacija
Fiziniai mokslai, fizika (02P)

Vilnius, 2017 metai

Disertacija rengta 2012 - 2016 metais Fizinių ir technologijos mokslų centre.

Mokslinė vadovė - prof. dr. Nerija Žurauskienė (Vilniaus universitetas, fiziniai mokslai, fizika - 02P)

Acknowledgements

Unquestionably, the first and foremost acknowledgement goes to my scientific supervisor Nerija Žurauskienė for devotion and help in preparing this dissertation.

Grateful I am to colleagues Saulius Balevičius, Voitech Stankevič, Skirmantas Keršulis, Česlovas Šimkevičius, Tomaš Stankevič, Valentina Plaušinaitienė, Jurij Novickij, Algirdas Matulis.

Unrivalled thanks go to my family – Gitana and Austėja. Parents – Kęstutis and Danguolė. Sister Giedrė.

Special thanks to colleagues at Bentley Systems – Diann Laracy, Martin Patton, Dalia Jasiniauskienė, Edita Kemzūraitė.

Thanks to Kęstutis Arlauskas and Bonifacas Vengalis for review of this dissertation.

Usual thanks to the Universe for letting me to get to this point of life.

In the end, I am thankful to all those not mentioned here, who also played their part in making this dissertation a reality.

Dainius Pavilonis
Vilnius
6th November 2017

Table of Contents

List of abbreviations

AF	Antiferromagnetic
AFM	Atomic Force Microscopy
CI	Canted Antiferromagnetic Insulator
CMR	Colossal Magnetoresistance
DE	Double Exchange
EDS	Energy Dispersive X-ray Spectroscopy
FI	Ferromagnetic Insulator
FM	Ferromagnetic Metal
GB	Grain Boundary
GIXRD	Grazing incidence X-Ray Diffraction
HFMR	High-Field Magnetoresistance
IACS	International Annealed Copper Standard
KAF	Kolmogorov–Avrami–Fatuzzo
KA	Kolmogorov–Avrami
KWW	Kohlrausch–Williams–Watts
LCMO	**or La-Ca-Mn-O** $La_{1-x}Ca_xMnO_3$
LFMR	Low-Field Magnetoresistance
LSMO	**or La-Sr-Mn-O** $La_{1-x}Sr_xMnO_3$
MEMS	Microelectromechanical system
MOCVD	Metal Organic Chemical Vapour Deposition
MRA	Magnetoresistance anisotropy
MR	Magnetoresistance
NTC	Negative temperature coefficient
PI	Paramagnetic Insulator
PM	Paramagnetic Metal
RF	Relaxation function
RHEED	Reflection High-Energy Electron Diffraction

SEM	Scanning Electron Microscopy
TEM	Transmission Electron Microscopy
UTS	Ultimate tensile strength
VRH	Variable range hopping

Chapter 1

Introduction

During the past few decades, the interest in polycrystalline lanthanum manganite films has increased because of fundamental understanding of colossal magnetoresistance (CMR) as well as due to potential device applications. Thin polycrystalline manganite films governing the CMR effect are perspective for application of high pulsed magnetic field (up to megagauss) measurements [1]. These applications require fast response and it is important to avoid the performance limiting effects of magnetic nature. Recent research has demonstrated that chemical composition and doping levels of manganite material have high impact on resistivity and magnetoresistance values as well as on relaxation and recovery times after film is affected by magnetic field. The purpose of this thesis is to investigate magnetoresistance and relaxation of electrical resistance and magnetic memory effects of nanostructured $\mathrm{La_{1-x}Sr_xMnO_3}$ and $\mathrm{La_{1-x}Ca_xMnO_3}$ films deposited using Pulsed injection MOCVD technique in wide temperature range and to determine the plausible mechanisms limiting the performance of sensor type applications.

Motivation and problem formulation of the work. Recently, it has been demonstrated that specially grown nanostructured (nano-grained polycrystalline) $\mathrm{La_{1-x}Sr_xMnO_3}$ (LSMO) films can be successfully used for the development of so called CMR-B-scalar sensors [2, 3]. These sensors allow for measurements of absolute magnitude of magnetic flux density B during high magnetic field pulses in the time scale of micro-milliseconds at room temperature. They were used to measure the magnetic diffusion processes and B-field dynamics during railgun launch [4, 5] and the distribution of transient magnetic fields in non-destructive dual-coil pulsed-field magnets [6]. However, for plasma science, condensed matter physics and other special applications sensors operating at cryogenic temperatures in the time scale of micro-milliseconds are required to measure magnetic fields in a wide range of amplitudes (0.1–100 T). In such cases, it is important to achieve high sensitivity and to avoid or minimize the magnetic memory effects which limit the speed of such sensors.

It was demonstrated that polycrystalline films reveal high magnetoresistance values in a wide temperature range down from paramagnetic-ferromagnetic phase transition temperature T_C to low temperatures. However, the highest MR values usually are obtained close to T_C. Therefore, for low temperature applications it is important to find out the chemical composition of the manganite films which have lower T_C in comparison with the LSMO ones and still not very high resistivity values for appropriate device operation.

In manganite films the memory effects are related to magnetization relaxation of these films upon removal or reversal of the external magnetic field. The numerous investigations of these processes proposed to use different mathematical expressions which can characterize the time dependences of the magnetization and the resistance relaxation: logarithmic, power-law-like, exponential (Debye), ‘stretched’ or ‘compressed’ exponential [7–9]. All these expressions depend on the mechanisms involved: the nucleation and ferromagnetic domain wall propagation, spin-glass-like behaviour, local disorder and others. It has to be pointed out that the magnetization reversal was also investigated in a number of out-of-plane and in-plane magnetized ultrathin epitaxial magnetic films and multilayers [10–12], however, there is a lack of information about investigations of magnetic relaxation anisotropy of thin nanostructured manganite films.

Finally, it has to be stressed that the stability of the electrical resistance and magnetoresistance values of the manganite films concerning device applications is of great importance. The investigations of ageing phenomena of manganite material were performed mostly on the polycrystalline ceramics. However, there is a lack of the investigations of ageing phenomena in thin manganite films. Therefore, the research of ageing effects which occur in the nanostructured manganite films is very important from the fundamental point of view to determine mechanisms responsible for the change of the main parameters of the films in time, as well as for device applications in order to stabilize their parameters.

Therefore, to gain an understanding of the magnetoresistance phenomenon and resistance relaxation in nanostructured manganite films, it is important to study electrical transport and magnetic reversal mechanisms in these films as well as ageing phenomena, especially focussing on the processes occurring in randomly oriented crystallites and disordered grain boundaries.

The object of the research. The object of the research described in this work are nanostructured manganite films: $\mathrm{La_{1-x}Sr_xMnO_3}$ and $\mathrm{La_{1-x}Ca_xMnO_3}$.

The aim of the work. The main aim of the present work is to investigate magnetoresistance and electrical resistance relaxation phenomena in nanostructured La-Sr(Ca)-Mn-O films, to clear up the origin of these effects and to determine the main properties of the films for the development of fast high magnetic field sensors operating at two ranges of temperatures: close to room and cryogenic.

The tasks of the work.

1. To investigate how chemical composition, deposition conditions and thickness of La-Sr(Ca)-Mn-O films influence the magnetoresistance values of these films in a wide range of temperatures (5–300 K) and magnetic fields (up to 60 T).
2. To study resistance relaxation phenomena upon removal of magnetic field pulse in La-Sr(Ca)-Mn-O films, and to determine how characteristic time constant and remnant resistivity depends on ambient temperature and magnetic field.
3. To analyse charge carrier transport and magnetic reversal mechanisms which determine magnetoresistance and resistance relaxation phenomena in nanostructured manganite films.
4. To investigate influence of accelerated thermal and long-term ageing on La-Sr-Mn-O film properties and clear up optimal conditions which could be used to stabilize resistance and magnetoresistance of these films.

5. To clear up the possibility to develop fast high pulsed magnetic field sensors operating at two ranges of temperatures: close to room and cryogenic.

Methodology of research. Methods used for the research were based on magnetic field generation and recording of the response of resistivity change of the investigated films. The results were analysed considering processes occurring in crystallites and grain boundaries of the nanostructured films mainly using modified Mott's hopping, Kolmogorov-Avrami-Fatuzzo and Kohlrausch-Willams-Watts models.

Scientific novelty. Novelty of this work includes the following findings:

- It was obtained that magnetoresistance of nanostructured manganite films can be analysed using modified Mott's hopping model taking into account contributions of both crystallites and grain boundaries, and its dependences on magnetic flux density scale with the sum of corresponding Brillouin functions $\mathcal{B}$ in ferromagnetic state and with the sum of $\mathcal{B}^2$ in paramagnetic state.
- It was found that in nanostructured manganite films the resistance relaxation process, after magnetic field is switched off, has two different components: 'fast' ($\sim$ 100 µs), and 'slow' ($\geqslant$ 1 ms). The characteristic time constants and relative parts of the remnant resistivity of these processes were systematically analysed for the first time in a wide range of temperatures and magnetic fields. It was demonstrated that the 'fast' magnetic relaxation process could be analysed using the Kolmogorov–Avrami–Fatuzzo model, and the nucleation and reorientation of magnetic domains into their equilibrium state is a predominant mechanism of this process, while the 'slow' magnetic relaxation process could be analysed using the Kohlrausch–Williams–Watts model considering the interaction of the magnetic moments in disordered grain boundaries having spin-glass properties.
- It was shown that the treatment of nanostructured manganite films by annealing them in an argon atmosphere at temperatures of 100–200 °C accelerates their ageing process and stabilizes their resistance and magnetoresistance. The annealing of the manganite samples coated by a hot-melt adhesive

increases the accelerated ageing process by almost three times. It was found that the ageing kinetics leads to a significant increase of the film resistivity which can be explained by the model of hierarchically limited relaxation dynamics with stretched exponential dependence typical for topologically-disordered systems, and is related with oxygen depletion and its diffusion in the grain boundaries of the nanostructured manganite films.

Practical value. The obtained results enable to suggest development of fast high pulsed magnetic field sensors operating at two ranges of temperatures: close to room and cryogenic. For the first application (appropriate high temperatures) the nanostructured La-Sr-Mn-O films are favoured. For the second application (cryogenic temperatures) the La-Ca-Mn-O films exhibiting higher magnetoresistance values and lower remnant resistivity are preferable. The results of the investigation of magnetic relaxation phenomena revealed the possible time scales of the sensors operation: for measurement of high pulsed magnetic fields with durations longer than milliseconds, the 'fast' resistance relaxation plays insignificant role, while the 'slow' relaxation process occurring in milliseconds time scale could be reduced by more than two times using La-Ca-Mn-O films with higher phase transition temperature. It was demonstrated that good stability of main parameters of magnetic field sensors (resistance and magnetoresistance change $<$ 2% during two years) could be achieved using accelerated ageing procedure by annealing the films in argon atmosphere at 100 °C temperature for more than 24 hours. The annealing of the film covered by a special hot-melt adhesive decreases the required annealing time.

Statements for defence.

1. Morphology and chemical composition of La-Sr(Ca)-Mn-O nanostructured manganite films strongly influences magnitude of their magnetoresistance which dependence on magnetic field is well described by modified Mott's hopping model taking into account contributions of both crystallites and grain boundaries.
2. The 'fast' resistance relaxation process in La-Sr(Ca)-Mn-O nanostructured manganite films after removal of magnetic field pulse, that takes place in

microseconds time scale, to a large extent depends on the structure and morphology of the films and is dominated by magnetic domain nucleation and reorientation to equilibrium state. Its kinetics is well described by the Kolmogorov-Avrami-Fatuzzo model using compressed exponential expression.

3. The ‘slow’ resistance relaxation process in La-Sr(Ca)-Mn-O nanostructured manganite films after removal of magnetic field pulse, that takes place in milliseconds time scale, is determined by processes occurring in disordered grain boundaries and is well described by the Kohlrausch-Williams-Watts model using stretched exponential expression.
4. Treatment of La-Sr(Ca)-Mn-O nanostructured manganite films by annealing in an argon atmosphere at higher than exploitation temperatures accelerates their ageing process and stabilizes their resistance and magnetoresistance. The observed resistivity increase can be explained by oxygen depletion and its diffusion in the grain boundaries of the films, and its kinetics is well described by the model of hierarchically limited relaxation dynamics with stretched exponential dependence typical for topologically-disordered systems.
5. Nanostructured $\mathrm{La_{1-x}Sr_xMnO_3}$ films having a higher sensitivity to magnetic field at room temperature should be favoured for the application at appropriate high temperatures, while for fast pulsed high magnetic field sensors operating at cryogenic temperatures the $\mathrm{La_{1-x}Ca_xMnO_3}$ films which exhibit higher magnetoresistance values and smaller relative remnant resistivity have to be used.

Approval of the work results. On the subject of the dissertation eight articles were published in scientific journals included in Thomson Reuters Web of Science database, two articles in conference proceedings.

The work was presented at seven following conferences:

- 4th Euro-Asian Pulsed Power Conf. / 19th Intern. Conf. on High-Power Particle Beams, Karlsruhe, Germany, Sept. 30–Oct. 4, 2012.

- 41-ji Lietuvos Nacionaline Fizikos Konferencija (41-th Lithuanian National Conference in Physics), Vilnius, Lithuania, June 17-19, 2015.
- 15th International Symposium on Ultrafast Phenomena in Semiconductors, Vilnius, August 25–28, 2013.
- IEEE International magnetic conference INTERMAG-2014, Dresden, Germany. May 4-8, 2014.
- 11th International Conference on Research in High Magnetic Fields RHMF-2015, Grenoble, France, 1-4 July, 2015.
- 5th Euro-Asian Pulsed Power Conf. Kumamoto, Japan. September 8-12, 2014
- 6th Euro-Asian Pulsed Power Conf. / 21th Intern. Conf. on High-Power Particle Beams / 15th International Conference on megagauss magnetic field generation and related topics, Estoril, Portugal, Sept. 18-22, 2016

Author's Contribution. The results and findings presented in this dissertation were obtained by the author in co-operation with his co-authors of the publications listed in the bibliography. The author's contributions include experimental research of magnetoresistance (up to 25 T) and resistance relaxation, including data recording and analysis by using modified Mott's hopping, Kolmogorov-Avrami-Fatuzzo and Kohlrausch-Willams-Watts models. The obtained results helped to interpret the observed phenomena in discussions with the co-authors. Also, the author participated in the improvement of magnetic field generation and recording setup used for magnetoresistance and magnetic relaxation measurements.

Structure of the Dissertation. The dissertation consists of an introduction, three main chapters, general conclusions, references, and list of publications. The main chapters include literature review, description of samples preparation and experimental setup, and obtained results. This work includes 113 pages, 56 numbered equations, 73 figures, 7 tables and 101 bibliographical references.

Chapter 2

Review of Physical Properties of Manganites

2.1 Crystallographic structure

Manganite oxides exhibiting perovskite structure are determined by chemical formula $RE_{1-x}D_xMnO_3$ (RE is a rare earth element and dopant D is usually an alkaline element). The base compound used in our research is $LaMnO_3$. The crystal lattice of most manganites is perovskite-like and nearly cubic (Fig. 2.1). When doping with lighter Sr or Ca ions the structure gets rhomboidal or orthorhombic lattice distortions resulting from either tilting or stretching (Jahn-Teller distor-

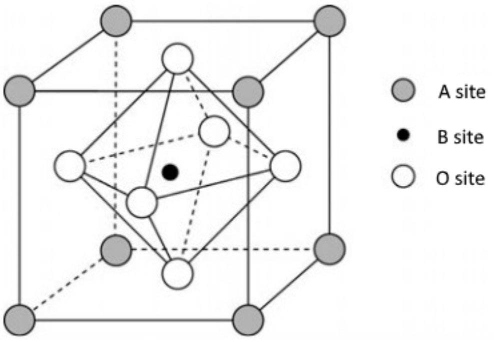

Figure 2.1: Ideal cubic perovskite structure. A site is occupied by La, Sr, Ca while small B cation is a host for Mn. Oxygen takes positions at O sites.

tion) of the oxygen octahedron around the Mn ions. This structure tends to accommodate misfit in the ionic sizes and electronically induced deformations by various kinds of distortion to larger cells with lower symmetry [13]. Stable structures are determined by tolerance factor t, when $0.89 < t < 1.02$ [14]:

$$t = \frac{rA + rO}{\sqrt{2}(rB + rO)}. \tag{2.1}$$

Large sized RE trivalent ions (e.g. La) and D divalent ions (Sr, Ca) occupy the A-site with 12-fold oxygen coordination. The smaller Mn ions in the mixed-valence state Mn^{3+} – Mn^{4+} are located at the centre of an oxygen octahedron – the B-site with 6-fold coordination.

2.2 Electronic structure

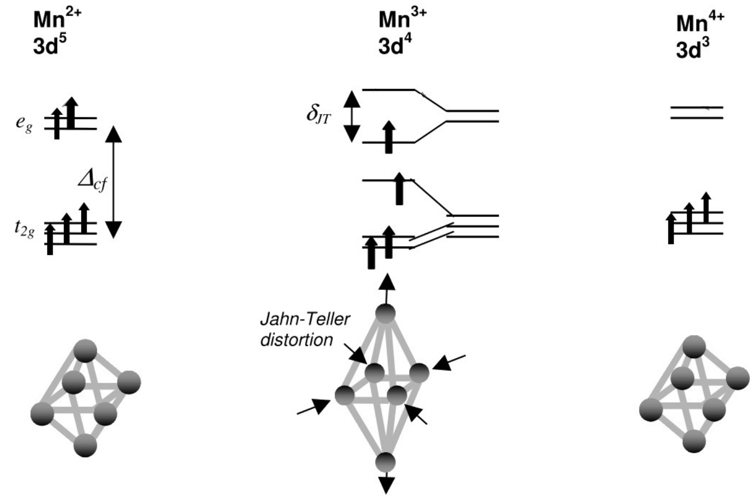

Figure 2.2: Single ion scheme of $3d$ electron states in Mn^{2+}, Mn^{3+} and Mn^{4+} ions in perovskite manganites. Here Δ_{cf} is cubic crystal field splitting energy(≈ 1.8 eV) and δ_{JT} is Jahn-Teller splitting energy (≈ 0.6 eV) resulting from distortion of the oxygen octahedron. Adapted from [15].

Magnetic and electrical properties of manganites depend on configuration of Mn ion $3d$ shell valence electrons. Five degenerated orbital states are available to the $3d$ electrons in an isolated Mn ion. In a basic crystal of MnO_6 the degeneracy is partly lifted and five d orbitals are split by a cubic crystal field into three t_{2g}

orbitals and two e_g orbitals. In the compound of $\mathrm{RE_{1-x}D_xMnO_3}$ the end members at $x = 0$ and $x = 1$ in ideal case contain only $\mathrm{Mn^{3+}}$ and $\mathrm{Mn^{4+}}$ respectively while in intermediate composition range $0 < x < 1$ there is simultaneous presence of both $\mathrm{Mn^{3+}}$ and $\mathrm{Mn^{4+}}$. Electronic configuration of $\mathrm{Mn^{3+}}$ ion in crystal field is $t_{2g}^3 e_g^1$ with lifted degeneracy due to axial elongation of the oxygen octahedron (Jahn-Teller distortion) as shown in Fig. 2.2. $\mathrm{Mn^{4+}}$ in contrast does not have a tendency to distort its octahedral environment and electrons fully occupy t_{2g}. Due to high Hund's energy electrons occupy all levels with the same spin state [16]. Generally, t_{2g} electrons are strongly localised while e_g electrons are weakly localised and determine electrical conductivity of the compound.

2.3 Phase diagram

Manganites are magnetic materials governing phases of ferromagnetic (FM), paramagnetic (PM), antiferromagnetic (AFM) or canted anti-ferromagnetic states [17]. Phase transition temperature (Curie temperature T_C for FM → PM transition and Néel's temperature T_N for AFM → PM) depends on doping level x. The phase diagrams are presented in Fig. 2.3 [18, 19].

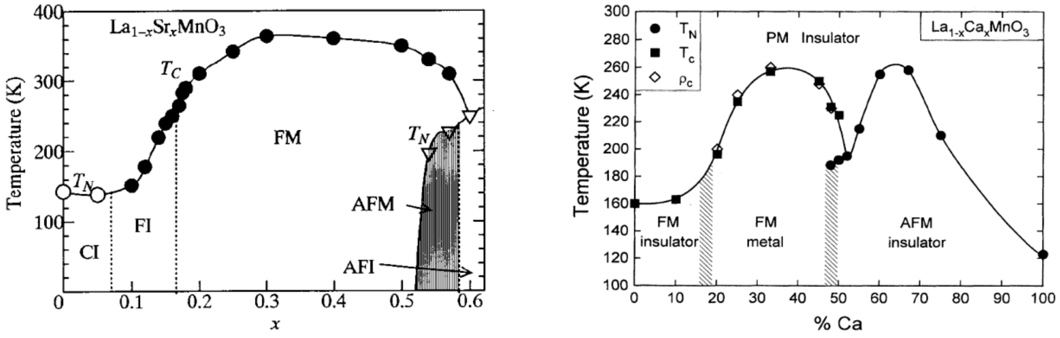

Figure 2.3: Phase diagrams of common manganite compounds. Left side – LSMO [19], right – LCMO [18],

At temperatures higher than T_C, $\mathrm{La_{1-x}Sr_xMnO_3}$ (LSMO) compound is paramagnetic insulator (PI) when $x < 0.175$ or paramagnetic metal (PM) when $x > 0.175$. $\mathrm{La_{1-x}Ca_xMnO_3}$ (LCMO) is PI in whole x range above T_C. More detailed phase diagrams can be found in references [18–21].

2.4 Electrical conductivity

Double exchange model. Electrical transport in manganites is described by double exchange (DE) model originally proposed by Zener [22, 23]. According to this theory electrons simultaneously transfer from e_g level of Mn^{3+} to O^{2-} and from O^{2-} to the empty e_g level of Mn^{4+}. In a case of strong DE, the e_g electrons become delocalized in a ferromagnetic phase for a certain range of doping concentrated around x almost equal to 1/3. Due to interatomic Hund's rule up and down spin bands are separated by 1 eV or more and the upper band is empty, leading to half-metallic behaviour [24] (See Fig. 2.4). The conduction band is thus fully spin-polarized and carriers do not change their orientation when hopping between neighbouring Mn^{3+} and Mn^{4+} ions. It was deducted that the probability of such transport depends on the angle θ between magnetic moments of neighbour Mn ions [25]:

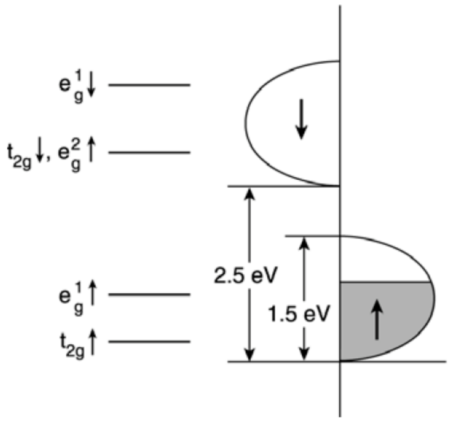

Figure 2.4: Schematic view of the band structure of $La_{2/3}Sr_{1/3}MnO_3$. After [24].

$$P \propto \cos(\theta/2), \tag{2.2}$$

Although DE provides qualitative understanding for resistivity change during FM → PM transition, electron-lattice coupling must be included for quantitative explanation. Gennes [26] demonstrated that for small values of x local distortions of the anti-ferromagnetic structure tend to trap the charge carrier. Localisation of charge carriers increases their interaction with the surrounding magnetic environment and, as a result, the effective mass is increased for the hopping electrons. But charge hopping is also related to the lattice distortions as described by the Jahn-Teller effect. This carrier transport influenced by lattice and spin distortions is usually referred to as magnetic polarons. Few studies have found evidence on localisation of charges and the formation of small (similar to the size of a unit cell) polarons in perovskite manganite materials above T_C [27–30].

Variable Range Hopping model. Mott's Variable Range Hopping (VRH) model is usually used to describe electrical conductivity in materials where main charge mobility mechanism is polaron-like. This model is derived for charge carriers that are localised in lattice (as polarons) and can move only by tunnelling or hopping (when it is favoured energetically) through potential barriers to other locations [31]. There is a competition between the potential energy difference and the distance electrons can hop as it is shown in the Mott's equation:

$$\sigma = e^2 R_h^2 \upsilon_{Ph} N(E_F) \exp(-\frac{2R}{L} - \frac{W_{ij}}{kT}), \tag{2.3}$$

where R is hopping distance, υ_{Ph} – phonon frequency, $N(E_F)$ – density of Fermi levels, L – charge carrier localisation distance, W_{ij} – potential barrier between start i and end j of the hop. The probability of charge transfer is higher when magnetic moment is the same at the start and end of hop. Neighbouring moments become orientated to same direction and potential barrier is lowered when external magnetic field is applied or temperature is lowered (i.e. material goes into ferromagnetic phase). This model fits with experimental data and is widely used to characterise the magnetoresistivity of manganite films [32].

According to Mott's VRH model, the expression for electrical resistivity in three dimensional hopping can be written as [32, 33]

$$\rho = \rho_{res} \exp(T_0/T)^{1/4}, \tag{2.4}$$

where ρ_{res} is residual resistivity and T_0 is the Mott's characteristic temperature, which can be expressed as follows:

$$T_0 = 18/[a^3 k_B N(E_F)], \tag{2.5}$$

where a is the localization length, k_B is the Boltzmann's constant and $N(E_F)$ is the density of states at the Fermi level. The mean hopping distance, $R_h(T)$, and hopping energy, $E_h(T)$, can be expressed at a given temperature T, as [32, 34]:

$$R_h(T) = (3/8)a(T_0/T)^{1/4}, \tag{2.6}$$

$$E_h(T) = (1/4)k_B T^{3/4} T_0^{1/4}. \tag{2.7}$$

The value of the parameter T_0 can be a measure of the strength of the lattice distortion and is inversely proportional to the spatial extent a of the localized wave function and density of states $N(E_F)$ (see Eq. 2.5).

Metal-Insulator Transition. Simple manganite compounds with strong DE, such as $La_{1-x}Sr_xMnO_3$ or $La_{1-x}Ca_xMnO_3$, where $x \approx 0.3$, exhibit a transition from a high temperature paramagnetic semiconducting or insulating phase to a low temperature highly conductive ferromagnetic phase.

In the PM phase, electrical resistivity has a strong temperature dependence and different $\rho(T)$ laws have been applied to fit experimental data. Several researchers reported semiconducting behaviour $\ln(\rho/\rho_\infty) = E_a/kT$ [35] with activation energy of about 0.2 eV, while others have found that the data can be better fitted by Variable Range Hopping (VRH) model $\ln(\rho/\rho_\infty) = (T_0/T)^{1/4}$ [32, 36], as was described in more detail in previous section. Both of these laws have physical origins, which are respectively: the existence of a pseudo-gap at the Fermi level in the PM phase; the localisation of the charge carriers by the magnetic disorder [24].

At low temperatures, the spontaneous alignment of the Mn spins below the T_C, allows a de-localization of the e_g electrons, leading to a low resistivity FM phase with $\rho \approx \rho_0 + aT^2$ for $T \ll T_C$. This alignment of the Mn spins can be induced for $T \geqslant T_C$, or reinforced for $T \leqslant T_C$, by applying an external magnetic field. The maximum effect is obtained close to T_C (Fig. 2.5) since the initial magnetic susceptibility diverges as $T \to T_C$ [24, 37].

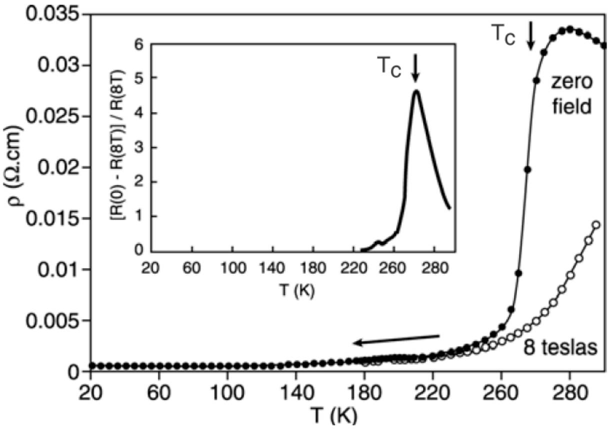

Figure 2.5: Resistivity in zero field and in a 8 T applied field versus temperature of a single crystal of $La_{0.825}Sr_{0.175}MnO_3$. In inset is magnetoresistance ratio versus temperature. The arrow indicates the Curie temperature. Adapted from [24].

2.5 Magnetoresistance of polycrystalline manganites

Magnetoresistance of polycrystalline manganites is analysed in two different ranges: low-field magnetoresistance (LFMR) and high-field magnetoresisitance (HFMR). LFMR is observed as sharp decrease of resistance in magnetic field and is usually investigated in magnetic fields less than 0.5 T. Above this limit one can observe the HFMR exhibiting smaller slope with magnetic field change, which in polycrystalline manganites is also known as extrinsic colossal magnetoresistance (CMR) because of its large extent coming from existence of disordered grain boundaries [38].

$$MR = \frac{R(B) - R(0)}{R(0)} \times 100\%. \tag{2.8}$$

MR is usually expressed in percent and defined by Eq.2.8, where $R(B)$ and $R(0)$ are electrical resistance values in magnetic field and without it respectively.

Low-field magnetoresistance. LFMR is observed at all temperatures below T_C in polycrystalline material while it is absent in single crystals (Fig. 2.6). This effect is distinctly different from HFMR. Hwang *et al.*[39] found that the negative MR of the polycrystalline samples is dominated by spin-polarized tunnelling between grains, and the key feature observed is a large negative MR at very low fields associated with magnetic domain rotation at the grain boundaries [40–42]. This grain-boundary scattering has been isolated in elegant model experiments on manganite strips on a bi-crystal substrates [43]. The predominant feature of LFMR is a sharp drop in the resistance at low fields, followed by a slower background negative CMR (HFMR). This sharp drop is the greatest at low temperatures and decreases with increasing temperature. This behaviour is associated with sharp increase in magnetization suggesting an anti-ferromagnetic inter-grain interaction. The ferromagnetic alignment of neighbouring grains by an applied field then allows increased electron tunnelling because of high degree of spin polarization (See Fig. 2.4 in previous section 2.4). Lee *et al.* [44] has shown that low field magnetoconductivity, rather than the magnetoresistance, in the low temperature limit is universally close to 1/3, which is consistent with second-order tunnelling through inter-facial spin sites at the grain boundary. In the presence of a field, the thermal average of the boundary spin is proportional to spin sus-

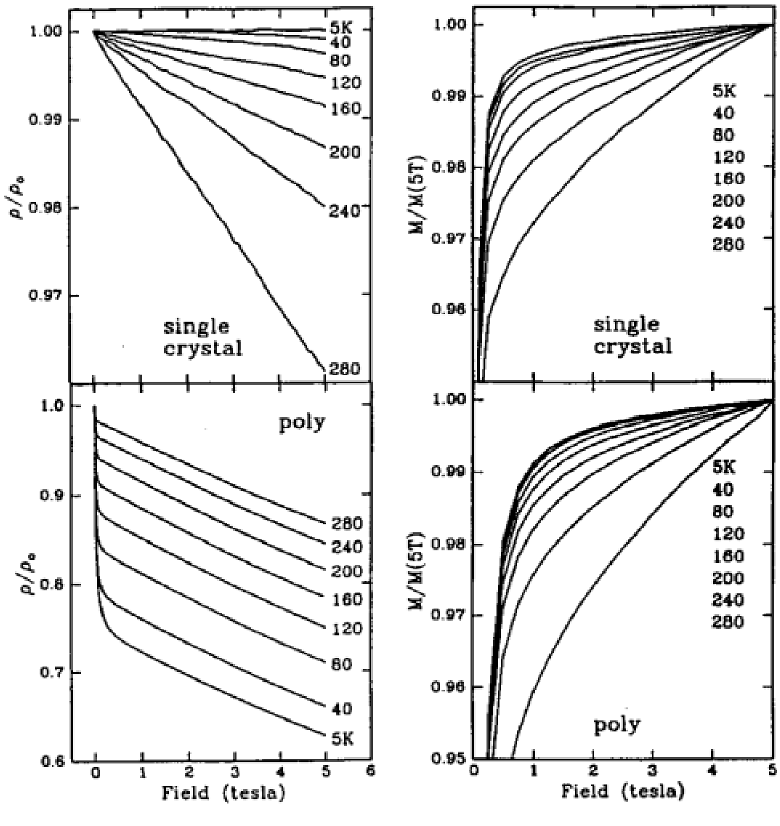

Figure 2.6: Comparison of the negative magnetoresistance of single-crystal and polycrystalline LSMO. Adapted from [39]

ceptibility of boundary states. Therefore, the conductivity can be expressed by [44]

$$\frac{\sigma}{\sigma_0} = 1 + \frac{1}{3}M^2 + 2\chi_b HM, \tag{2.9}$$

where χ_b is the spin susceptibility of the boundary states, H – applied field, M – normalized magnetization of grain.

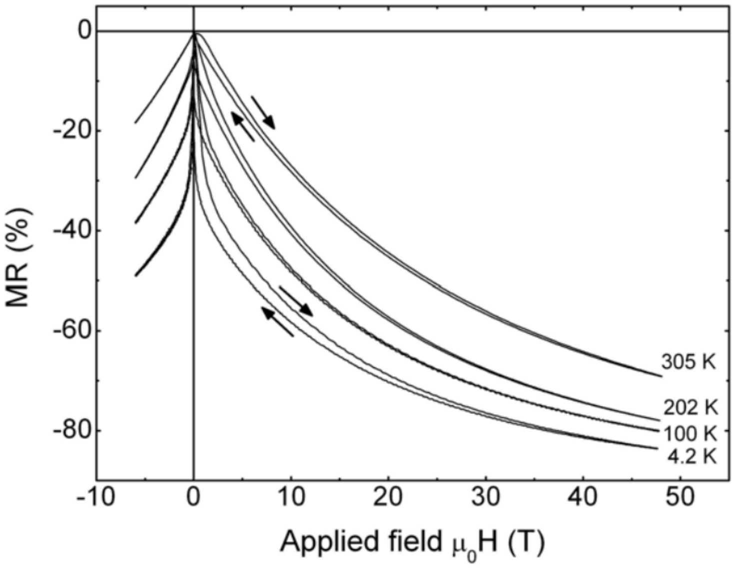

Figure 2.7: Field dependence of the magnetoresistance for LSMO manganite. Adapted from [45]

High field magnetoresistance (CMR). Colossal magnetoresistance (CMR) is observed in a large number of polycrystalline manganites where MR values of 80% and more are reached at very high fields up to 50 T and above with no clear evidence of saturation [45, 46]. It is attributed to alignment of magnetic moments in grain boundaries and is most pronounced in the vicinity of T_C. CMR is caused by a magnetic field-induced enhancement of carrier mobility while the carrier density is not affected [45, 47]. Considering high field region, some offer presenting results as relation of resistivity (see left side of Fig. 2.6) or magnetoconductivity as seen in Eq.2.9. In the latter case, experimental results can be fitted by simple linear expression [44, 48]. Wagner *et al.* [31] explained MR in more detail by extending Mott‘s hopping model to explain the magnetic field dependence of magnetoresistance. According to this model MR can be approximated by a Brillouin function $\mathcal{B}$ in FM and $\mathcal{B}^2$ in PM phases:

$$MR = A(T) \times \mathcal{B}(g\mu_B J(T)B/k_BT) \qquad T < T_C, \tag{2.10}$$

$$MR = A(T) \times \mathcal{B}^2(g\mu_B J(T)B/k_BT) \qquad T > T_C, \tag{2.11}$$

where $A(T)$ is a temperature-dependent CMR amplitude, $g = 2$ is the gyromagnetic ratio, μ_B -the Bohr magnetron, B – applied magnetic field, $J(T)$ – the average spin moment at the hopping sites and $\mathcal{B}$ is defined as

$$\mathcal{B} = \frac{1}{j}\left\{\Big(j + \frac{1}{2})\coth\left[\left(j + \frac{1}{2}\right)\chi\right] - \frac{1}{2}\coth\left[\frac{1}{2}\chi\right]\right\}, \tag{2.12}$$

where $\chi = g \times \mu_B \times J \times B/k_BT$ Brillouin function is used for defining magnetic moments of atoms or ions. It can have values from 0 (no external field applied) to 1. While investigating temperature dependence of this function some researchers [31, 49] found large values of the spin moment J. The very high moments (for example, $J \approx 60$ at 200 K was observed by [31], whereas $J = 2$ for a bare Mn^{3+} ion) indicate that the perovskite behaves as a paramagnet with formation of ferromagnetic clusters absorbing particles in a short range of typically three or more lattice constants and lowering their energy levels. These clusters might be interpreted in terms of 'large spin polarons' introduced by [50] (see Fig. 2.8). Moreover, this cluster size agrees well with carrier localization length calculated by applying the VRH model (10.2 Å) and with the magnetic-polaron diameter (12 Å) determined by De Teresa *et al.* [27]. Thus fitting experimental data by Brillouin functions provides J parameters values that can give information about hopping mechanisms in the films.

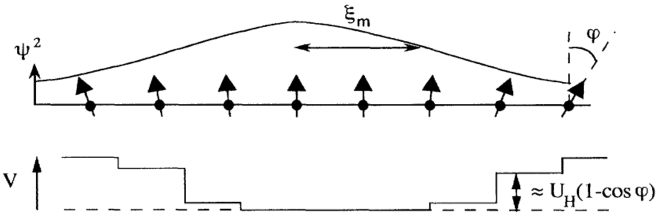

Figure 2.8: Spin-dependent potential well producing a magnetic polaron. Here ξ_m is the size of large bound polaron and U_H is Hund's coupling energy. Adapted from [50].

2.6 Magnetic relaxation and reversal

Magnetic relaxation upon removal or reversal of the external magnetic field is studied in bulk and film magnetic materials, where magnetization processes are of great importance in information storage technology. Magnetic relaxation has been investigated for several decades. Through numerous experimental studies that have been carried out, several issues remain in the interpretation of the results. First, there are several expressions to characterize the time dependence of the magnetization relaxation such as the Richter-type logarithmic relaxation and the stretched exponential relaxation. Second, the time dependence is occasionally analysed by an exponential Debye relaxation. In this case, the energetic view of the magnetic system is oversimplified. Third, the characterization of the time dependence of magnetization relaxation and reversal in magnetic thin films has been mostly qualitative based on the Fatuzzo model [51]. Therefore, magnetic relaxation is a rather complicated phenomenon. Many models have been proposed that can be used to characterize the time-dependences of the magnetization and the resistance relaxation: logarithmic [8, 52], power-law-like [53], exponential Debye [9], stretched or compressed exponential [7, 54, 55]. It also should be noted,

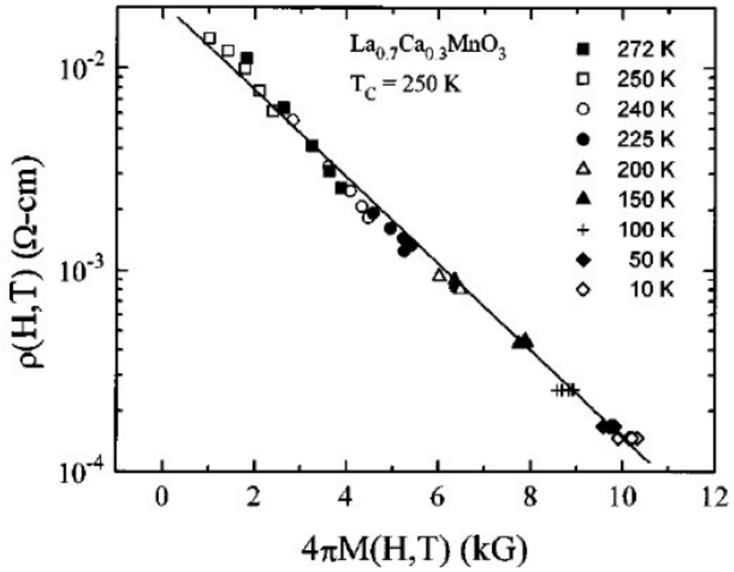

Figure 2.9: The resistivity scales logarithmically with the magnetization of the film for all recorded temperatures, giving evidence for strong correlation of resistance and magnetic order. Adapted from [56].

that according the generally accepted Zener double exchange model [22], which is commonly used for a description of manganese compounds, it is assumed that the magnetic field aligns the local Mn-t_{2g} spins ferromagnetically and facilitates hopping of the conduction electrons Mn-e_g between adjacent Mn-ions sites. Due to this close relation between transport properties and the magnetization in manganese compounds [10, 56, 57] (see Fig. 2.9), the resistance relaxation measurements provide an excellent indirect method for characterization of the magnetic relaxation observed in manganites.

2.6.1 Logarithmic relaxation

Probably the best-known is the logarithmic relaxation in the magnetics research literature. Let's consider a single magnetic domain or particle. An external magnetic field opposite to the initial magnetization direction would cause the particle to overcome the energy barrier and reverse its field direction for the minimum energy state. The time dependence of the magnetization is written as [7]

$$M(t) = M_0(2\mathcal{B}(t) - 1) \tag{2.13}$$

and $\mathcal{B}(t) = \exp(-t/\tau)$ describes the simple Debye relaxation that involves just a single energy barrier. At finite temperatures, the time constant τ for the magnetization reversal follows the Arrhenius–Neel law:

$$\tau = \nu_0^{-1} \exp(\Delta E/k_B T), \tag{2.14}$$

where the attempt frequency ν_0 in the range of $10^9 - 10^{11}$ Hz is related to the spin-lattice interaction. ΔE is the energy barrier that is a function of the applied field and $k_B T$ is the thermal activation energy. In an assembly of non-interacting magnetic particles, the time-dependent magnetization is determined by the statistical reversals of individual particles towards thermal equilibrium. Therefore, the magnetic relaxation by the system from measurement is [7]

$$\mathcal{B}(t) = \int_0^\infty \exp[-t/\tau(y)] g(y) dy. \tag{2.15}$$

Here y denotes the energy barrier that determines the time constant of reversal, $\tau(y)$. $g(y)$ is the distribution function of energy barriers in the magnetic particle system. Then given the distribution function is constant in a time period ($\tau_1 \leq \tau \leq \tau_2$) and zero outside the magnetization relaxation is obtained to be [7]:

$$M(t) \cong M_0 - S(H,T)\ln(t/t_0), \tag{2.16}$$

where $S(H,T)$ is known as the magnetic viscosity coefficient and is used to characterize the magnetic relaxation in the system. In cases where relaxation is not quite fit to logarithmic Eq.2.16, Sirena *et al.*[10] suggested that the relaxation process consists of a logarithmic and an exponential terms acting in series, which indicates the presence of both single energy barrier and distributed energy barrier for magnetization switching [10]:

$$M(t) = M_0 + c_1 e^{-t/\tau} - c_2 \ln(t), \tag{2.17}$$

where c_1 and c_2 are constants and M_0 is the initial magnetization value. Dominiczak *et al.* also proposed a model based on magnetic phase separated random resistance network where following expression of the time dependence of the resistance was derived [8]:

$$\frac{R}{R_0} = (1-\alpha)[\exp(-t/\tau) + S\log t] + \alpha. \tag{2.18}$$

Here S is a parameter defining resistive viscosity, τ is a characteristic relaxation time and α is the fraction of paramagnetic insulator considering FM → PM transition is taking place. The remainder of FM metallic sites is expressed as $(1-\alpha)$.

2.6.2 Power-law relaxation

Another kind of magnetization relaxation is the power-law time dependence [53]

$$M(t) = M_0 t^{-\zeta}, \qquad \zeta \geq 0. \tag{2.19}$$

This type has been observed in Monte Carlo simulations that were carried out to study the magnetic relaxation in single-domain ferromagnetic nano-particles and showed that for all the particle densities the magnetization approaches a finite remnant value slowly by a power law [53].

2.6.3 Kohlrausch–Williams–Watts relaxation

Stretched exponential relaxation (Eq.2.20) (also known as Kohlrausch–Williams–Watts or KWW) fits many relaxation processes in disordered electronic and molecular systems. For electronic relaxation the appearance of stretched exponential is often described in systems with randomly distributed traps (e.g. non-radiative exciton recombination) where after an initial probe pulse, the relaxation kinetics are represented by diffusion of excitations to fixed traps or sinks which are topologically equivalent to static points and are randomly (i.e., uniformly) distributed [58]. It was also observed in manganite films [59].

$$\mathcal{B}(t) = \exp\left(-(t/\tau)^{\beta}\right), \qquad 0 \leq \beta \leq 1, \tag{2.20}$$

In high temperature limit, both the traps and the defects diffuse and $\beta \to 1$, but in the low temperature limit, where the traps are immobile, β is given by this relation

$$\beta = d^{*}/(2 + d^{*}), \tag{2.21}$$

where d^{*} is the effective restricted dimensionality ($d^{*} \leq d \leq 3$) of the configuration space in which the relaxation takes place [60]. In complex, multi-nary perovskite-like structures of the manganites, it is difficult to identify the presence of most defects, and much more difficult to quantify the extent to which the electrically active defects are uniformly distributed. However, it has been shown that in materials where above conditions apply, d^{*} and β can be specified with high accuracy [60]. Firstly, the stretched exponential form can be distinguished from other relaxation functions if the observation time spans over multiple (3 to 6) decades. Secondly, only in fully disordered samples the stretched exponential relaxation is observed over such wide range and there is universal pattern of correlation of measured values of β with sample quality and structure on molecular scale. For density relaxation by thermal phonons and local phonons in intrinsic materials, $d^{*} = d = 3$ and $\beta = 3/5$, while for charge relaxation by thermal phonons and plasmons, again in intrinsic materials, $d^* = d/2 = 3/2$ and $\beta = 3/7$. To sum up, the β parameter obtained from stretched exponent fit can be used to characterize the nature and scale of sample inhomogeneities.

2.6.4 Kolmogorov–Avrami–Fatuzzo relaxation

The spontaneous or magnetic field-induced reversal of the magnetisation direction in materials and nano-structures has been the subject of studies since many decades. In nearly all materials the rotational symmetry is lost as a consequence of the discrete crystalline structure and the spin-orbit coupling, or due to bipolar interactions [61]. This effect is called magnetic anisotropy, which can be expressed as an angular-dependent energy. In the presence of anisotropy, a field of finite size is needed to reverse the magnetisation. For thin films and bulk magnetic materials with defects such as voids and pinning sites, the coherent reversal is not likely since the process is not favoured energetically. The picture is that first some reversed spins or grains appear in the films [7]. Via the short-ranged exchange coupling, the adjacent spins or grains are more likely to reverse than the others. Therefore, magnetic domains are formed and propagate over time from the reversed spins or grains, which are considered as nuclei. The magnetization reversal is achieved when the domains expand to cover the whole film. This so-called Kolmogorov–Avrami (KA) model was originally used to describe crystal growth [12, 62]. Under the framework of the KA model, the time dependence of magnetization reversal is expressed as [7]

$$\mathcal{B}(t) = \exp\,(-\int_0^t n(\tau)s(t-\tau)d\tau). \tag{2.22}$$

$n(\tau)$ is the nucleation rate at time τ. $s(t-\tau)$ is the domain expanding from a nucleus, which appears at time τ, for a given time t. The change of magnetization at time t is then the sum of the growth of the reversed domains from the nucleation that occurs from the beginning. The domain growth can be considered to be a power-law function [7]

$$s(t-\tau) = c(t-\tau)^\gamma, \tag{2.23}$$

where c is the domain growth speed and $\gamma \geq 0$. There are two limiting cases. Supposing nucleation occurs at $\tau = 0$ immediately after the reverse field is applied, i.e. $n(\tau) = \delta(\tau)$:

$$\mathcal{B}(t) = \exp\left(-ct^{\gamma}\right). \tag{2.24}$$

When nuclei appear at a constant rate, i.e. $n(\tau) = n_0$, the magnetization reversal is [7]

$$\mathcal{B}(t) = \exp(-\frac{cn_0}{\gamma+1}t^{\gamma+1}). \tag{2.25}$$

Both equations look similar to that of the KWW relaxation but, in the second case, the exponent, $\gamma + 1$, is known for sure to be greater than one. Fatuzzo [51] has elaborated the thin film relaxation associated with nucleation and domain growth based on the KA model with the assumptions that the nucleation rate decreases exponentially in time [51]:

$$n(t) = \exp(-Rt), \tag{2.26}$$

and circular domains grow with a speed v:

$$s(t-\tau) = \pi v^2 (t-\tau)^2. \tag{2.27}$$

Thus, the relaxation is obtained as [7, 51]

$$\mathcal{B}(t') = \exp[-k^2(2 - 2(t' + k^{-1}) + (t' + k^{-1})^2 - 2e^{-t'}(1 - k^{-1})) + (1 - t')], \tag{2.28}$$

where $t' = Rt$ and the parameter k is

$$k = v/Rr_c. \tag{2.29}$$

Here r_c is the radius of the nuclei. The magnetization reversal as a function of t' is solely determined by the parameter k. Furthermore, the time dependence described by equation 2.28 can be approximated by [7, 51]

$$\mathcal{B}(t') = \exp[-(t'/\tau(k))^{\beta(k)}], \tag{2.30}$$

or

$$\mathcal{B}(t') = \exp[-(Rt/\tau(k))^{\beta(k)}], \tag{2.31}$$

in a significantly long time range. $\tau(k)$ and $\beta(k)$ are only dependent on k. Figure 2.10 shows good consistency between equations 2.28 and 2.31 for multiple k values.

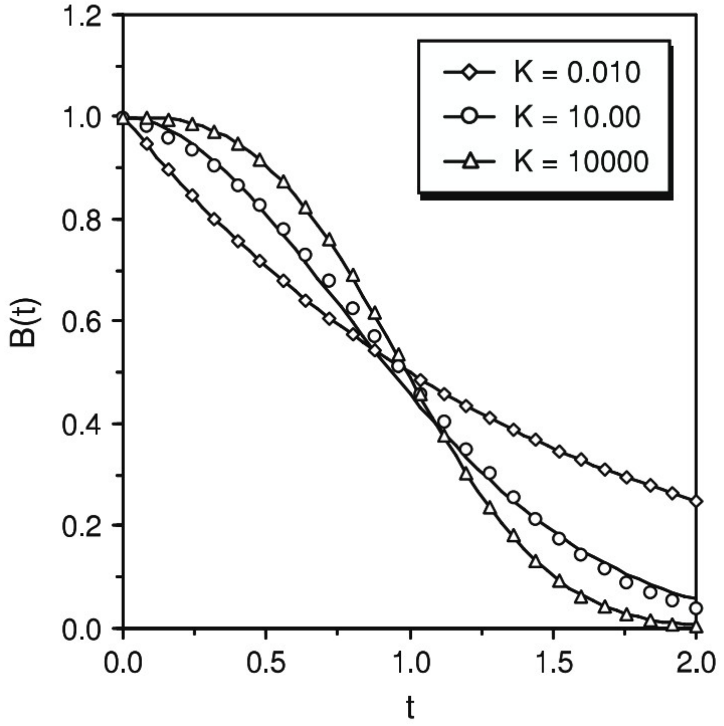

Figure 2.10: Equation 2.28 represented by the open dots fitted by compressed exponential functions for some typical cases, $k = 0.01$, 10 and 10000. Time t is normalized to the characteristic time constant $t_{1/2}$, where $\mathcal{B}(t)$ reduces to 1/2. Adapted from [7].

The relaxation is characterized by a time constant, $t_{1/2}$, at which the magnetization becomes zero and $\mathcal{B}(t) = 1/2$. Because of the property of equation 2.28, $t_{1/2}$ can be written as $t_{1/2} = h(k)/R$. Specifically, from equation 2.31,

$$t_{1/2} = (\ln 2)^{1/\beta(k)}\tau(k)/R \tag{2.32}$$

For the limiting case that the nuclei do not grow, $k \to 0$:

$$\mathcal{B}(t) = \exp(-Rt), \tag{2.33}$$

and

$$t_{1/2} = \ln 2/R. \tag{2.34}$$

For the other limiting case when domains grow extremely fast, $k \to \infty$ [7]:

$$\mathcal{B}(t) = \exp(-k^2R^3t^3/3), \tag{2.35}$$

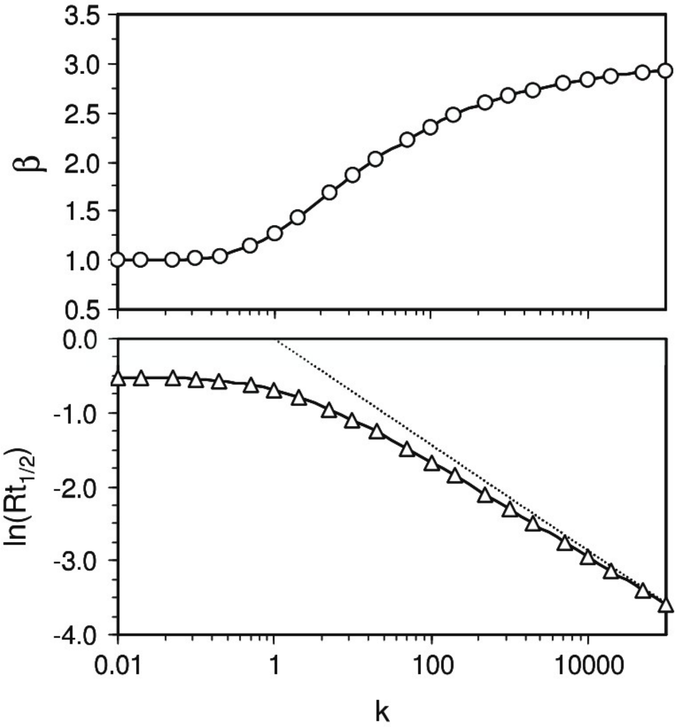

Figure 2.11: Exponent β and time constant $t_{1/2}$ as functions of k. The dotted line represents equation 2.36. Adapted from [7].

and

$$t_{1/2} = (3\ln 2)^{1/3}/Rk^{2/3} \tag{2.36}$$

Thus, $\beta(k) = 3$ and this is equation 2.25 with $\gamma = 2$ for the growth of circular domains, since the domains grow so fast that the change of nucleation rate over time is negligible. Figure 2.11 shows the exponent β and the time constant $t_{1/2}$ as functions of k. β increases gradually from 1 to 3 when k goes from 0 to $+\infty$. $t_{1/2}$ is close to $\ln 2/R$ for low k and follows equation 2.36 for high k. The characteristics of nucleation and domain growth can be readily obtained by fitting experimental data to equation 2.31 and then converting the fitting values for β and $t_{1/2}$ to R and k from this figure.

2.7 Ageing behaviour of manganites

Resistivity and magnetoresistance of manganites are very sensitive to the ambient temperature variations [1, 11, 63]. For this reason the temperature drift during operation of magnetic field sensors based on manganite materials is very important and has to be taken into consideration during design of such devices. This problem is solved by measurement of film's resistance in zero magnetic field just before the application of pulsed magnetic field which has to be measured [2]. In such case zero-field resistance of the film is a measure of ambient temperature while the resistance change in applied magnetic field is a measure of magnitude of this field. Thus manganite film is used not only as a magnetic field sensor, but also as a temperature sensor. In this case the stability of the electrical resistance and magnetoresistance over the time plays an important role in the development of these devices. However, it was observed that the structurally imperfect manganite films, such as polycrystalline [64] or very thin epitaxial [65], may undergo dramatic changes of their resistance with time which could limit their technological applicability. Moreover, for the application of the magnetic field sensors, where smaller magnetic fields (< 0.5 T) are measured, the role of magnetoresistance anisotropy (MRA) significantly increases [11]. Some research was focused on the investigation of the ageing phenomenon in polycrystalline manganese oxides which were used as negative temperature coefficient (NTC) thermistors or common cathode materials for solid oxide fuel cells [66, 67]. The ageing kinetics in these materials was analysed by using such relaxation functions as hyperbolic, 'stretched hyperbolic' or stretched exponential [68–70]. According to this research it is known that monotonically decaying kinetics of degradation, expressed by decreasing of controlled relaxation parameter $\eta(t)$ with time t, is described by this equation [69]:

$$\frac{d\eta}{dt} = -\lambda\eta^{\alpha}t^{\beta}, \tag{2.37}$$

where λ is a coefficient of proportionality and α, β are material-specific constants. Similarly, when the monotonically rising degradation kinetics takes place, the relaxation parameter $\eta(t)$ satisfies this differential equation [69]:

$$\frac{d\eta}{dt} = \lambda(1-\eta)^{\alpha}t^{\beta}, \tag{2.38}$$

The ageing kinetics is then determined by a relaxation function which can be

Table 2.1: Relaxation functions describing ageing kinetics types. Adapted from [69].

Mono-molecular RF1 ($\alpha = 1, \beta = 0$)	$N_\eta(t) = 1 - \exp(-\frac{t}{\tau})$, $\tau = \frac{1}{\lambda}, \lambda \neq 0$
Bimolecular RF2 ($\alpha = 2, \beta = 0$)	$N_\eta(t) = 1 - \frac{1}{1+\frac{\tau}{t}}$, $\tau = \frac{1}{\lambda}, \lambda \neq 0$
RF3 ($\alpha \neq 2, \beta = 0$)	$N_\eta(t) = 1 - \frac{1}{(1+\frac{t}{\tau})^k}$, $\tau = \frac{1}{\lambda(\alpha-1)}, k = \frac{1}{\alpha-1}, \alpha \neq 1, \lambda \neq 0$
Williams-Watts RF4 ($\alpha = 1, \beta \neq 0$)	$N_\eta(t) = 1 - \exp(-(\frac{t}{\tau})^k)$, $\tau = \frac{1+\beta}{\lambda}, k = 1+\beta, \beta \neq -1, \lambda \neq 0$
RF5 ($\alpha \neq 0, \beta \neq 0$)	$N_\eta(t) = 1 - (\frac{1}{(1+\frac{\tau}{t}^k)^r}$, $\tau = (\frac{1+\beta}{\lambda(\alpha-1)})^{\frac{1}{1+\beta}}, r = \frac{1}{\alpha-1}$, $k = 1 + \beta, \alpha \neq 1, \lambda \neq 0$

presented for Eq.2.38 in this form [69]:

$$N_\eta(t) = \frac{\eta_t - \eta_0}{\eta_\infty - \eta_0}, \tag{2.39}$$

where η_0 and η_∞ correspond to initial $t = 0$ and final $t \to \infty$ values of η_t measured before and after ageing test. There are five kinds of $N_\eta(t)$ relaxation functions (RFs) which can be considered as possible solutions for Eq.2.38 in dependence on α and β parameters (Table 2.1)[69].

When $\alpha = 1$ and $\beta = 0$ we have a well-known monomolecular relaxation process which is expressed by simple exponential dependence on time t (RF1 in Table 2.1). If the process is caused by recombination of specific defect pairs as electron-hole or vacancy-interstitial, the underlying kinetics is determined by bimolecular RF ($\alpha = 2$ and $\beta = 0$, RF2 in Table 2.1). The exact solution of Eq. 2.38 when $\beta = 0$ gives RF3 – a 'stretched' behaviour owing to standard αth order kinetics of ageing (degradation). RF3 is often used for describing post-irradiation thermal effects in some oxide glasses [70]. In case of $\alpha = 1$ and $\beta \neq 0$ the relaxation process is described by stretched exponential RF4 which is most suited for quantitative description of structural, mechanical and electrical degradation processes in glasses and other solids with dispersive nature of relaxation. This was introduced by Williams and Watts [71]. The exact general solution of Eq.2.38 with arbitrary values of α and β differed from 0 or 1 can be presented in RF5.

As seen by previous works for similar compound materials [64], significant increase of the resistivity is observed during the first hours of annealing, followed by saturation effect. The resistivity change in time during accelerated ageing (annealing at higher than operating temperatures) should be described by same functions as for ageing processes in random topologically-disordered media caused by increased temperature treatment. Given general differential equation 2.38 the normalized relaxation function in the case of polycrystalline manganite can be described as follows:

$$N_\rho(t) = \frac{\rho_t - \rho_0}{\rho_\infty - \rho_0}, \tag{2.40}$$

where ρ_t – resistivity at time instant t of the treatment at increased temperature; ρ_0 – initial resistivity value before the treatment; ρ_∞ – final resistivity at the end of the treatment (when time $t \to \infty$). As discussed the stretched exponent relaxation function (RF4 in Table 2.1) is the most suitable in this case for quantitative simulation. For growing kinetics the stretched exponent of the relative resistivity change can be expressed as follows:

$$\frac{\rho_t - \rho_0}{\rho_0} = \frac{\rho_\infty - \rho_0}{\rho_0}(1 - \exp{[-(\frac{t}{\tau})^k]}) \tag{2.41}$$

where τ – characteristic time; k – stretched exponent ratio.

Here the stretched exponent ratio can give a hint on what relaxation mechanisms take place. It should be noted that mechanisms of degradation processes in topologically-disordered systems can be quite different, however, two main groups can be identified among them. The first group explores mechanisms in disordered structures under dispersive transport conditions [68, 70]. Defects in these structures responsible for deviation from the thermodynamic equilibrium take place in multiple capture-elimination acts of excited carriers before being finally stabilized. The quantitative parameters of elementary capture and elimination acts form the continuous spectra in agreement with structural peculiarities of the disordered solid. The model of hierarchically limited relaxation dynamics [60, 69] is in a basis of the second group of mechanisms. Within this model, each individual relaxation act in disordered solid is possible after previous relaxation events formed favourable conditions for its realization (for example, free-volume space formation). The values of stretched exponent ratio for the first group of mechanisms are between 0.43 and 0.6 [60, 68, 72]. In the case of the second group of mechanisms the stretched exponent ratio shows the tendency to increase up to values in the range of 0.8–0.9 [68, 69]. The measurement of ageing kinetics and its analysis by using stretched exponent relaxation function can be used as method for the investigation of the ageing mechanisms in nanostructured manganite films used for magnetic field sensors fabrication. Experimentally obtained k values and their change with annealing temperature could show if or which of these mechanisms of relaxation processes are taking place.

Chapter 3

Samples Preparation and Experimental Setup

3.1 Samples preparation and characterisation

3.1.1 Film deposition – PI MOCVD

$La_{1-x}Sr_xMnO_3$ (LSMO) films where deposited using pulse injection (PI) metal organic chemical vapour deposition (MOCVD) technique which is a versatile technique for the deposition of oxide layers [73]. Single source solution has been prepared of $La(thd)_3$, $Sr(thd)_2$, $Mn(thd)_3$ (thd stands for 2,2,6,6-tetramethyl-3,5-heptandionate) precursors and monoglyme solvent. Ar + O_2 gas mixture was used to transport the vapour mixture towards the heated polycrystalline alumina (Lucalox, 99.9% Al_2O_3 + 0.1% MgO) substrate. For LSMO film the substrate's temperature has been varied from 600 to 750 °C to achieve different sample properties. After deposition the substrate with film was cooled down to room temperature in oxygen environment (760 Torr). During growth the thickness of layer was *in-situ* monitored using optical reflection interference method, consisting of a laser system ($\lambda = 670$ nm) and Si photo detector installed in the PI MOCVD reactor. Film thickness was varied from 75 to 420 nm. The chemical composition of the films was measured by means of Energy Dispersive X-ray spectroscopy (EDS) and was determined to be $La_{0.83}Sr_{0.17}MnO_3$.

The same technology was used for producing $La_{1-x}Ca_xMnO_3$ (LCMO) films, but the substrate, deposition temperature and other parameters where varied based on goals of the research. Firstly, some films were grown on different types of substrates: polycrystalline Lucalox, monocrystalline $LaAlO_3$ (100) and R-plane sapphire. The substrate temperature during deposition was 775 °C for all samples. Secondly, for some of samples the source solution of $La(thd)_3$, $Ca(thd)_2$, $Mn(thd)_3$ was modified to achieve different ($x = 0.2 - 0.4$) Ca content in the final composite. The average LCMO film thickness ranged from 300 to 320 nm.

3.1.2 Surface morphology and microstructure characterization

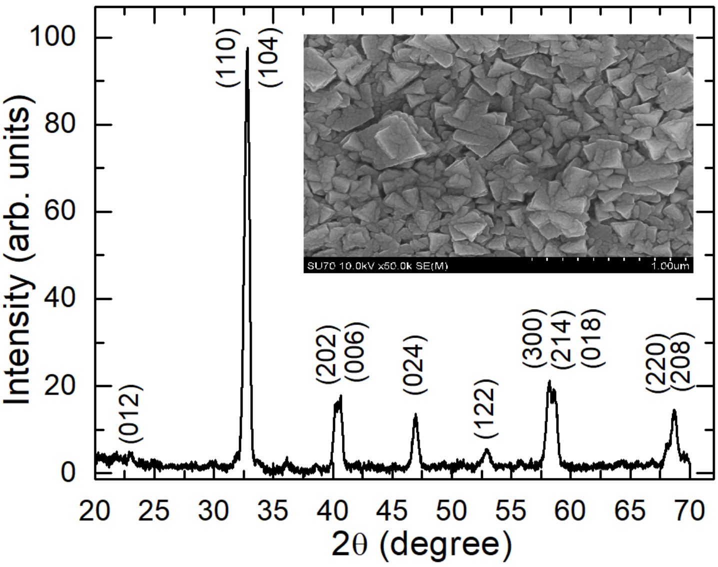

Figure 3.1: X-ray diffraction patterns in grazing incidence geometry for $La_{0.83}Sr_{0.17}MnO_3$ film grown on Lucalox substrate. All peaks are assigned to the reflections from a rhombohedral perovskite lattice (indices are given for hexagonal unit cell). Inset – SEM image of the film surface.

Grazing incidence X-ray diffraction (GIXRD) measurements of the samples were performed using SmartLab diffractometer. The angle of the incident X-ray beam was fixed at 0.5°. GIXRD spectra presented in Fig. 3.1 show that the films are single phase polycrystalline and their crystal structure is perovskite-like with rhombohedral distortions (the space group R3c). The study of film surface mor-

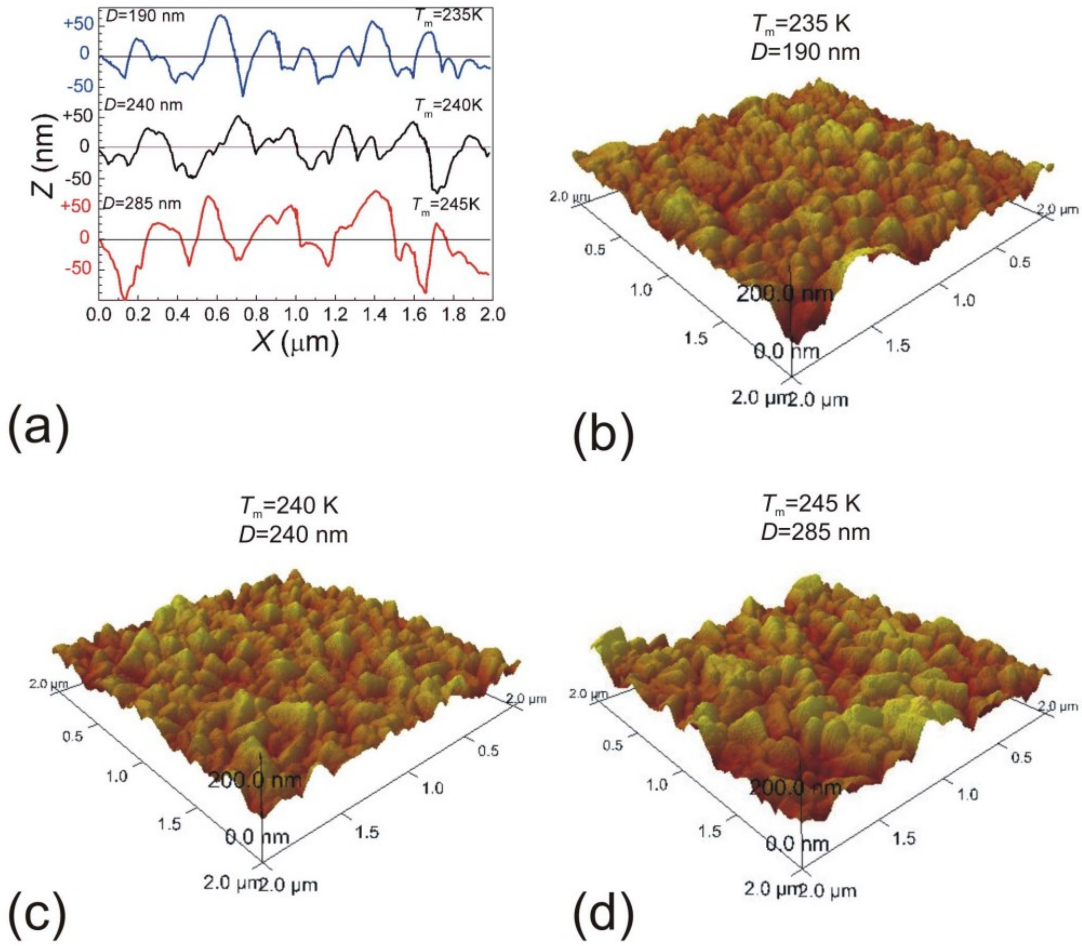

Figure 3.2: (a) AFM profiles. (b)–(d) Images of the films grown at different conditions and having different average crystallite dimensions D. The obtained D and T_m values are indicated in each image.

phology performed by SEM (see inset of Fig. 3.1) revealed that films consist of grains having average dimensions of about 50-140 nm depending on deposition condition.

The surface morphology and microstructure of the films were investigated using Atomic Force Microscopy (AFM, see Fig. 3.2), Scanning Electron Microscopy (SEM, Fig. 3.3a, 3.3b) and Transmission Electron Microscopy (TEM, 3.3c, 3.3d). Nanostructured nature of the films was observed: column-shaped crystallites with dimensions d of 30-70 nm were separated by 5–7 nm thickness grain boundaries (obtained from SEM). The AFM measurements revealed larger average dimensions D_{avg} of crystallites: 90–285 nm (see Tables 3.1, 3.2).

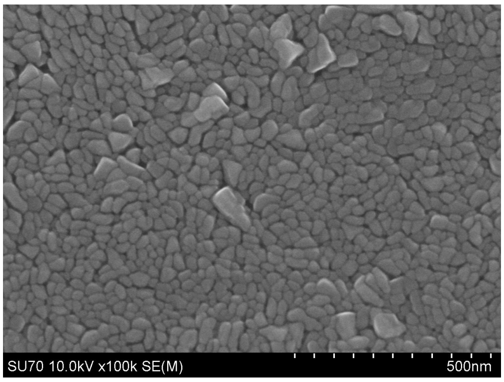

(a) SEM image of $d = 170$ nm sample

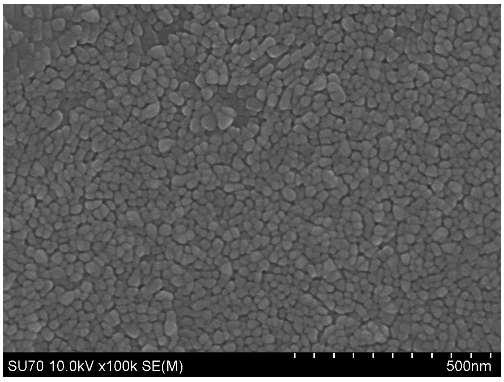

(b) SEM image of $d = 75$ nm sample

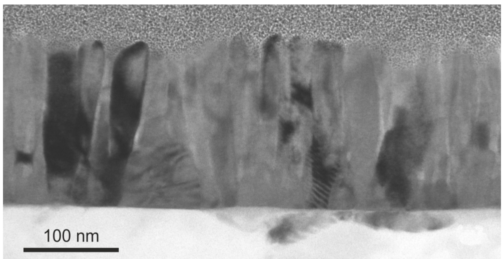

(c) TEM image of $d = 170$ nm sample

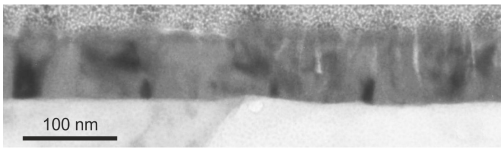

(d) TEM image of $d = 75$ nm sample

Figure 3.3: SEM and TEM images of Sr-doped samples with different thickness from set S2 as seen in Table 3.1. Average surface cluster diameter D_{avg} (acquired from AFM data) is 90 nm for $d = 75$ nm sample and 110 nm for $d = 170$ nm sample.

It is worth noting that column-shaped structure was obtained for all LSMO and LCMO films investigated in this work. Such nanostructured composition of the film as will be shown in the following chapters is essential for variation of their properties. Fig.3.3 presents TEM images of LSMO films grown with different thickness. One can see that column-shaped crystallites of the thinner films are not perfect structurally and are composed of many small crystallites separated by grain boundaries.

As seen in Tables 3.1, 3.2, the samples are grouped in few sets depending on growing conditions and measurements purposes. Substrate temperature was varied for Set S1 and Set S3 of LSMO films to achieve different average cluster diameter D_{avg} while Set S2 samples were varied by film thickness d. Set S4 consisted of 5 samples (S_{50}, S_{100}, S_{150}, S_{200}, S_{250}) prepared for the accelerated ageing investigations. Sr concentration was kept constant to achieve $La_{0.83}Sr_{0.17}MnO_3$ composition for all LSMO samples. LCMO Set C1 has been grown with different doping levels x. It

Table 3.1: Main characteristics of the $La_{0.83}Sr_{0.17}MnO_3$ samples used in this work.

	$La_{0.83}Sr_{0.17}MnO_3$				
	T_{dep},°C	T_m, K	ρ_m, Ωcm	d, nm	D_{avg}, nm
Set S1	700	240	1.6	420	240
	725	235	1.9	420	190
	750	245	0.8	420	285
Set S2	750	187	2.1	75	90
	750	235	1.2	170	110
	750	237	1.16	280	130
Set S3	650	160	53	400	110
	700	220	6.5	400	140
	750	235	1.8	400	170
	750	245	0.8	400	285
Set S4	750	235	1.4	400	250

Table 3.2: Main characteristics of the $La_{1-x}Ca_xMnO_3$ samples used in this work.

	$La_{1-x}Ca_xMnO_3$						
	x	T_{dep},°C	P_{dep}, Torr	T_m, K	ρ_m, Ωcm	d, nm	D_{avg}, nm
Set C1	0.218	775	5	220	8.2	320	110
	0.296	775	5	185	5.4	320	140
	0.41	775	5	130	2.8	320	210
	0.285	775	5	115	5.0	320	157
Set C2	0.28	775	3	175	19.3	300	100
	0.28	775	5	225	2.8	300	120
	0.27	775	7	225	2.8	300	120

has to be noted that LCMO film with $x = 0.285$ was textured with wider distribution of crystallite dimensions resulting in very broad phase transition range. MOCVD chamber pressure P_{dep} was varied for samples from Set C2.

3.1.3 Deposition of electrodes

After morphology and microstructure characterization was done, the electrodes of the samples were made by thermal deposition of Ag followed in-situ after a Cr sub-layer deposition. Cr film serves as adherent film among manganite and Ag for better contact. During the deposition the samples temperature was kept at 200 °C and pressure was $\sim 10^{-5}$ Pa. Finally, a thermal treatment at 400–450 °C for up to 1 hour in Ar atmosphere was carried out. It was demonstrated [74] that total contact resistance of so prepared manganite samples is $\sim 10^3$ times smaller in comparison with the resistance of the active area of manganite film and, thus, has no significant influence on the measurement accuracy. The prepared electrodes have a rectangular shape area of approx. 0.25 mm^2 with 50 µm distance between them as seen in Fig. 3.4.

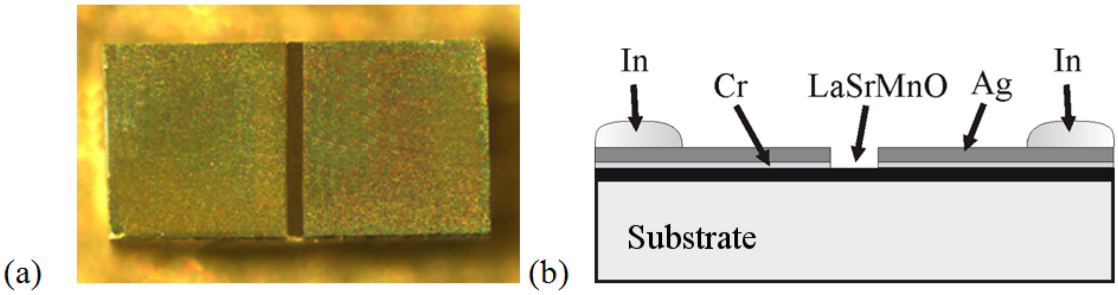

Figure 3.4: (a) Picture of the prepared sample, (b) profile of the sample with deposited electrode.

The Ag or Cu wires of 50 to 150 µm diameter where soldered to contact pads before the electrical measurements. Indium was used as soldering agent as it remains soft and malleable even in cryogenic temperatures. The wires would then be twisted to minimize the current induced by high pulsed magnetic field. The active surface of the sensor and the soldered area with electrodes were covered by polyethylene hot-melt adhesive or left uncovered for further ageing investigations.

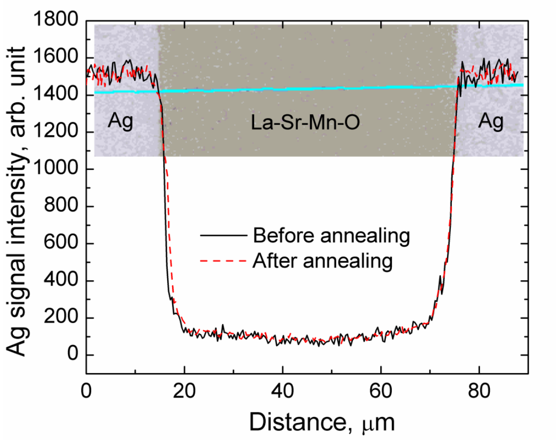

Figure 3.5: EDS line scan of Ag profile across the surface of the manganites film between the two electrodes. Background image is a SEM image of the sample surface and the scan line.

The thermal treatment applied during accelerated ageing of samples may cause silver atoms diffuse from the electrodes not only to manganite layer depth, but also toward the terminal. The latter phenomenon can be a source of in-time instability of the electrical parameters of the sensors. The silver distribution across the surface of the manganite film was measured by using a Scanning Electron Microscope with attached Energy Dispersive X-Ray Spectrometer (SEM/EDS) Hitachi TM3000. The line scan profiles acquired before and after annealing of the electrodes are shown in Fig. 3.5. It can be seen that the Ag concentration profile did not change after the annealing within the spatial resolution of the method (1 µm). This means that no appreciable diffusion takes place at temperatures up to 450 °C.

3.1.4 Investigation of resistivity in a wide temperature range

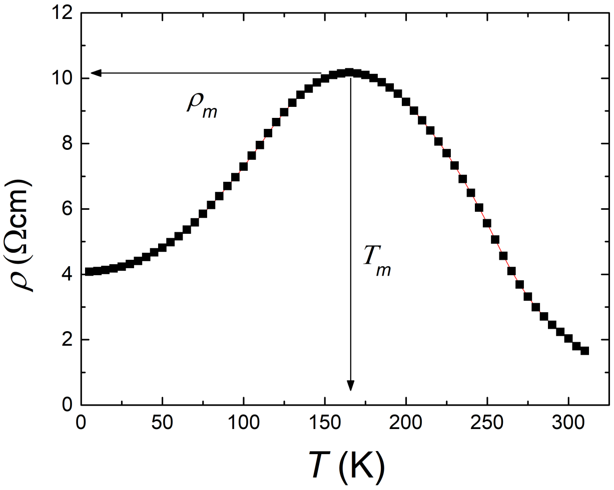

Figure 3.6: Typical resistivity *vs.* temperature characteristic of a manganite sample. T_m is the temperature of the resistivity maximum ρ_m.

After contact deposition the resistivity dependence on temperature (see Fig. 3.6) was investigated in a closed cycle helium gas cryocooler in the temperature range of 5 to 300 K. All samples exhibited the resistivity maximum separating metallic ($d\rho/dT > 0$) and semiconducting ($d\rho/dT < 0$) regions.

3.2 Measurement equipment and methods

Measurement equipment and methods used for the investigation of manganite films are listed in this section.

3.2.1 Measurement of resistance in high magnetic fields

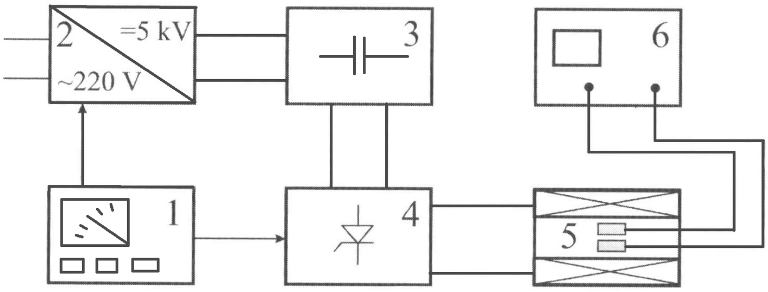

Figure 3.7: High magnetic field pulse generator block scheme.

The resistance dynamics of LSMO and LCMO films was investigated using pulsed magnetic field generator based on a capacitor bank discharge through a multi-shot magnetic field coil. The block scheme is presented in Fig. 3.7: 1 – Charge/Discharge control device, 2 – Capacitor bank charging unit, 3 – Capacitor bank, 4 – High power semiconductor thyristor switch, 5 – Coil, 6 – Measurement device (oscilloscope or in-house manufactured B-scalar meter). Due to the rectifying current-voltage characteristic of the thyristors, the system generates a current pulse of half sine shape with amplitudes up to 15 kA. This pulse is fed to the coil, inside of which a high magnetic field is generated. The amplitude of magnetic field is controlled by charge voltage in the capacitor bank while pulse length depends on coil dimensions and winding count as seen in Table 3.3.

The Coil #1 with steel casing was used to generate magnetic fields up to 25 T. The measurements in magnetic fields up to 60 T were performed at Dresden High Magnetic Field Laboratory (for more details of the setup see [P1]). For generation of short pulses (duration < 1 ms), special non-destructive (at least 100 pulses) coils were constructed for the resistance relaxation experiments after the magnetic field pulse was switched off. The coils were wound with Cu-Nb microcomposite wire (conductivity 65% IACS, strength UTS = 1.2 GPa, manufacturer — Boshvar

Table 3.3: Parameters of coils used in experiments.

	Coil #1	**Coil #2**
Pulse length	900 µs	260 µs
Inner diameter	14 mm	10 mm
Outer diameter	34 mm	19 mm
Length	48 mm	40 mm
Number of layers	4	2
Windings per layer	10	10
Total windings	40	20
Wire gauge	4.2 x 2.37 mm^2	3.8 x 2 mm^2

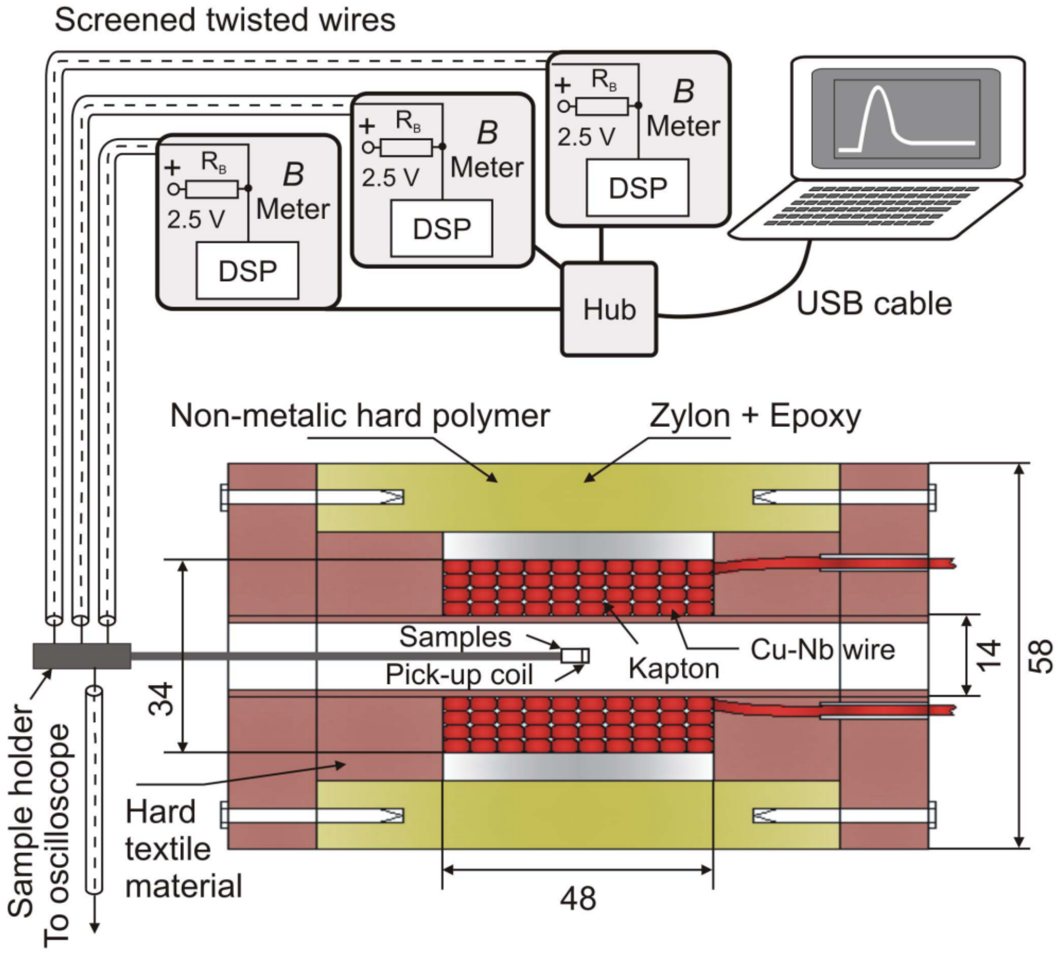

Figure 3.8: Measurement setup and schematic diagram of magnetic field coil. Dimensions are in millimetres.

Institute, Moscow), insulated with Kapton film and reinforced with Zylon fibre-epoxy composite. Coils consisted of 40 (as seen in Fig. 3.8) or 20 turns (10 in each layer) with dimensions as shown in Table 3.3. In order to avoid a 'tail' of the magnetic field pulse after the current is switched-off [75], a non-metallic outer casing was made from polyamide material which allowed us to produce half sine waveform magnetic field pulses with amplitudes of up to 14 T (see Fig. 3.9). The coils prepared in this manner were mounted into a double walled, 10 mm thick steel or polyamide container which was pre-cooled with liquid nitrogen.

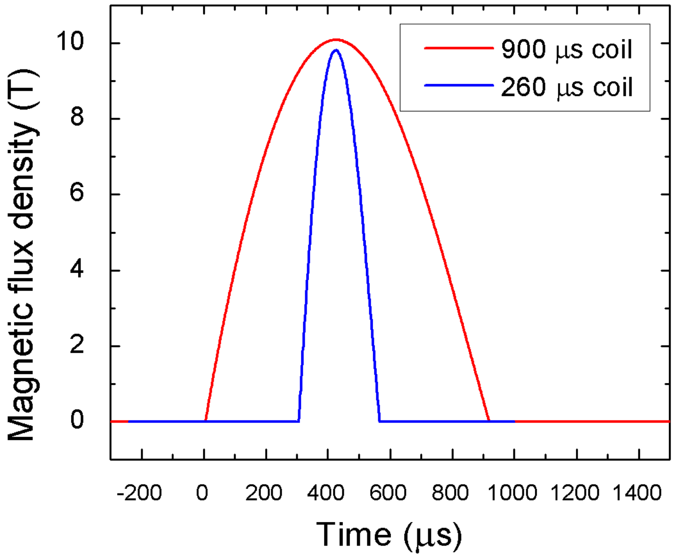

Figure 3.9: Example of typical magnetic field pulse form for 900 μs and 260 μs coils as measured by inductive sensor based on Faraday's law.

During the experiments, up to three manganite samples together with a search coil magnetometer used for the magnetic field measurements were placed inside the non-destructive coil. The parameters of the coil assured the axial homogeneity of magnetic field is accurate to 5% within 1 cm region at the centre [6, 76] where the samples and magnetometer were placed about 5 mm apart. To calculate magnetic flux density values during pulse the signal from the search coil magnetometer was integrated by RC circuit and measured by oscilloscope. According to Faraday's law, the voltage induced in search coil is proportional to rate of magnetic flux density change in the main coil as [77]:

$$U(t) = n\frac{dB}{dt}S, \tag{3.1}$$

where n and S are winding count and cross sectional area of windings, respectively. The voltage at RC integrator output is then

$$U_{int}(t) = \frac{1}{RC}\int_0^\tau U(t)\exp\Big(-\frac{\tau - t}{RC}dt\Big), \tag{3.2}$$

where τ is the duration of magnetic field pulse. Given R and C values are selected to satisfy $\tau \ll RC$ then the final value for magnetic flux density is calculated according to Eq .3.1:

$$B = \frac{RC}{nS}U_{int}. \tag{3.3}$$

During experiment the magnetic field is applied in the manganite film plane perpendicular to the current direction. Each manganite sample is connected to up to three independent measurement devices (B-meters, see Fig. 3.8) through a twisted pair cable. A 6.2-kΩ ballast resistor R_B is connected in series to the each sample having resistance R_S which can be calculated from Eq. 3.1.

$$R_S = \frac{U_m R_B}{U_{sup} - U_m}. \tag{3.4}$$

The total voltage drop across both resistors ($R_B + R_S$) is 2.5 V. Electrical circuit is presented in Fig. 3.10. The output voltages corresponding to each sample's change of resistance during the magnetic field pulse are stored in the internal memory of the B-meter and transferred to the personal computer on software package request. For this purpose, the B-meters are connected using a duplex fibre optic data link

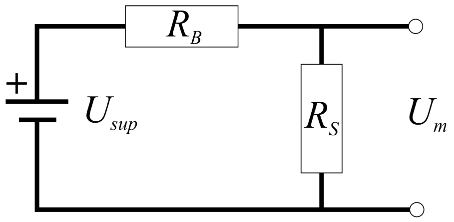

Figure 3.10: Equivalent electrical circuit used for resistance measurements in strong pulsed magnetic field.

to a hub that transformed and encoded the data to single data packet and sent it through USB cable to the personal computer. The resistance relaxation after the magnetic field pulse is switched off is investigated at various temperatures and magnetic fields. The time instant of switching off the field can be clearly seen by the spike in the resistivity curve (it is also seen in the magnetic induction curve). It is related with interference generated by closing of the thyristor in the current oscillating circuit of capacitor bank – magnetic field coil system.

3.2.2 Resistance relaxation anisotropy measurement setup

The resistance relaxation anisotropy of samples was tested by changing the orientation of film plane in the magnetic field coil in respect to magnetic field direction. Fig 3.11 presents all three configurations of the sample mounted inside the coil.

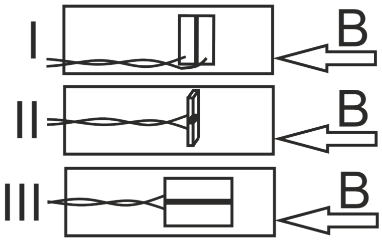

Figure 3.11: Three sample orientations as used in experiments.

3.2.3 Film ageing measurement setup

The accelerated ageing of the uncoated samples was performed by their cycled annealing during 1 h at different temperatures T_a (50, 100, 150, 200 and 250 °C) in argon atmosphere. For simplification the samples were numbered according to the annealing temperature (S_{50}–S_{250}). Sample which was kept at room temperature without additional annealing was used as a reference (S_r). After each annealing cycle the samples were slowly (during ~30 minutes) cooled to the room temperature and characterized. Then, after a total of 8 h of annealing, all samples were aged for a long-term (approximately for 2 years) by keeping them at room temperature in a silica gel filled desiccator. The sample S_{100} used for long term ageing was annealed at $T_a = 100$ °C for two different time periods – 8 h and

24 h. The resistance and magnetoresistance of these samples were periodically measured every 1–2 months. The characterization of the samples was performed by measuring the resistivity and magnetoresistance (MR) in a temperature range of 5–315 K and magnetic field range $B = 0$–0.8 T using a closed cycle helium gas cryocooler and electromagnet. For the magnetoresistance measurements in higher magnetic fields two methods were used: electromagnet together with installed thermostat based on Peltier effect for measurements at temperatures 265–315 K and magnetic fields up to 2.4 T, and pulsed magnetic field generator for MR measurements up to 25 T.

The accelerated ageing of the coated samples (as illustrated by Fig. 3.12) was performed by annealing for ∼50 h. The stability of coated annealed samples was then verified by long-term ageing (7 months) using same methodology as for uncoated samples.

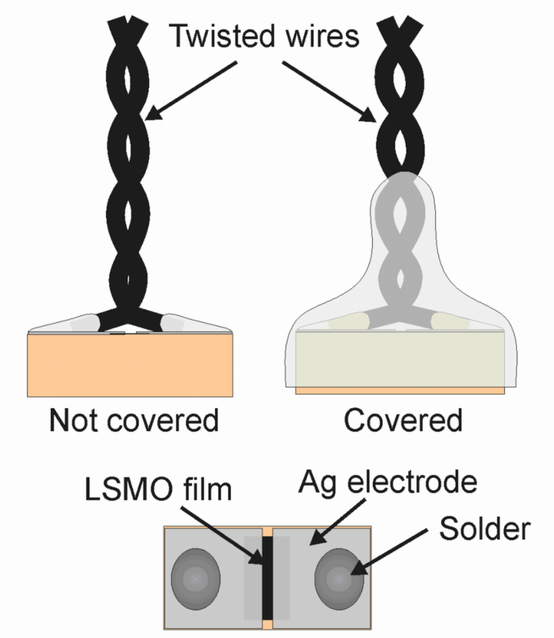

Figure 3.12: Top view and cross-section of covered and uncovered sensor.

Chapter 4

Results

4.1 Magnetoresistance

The nanostructured $\mathrm{La_{1-x}Sr_xMnO_3}$ (LSMO) films which exhibit the colossal magnetoresistance effect were successfully used for the development of CMR-B-scalar sensors [2, 3] operating at room temperatures and measuring the absolute magnitude of the magnetic flux density during high magnetic field pulses. For other application, as it was mentioned in the introduction, sensors operating at cryogenic temperatures and measuring high magnetic fields are required. It was found that the highest MR values usually are obtained close to T_C [15, 78]. Therefore, for low temperature applications the $\mathrm{La_{1-x}Ca_xMnO_3}$ (LCMO) films having lower T_C in comparison with the LSMO ones might be of greater interest. It is important to find out which composition – $\mathrm{La_{1-x}Sr_xMnO_3}$ or $\mathrm{La_{1-x}Ca_xMnO_3}$ – is favoured for magnetic field sensing applications at various temperature ranges. Also, the sensitivity of the sensors to magnetic field depends on magnetoresistance magnitude. For measurement of low fields, the 'Low field magnetoresistance' (LFMR) effect usually attributed to spin-polarised tunnelling [39] is important. For measurement of magnetic fields close to megagauss (High field magnetoresistance, HFMR), the magnetoresistance saturation with magnetic field plays very important role.

Therefore, in this section the results of LFMR and HFMR dependences on magnetic field value and temperature for the LSMO and LCMO films are presented and analysed. The influence of chemical composition and deposition conditions of the film to the MR values is discussed.

4.1.1 Low-Field Magnetoresistance

The low-field magnetoresistance (LFMR) of LSMO films varied by deposition temperature T_{dep} (Set S1 in Table3.1) in wide temperature range was measured using a closed cycle helium gas cryocooler and electromagnet. The measurements were executed by changing the orientation of the samples: magnetic field is perpendicular to the film plane or magnetic field is in plane with film surface. Magnetoresistace values were calculated using Eq.2.8. The results of low-field magnetoresitance measurements of nanostructured LSMO films at 200 K temperature are presented in Fig.4.1. Magnetoresistance curves for sample where magnetic field is in plane with surface can be used to evaluate the influence of spin-polarised tunnelling which is responsible for sharp increase of MR for polycrystalline manganites in weak magnetic field, or low-field magnetoresistance (LFMR). The LFMR was defined in the configuration $B||$film plane (see Fig.4.1 a)) where it can be extracted by extrapolating MR slope at $B > 0.15$ T to intersection with $B = 0$ T axis. In our case the LFMR is equal to -2 % for sample grown at 700 °C (T_m= 240 K) and -1.4 % for sample grown at 750 °C (T_m= 245 K). It is clear that absolute

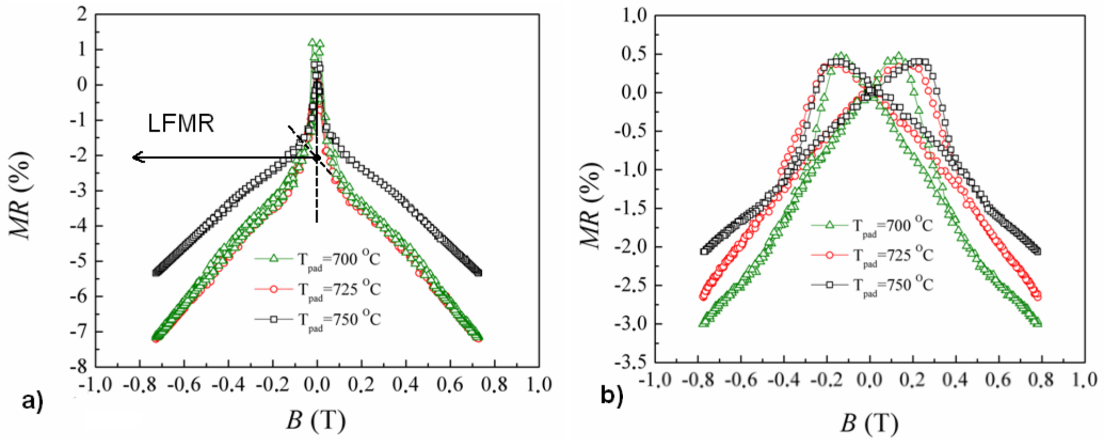

Figure 4.1: Magnetoresisitance dependencies on applied magnetic field at 200 K temperature from LSMO samples: a) magnetic field is in plane with film surface; b) magnetic field is perpendicular to film surface.

MR values for sample grown at 750 °C (T_m= 245 K) are lower than for two other samples, which give very similar MR characteristics. We also observe the anisotropy of magnetoresistance in parallel (Fig.4.1 a)) and perpendicular (Fig.4.1 b)) fields. MR when magnetic field ($B > 0.5$ T) is applied in plane with sample is almost 3 times higher than MR of sample in perpendicular field. Both orientations give tiny positive MR in very small fields of $B < 0.4$ T – at first resistance is increasing when magnetic field is increased and only later starts to drop. Hysteresis is observed in perpendicular field $B < 0.4$ T and parallel field $B < 0.05$ T. Coercive field, which is needed to reorient the magnetic domains in opposite direction, can be calculated from MR dependency of film in parallel field. It is equal to value of magnetic induction at peak of the MR curve: 22 mT for sample grown at 700 °C (T_m = 240 K), 12 mT for sample grown at 750 °C (T_m = 245 K). Similarly, demagnetisation field, which is needed to reorient the magnetic domains from perpendicular plane orientation to parallel, can be calculated from MR dependency of sample in perpendicular field: 135 mT for sample grown at 700 °C (T_m = 240 K), 180 mT for sample grown at 750 °C (T_m = 245 K).

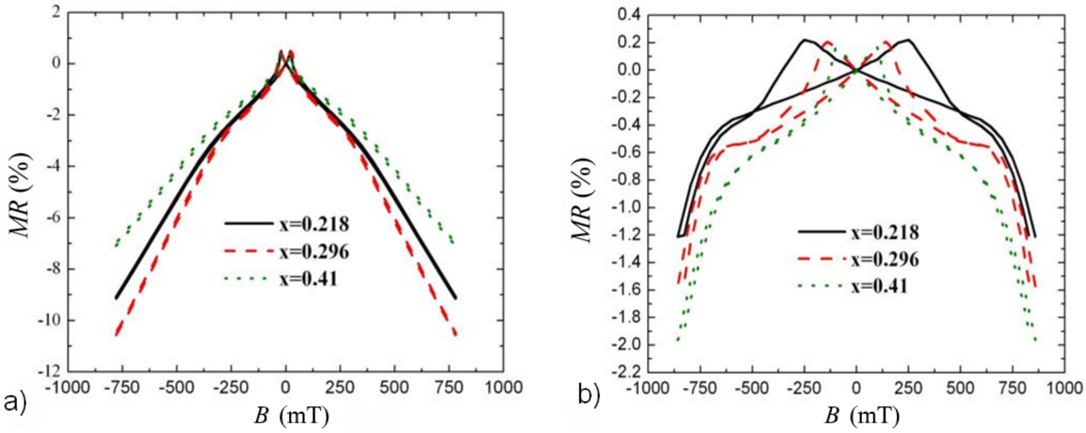

Figure 4.2: Magnetoresisitance dependencies on applied magnetic field at 200 K temperature for LCMO samples: a) magnetic field is in plane with film surface; b) magnetic field is perpendicular to film surface.

The low-field magnetoresistance of LCMO films varied by doping level x (Set C1 in Table 3.2) was also investigated using the same methods as for LSMO films. The results of low-field magnetoresitance measurements of nanostructured LCMO film at 200 K temperature are presented in Fig.4.2. When magnetic field is in-plane with sample surface: sample of $x = 0.41$ has lowest sensitivity while $x = 0.296$ composition offers greatest MR. We can see that for Ca-doped samples with higher x the MR is also higher (film is more sensitive to magnetic field) at same perpendicular magnetic field values. Anisotropy is more pronounced compared to LSMO samples. Lowest anisotropy was observed for film with highest doping level ($x = 0.41$). MR when low magnetic field ($B > 0.5$ T) is applied parallel with sample can be up to 10 times higher than MR of sample in perpendicular field. Both orientations give some amount of positive MR in very small fields of $B < 0.5$ T: at first resistance is increasing when magnetic field is increased and only later starts to drop. Hysteresis is observed in perpendicular field $B < 0.5$ T and parallel field $B < 0.05$ T. Coercive field for reorientation of the magnetic domains in opposite direction was determined at 24 mT for all samples. LFMR values of LCMO samples were in the range of $-(10-15)$ % at low temperatures. Demagnetisation field, which is needed to reorient the magnetic domains to be perpendicular to the plane of the film was 250 mT for the sample grown with $x = 0.218$ ($T_m = 220$ K), 140 mT for sample with $x = 0.296$ (T_m= 200 K) and 100 mT for $x = 0.241$ sample ($T_m = 160$ K). It has to be noted that demagnetisation field is higher for LCMO samples in comparison to LSMO ones. Taking into account that film thickness of LSMO and LCMO are similar ($\sim 300 - 400$ nm) and more than 100 times smaller in comparison to the distance between electrodes (50 µm), one can expect that different demagnetization field values have to be explained by long-range magnetic coupling in the film plane. For LCMO films grain boundaries were found to be narrower in comparison to the LSMO films. As a result, the in-plane coupling for these films has to be higher and demagnetization field is larger. The crystallites of LSMO films are separated by wider GBs and in-plane magnetic coupling can be destroyed more easily. Therefore, the crystallites in LSMO film can behave as separate columns interacting magnetically not so strong as in the LCMO case. As a result, the demagnetisation field for LSMO is smaller.

4.1.2 High-Field Magnetoresistance

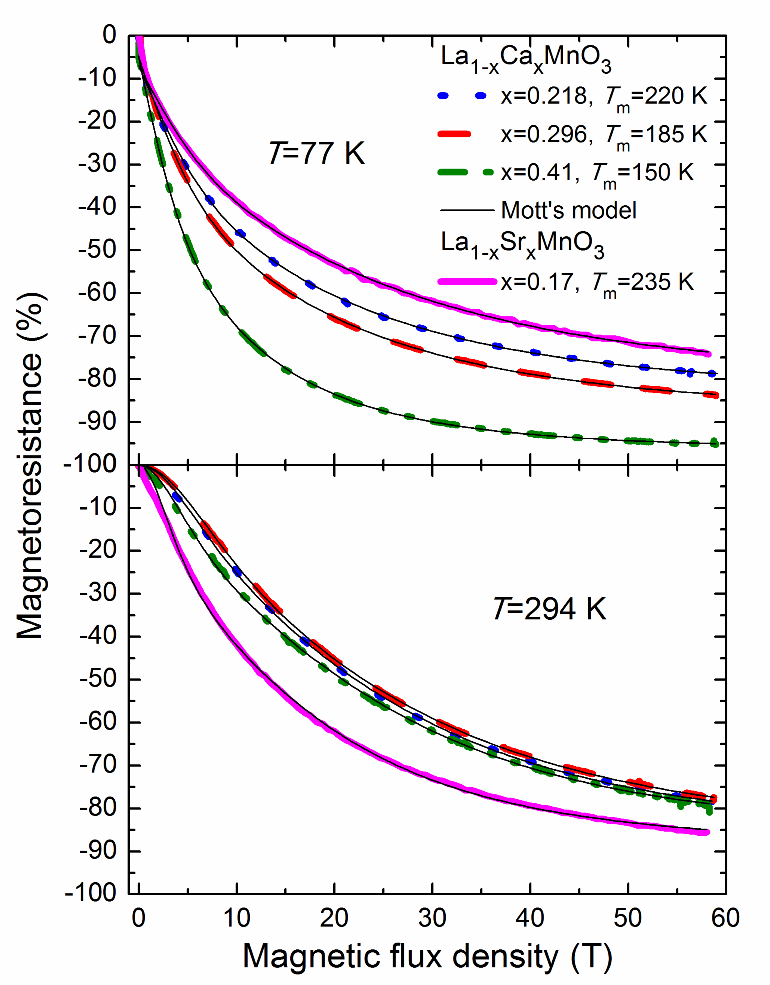

Figure 4.3: The magnetoresistance-magnetic flux density dependences in the ferromagnetic (77 K) (a) and paramagnetic (294 K) (b) phases of LCMO and LSMO films having different composition x. Thin solid curves represent fitting results to the modified Mott's hopping model: using Eq. 4.1 at 77 K, and using Eq. 4.2 at 294 K.

The magnetoresistance of the LCMO and LSMO films was investigated in pulsed magnetic fields up to 25 T in the temperature range 77–300 K (for setup details see Chapter 3) and up to 60 T in the temperature range 1.5–294 K (for setup details see [6]). The dependence of magnetoresistance on the magnetic flux density B is presented in Fig.4.3 both in the ferromagnetic (77 K) and paramagnetic (294 K) phases for LCMO films with various doping levels and compared with the LSMO one. It is evident that the MR at 77 K has higher magnitude values than in the LCMO films with larger crystallites (larger x). At 294 K, the highest MR magnitude values are obtained for the LSMO films. Therefore, for the development of magnetic field sensors operating at low temperatures, the LCMO films are preferable.

It was demonstrated that a modified Mott's hopping model [31] could be used to analyse magnetoresistance of such films in a wide range of magnetic fields. According to this model, the MR in the ferromagnetic (FM) state is supposed to scale with the Brillouin function, $\mathcal{B}$, while in the paramagnetic (PM) state with $\mathcal{B}^2$. It was shown that a simple approach where both nano-crystallites and inter-cluster boundaries are connected in series could be used for the LSMO films [3]. Taking into account that our investigated films are composed of column-like crystallites separated by grain boundaries (see TEM images in Fig.3.3), we applied such model for the nanostructured films and analysed the magnetoresistance by the sum of the two contributions – crystallites (C) and grain boundaries (GB):

$$MR = f \times A_C \times \mathcal{B}(\chi_C) + (1-f) \times A_{GB} \times \mathcal{B}(\chi_{GB}) + LFMR, \tag{4.1}$$

$$MR = f \times A_C \times \mathcal{B}^2(\chi_C) + (1-f) \times A_{GB} \times \mathcal{B}^2(\chi_{GB}). \tag{4.2}$$

Here Eq.4.1 and Eq.4.2 are given for the FM and PM states, respectively, f is the crystallite material fraction of the film, $(1-f)$ is the grain boundary material fraction. $\mathcal{B}(\chi)$ is the Brillouin function, $\chi_{C(GB)} = g \times \mu_B \times J_{C(GB)} \times B/k_BT$ is the ratio of magnetic and thermal energy, g is the Lande factor, μ_B is the Bohr magnetron, k_B the Boltzman constant, B the magnetic flux density, and T is the temperature. The magnetoresistance amplitudes A_C and A_{GB} as well as spin-orbit quantum numbers J_C and J_{GB} are treated as fitting parameters. Low-field magnetoresistance (LFMR) was obtained from low-field measurements in magnetic fields aligned parallel to the film plane. The presence of low temperature MR should originate from spin-dependent scattering of polarized electrons at the grain boundaries. Thin solid curves in Fig.4.3 represent fitting results both for the FM (77 K) and PM (294 K) states. The ranges of fitting parameters obtained for the LCMO films are presented in Table 4.1. For the LSMO film, the $f \times A$ values are similar, but J values are approximately 1.5 times higher. The obtained J values higher than magnetic moment of one manganese ion (> 2) indicate

Table 4.1: The ranges of fitting parameters obtained for magnetoresistance of the LCMO and LSMO films.

	LCMO		LSMO	
	$T = 77$K	$T = 290$K	$T = 77$ K	$T = 290$ K
$f \times A_C$	$-(31.3 - 45.4)\%$	$-(28.8 - 30.7)\%$	$\sim -23.7\%$	$\sim -33.4\%$
$(1-f) \times A_{GB}$	$-(44.9 - 45.7)\%$	$-(52.9 - 57)\%$	$\sim -49.7\%$	$\sim -52.9\%$
J_C	$7.5 - 11.8$	$27.2 - 37.8$	~ 7.5	~ 52.5
J_{GB}	$1.8 - 3.1$	$7.8 - 8.6$	~ 1.5	~ 10.7
$LFMR$	$-(5 - 7)\%$	-	$\sim -7\%$	-

that the crystallites and grain boundary material in these films behave like a superparamagnet of magnetically aligned polarons [31, 79, 80]. Also, it has to be noted that the MR of nanostructured films has tendency to saturate only at fields $>$ 50 T. Therefore, these films can be used for ultrahigh magnetic field measurements.

The dependencies of the MR on temperature at various magnetic flux densities are presented in Fig.4.4 for the LSMO ($x = 0.17$) and LCMO ($x = 0.17$) films. One can see that the MR shows high values not only close to metal-insulator transition temperature T_m (245 K for LSMO and 220 K for LCMO) but also down to cryogenic temperatures (1.5 K). The large MR values below the T_m in the investigated films are caused by the polycrystalline structure of the films. This feature is important for the development of magnetic field sensors operating in a wide range of temperatures.

MR temperature dependencies and the role of MOCVD chamber pressure P_{dep}. Properties of La-Sr(Ca)-Mn-O manganite films grown using the pulsed injection metal-organic chemical vapour deposition (PI MOCVD) technique depend not only on the Sr(Ca) content, but also on a number of processes occurring during the deposition. The PI MOCVD processes are extremely complex and involve a series of gas phase and surface reactions. The film growth rate, chemical composition and structure are determined by several parameters, primarily temperature of the substrate, the operating pressure (transported gas pressure) of the reactor as well as the composition and chemistry of the gas phase. A crucial factor that determines the relative importance of film properties is the pressure in the MOCVD reactor [81–83]. It was shown in [81] that kinetics, gas phase re-

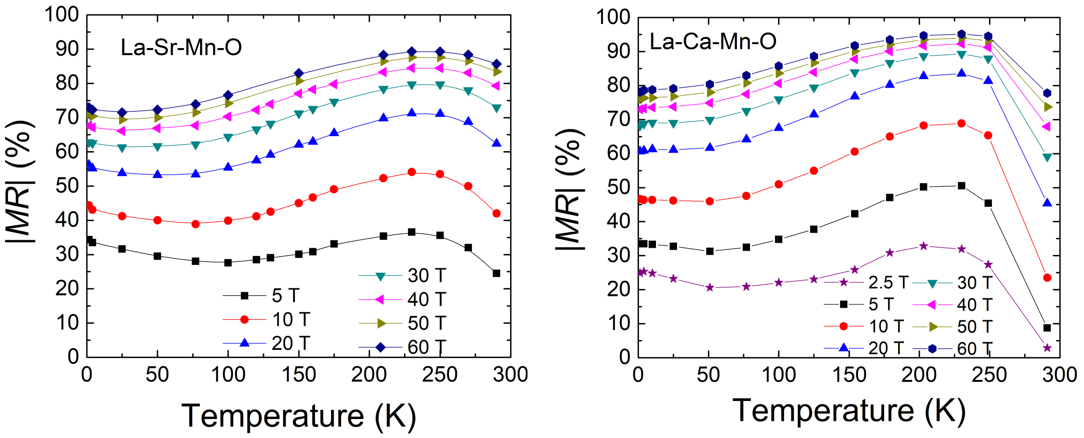

(a) LSMO

(b) LCMO

Figure 4.4: MR magnitude (absolute value) *vs.* temperature at different magnetic flux density dependencies of LSMO film grown at $T_{dep} = 750°\text{C}$, $P_{dep} = 5$ Torr and LCMO film grown at $T_{dep} = 775°\text{C}$, $P_{dep} = 5$ Torr.

actions and mass transport depend on the gas pressure and can play a significant role in deposition. Therefore, for development of magnetic field sensors, it is very important to determine the optimal deposition conditions of these films. In this section, the results of the investigation of the influence of total gas pressure during Pulse Injection (PI) MOCVD on magnetic properties of $\mathrm{La_{1-x}Ca_xMnO_3}$ films are presented.

The dependence of MR magnitude (absolute value) on the temperature at different magnetic flux density B is shown in Fig.4.5 for LCMO films grown at 3 and 7 Torr, respectively. The MR is defined by Eq.2.8. One can see that independently on the magnetic field value the maximum of MR is achieved at the temperature close to the transition temperature T_m. Large magnetoresistance of film is observed in a wide temperature range below the insulator-metal transition. This is in contrast to the monocrystalline manganites (or epitaxial films) exhibiting large MR values only in the vicinity of the T_m. The same general tendencies are observed for Sr-doped nanostructured film as seen in Fig.4.4a. Moreover, it is evident that in the low temperature range (1.3–200 K), the films grown at pressure of 3 Torr have higher MR than the films grown at 7 Torr. This is caused by greater structural imperfections of the films grown at low pressure. When pressure during film growth is increased, the GB regions become more homogeneous with lower defect concentration and, as a result, the resistivity of the sample decreases

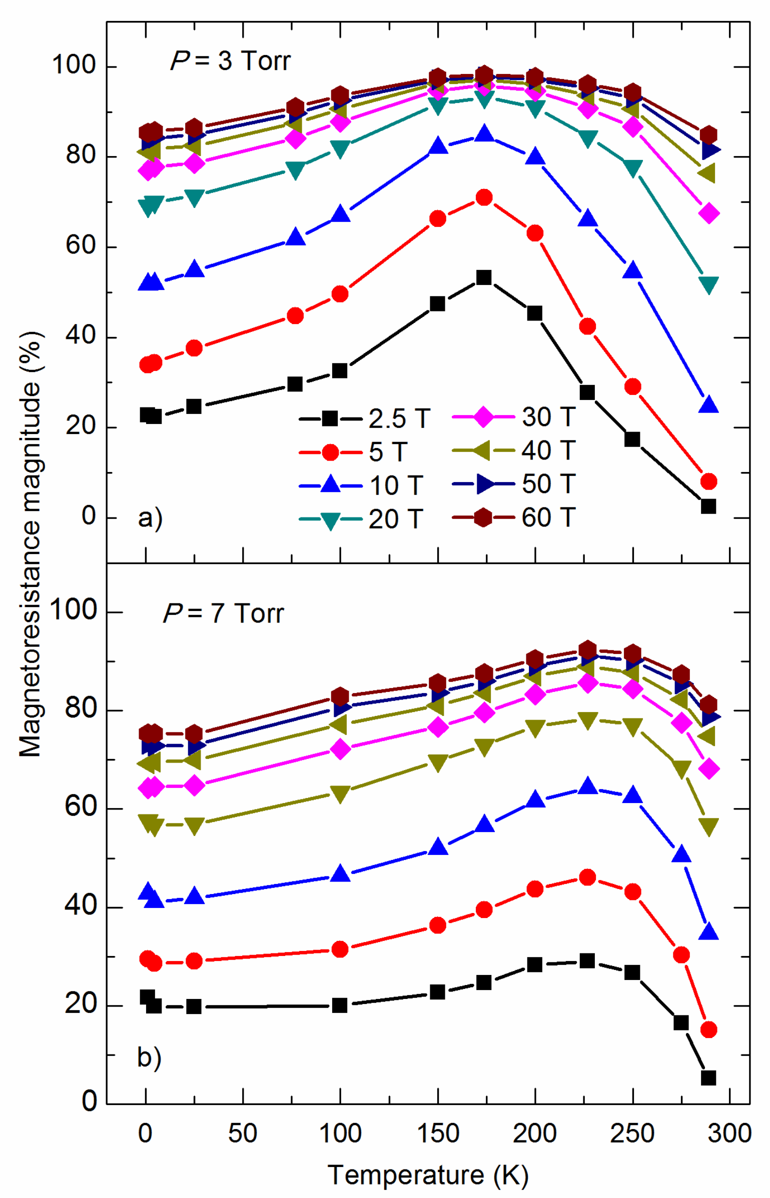

Figure 4.5: MR magnitude (absolute value) $vs.$ temperature at different magnetic flux density dependencies of LCMO films grown at different gas pressure: a) P_{dep} = 3 Torr, b) P_{dep} = 7 Torr.

and the MR also shows lower values.

The dependencies of MR magnitude (absolute value) on magnetic flux density B measured at temperatures of 100 K and 1.3 K by applying 60 T magnetic field pulses are shown in Fig.4.6 for LCMO films grown at 3, 5 and 7 Torr. One can see that in this temperature range the MR of the films depends non-linearly on the

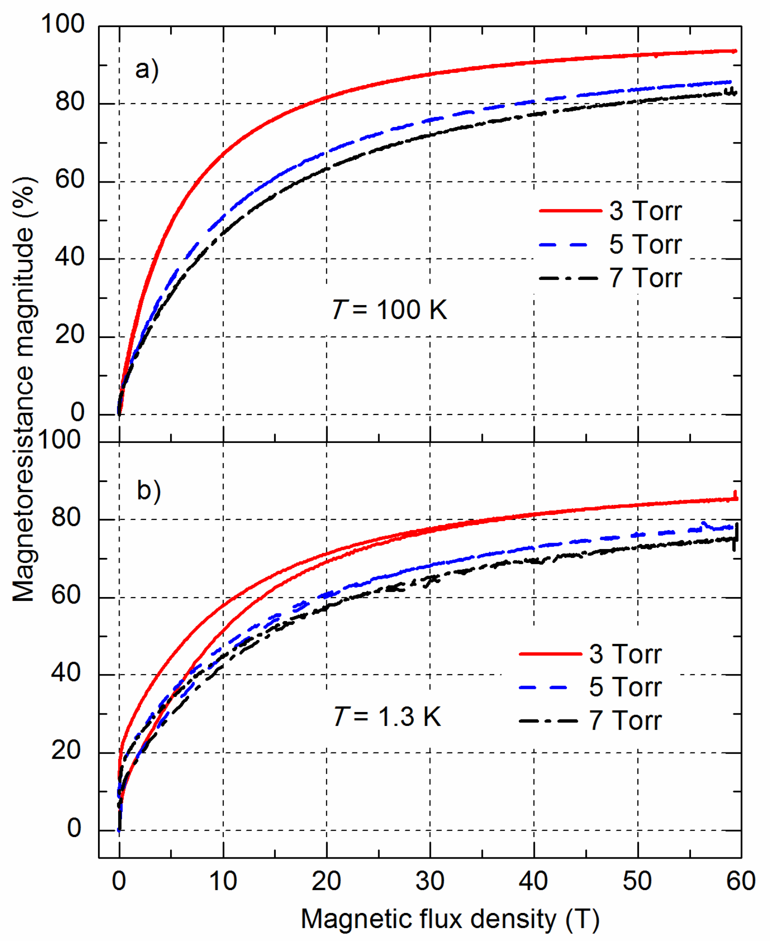

Figure 4.6: MR magnitude (absolute value) *vs.* magnetic flux density dependencies of LCMO films grown at different gas pressure; a) measured at temperature 100 K, b) 1.3 K.

magnetic field and does not fully saturate up to 60 T. The largest magnetoresistance slope is in the range of magnetic fields up to 10 T. At higher magnetic field (more than 20 T) the MR change becomes slower and tends to saturation. In addition, as can be seen from figure 4.6 b), at very low temperature (T = 1.3 K), hysteresis of MR is observed in magnetic fields below ~20 T. This phenomenon shows the memory effect at this temperature and is related with short-range interaction of the magnetic moments in disordered grain boundaries having spin-glass properties as will be discussed in more detail in section 4.2.4. It is evident that at cryogenic temperatures the manganite films grown at pressure of 3 Torr have the higher MR in comparison with films grown at 5–7 Torr.

For the development of magnetic field sensors operating at low temperatures in

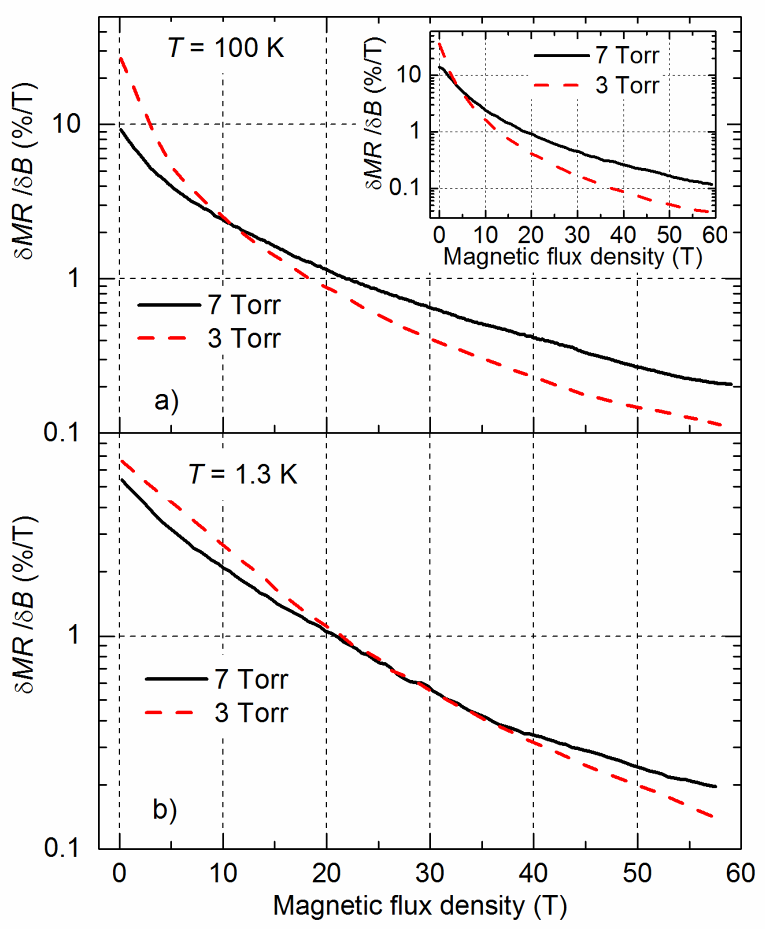

Figure 4.7: Change of magtenoresistance *vs.* magnetic flux density (sensitivity) for LCMO films grown at gases pressure 3 and 7 Torr measured at different temperature: a) 100 K and b) 1.3 K. Inset presents the same dependences measured at temperature Tm: 175 K for film grown at gases pressure 3 Torr and 225 K for film grown at 7 Torr.

wide magnetic field range, it is important to obtain the sufficiently high sensitivity of the sensors over the large range of magnetic fields. The sensitivity in this case can be described as change of magnetoresistance relative to change of magnetic flux density (derivative $\delta MR/\delta B$). These dependences *vs.* magnetic flux density are presented in Fig.4.7 for different temperatures: a) 100 K, b) 1.3 K. The inset presents same relation at temperatures where highest arbitrary MR values are observed: at 175 K for film grown at 3 Torr, and at 225 K for film grown at 7 Torr (see Fig.4.5). One can see that the highest sensor's sensitivity corresponds to the largest derivative of the magnetoresistance with respect to magnetic field.

Moreover, at various magnetic field ranges and temperatures, the sensitivity is different for films grown at various gas pressures. The higher sensitivity in the lower magnetic field range (< 10 T) exhibit films grown at pressure of 3 Torr (see Fig.4.7 a). These films could be used for production of magnetic field sensors operating in the temperature range 1.3–100 K and measuring magnetic fields up to 10 T. However, for measurement of very high magnetic fields (20–60 T), especially close to megagauss, the films grown at gas pressure of 7 Torr have to be used (see Fig.4.7). These films show higher sensitivity in high magnetic fields in the whole temperature range up to transition temperature T_m.

Therefore, during the growth of LCMO films used for magnetic field sensors operating at cryogenic temperatures, the PI MOCVD conditions have to be chosen depending on the range of the magnetic field which has to be measured.

4.2 Resistance relaxation upon removal of external magnetic fields

It was demonstrated, that polycrystalline manganite films exhibit magnetic memory effects which could be a disadvantage for magnetic field sensors operating at cryogenic temperatures [9, 48]. Therefore, it is important to minimize the magnetic memory effects which limit the speed and precision of such devices. It has been shown that the dynamics of the resistance relaxation in polycrystalline films upon removal of the external magnetic field reveal 'slow' remnant resistivity 'tails' [7, 8, 48, 84] which are usually attributed to the short-range interactions of disordered grain boundaries having spin-glass properties. The kinetics of this relaxation can be described by the simple Debye exponent [9], logarithmic [8, 48] or stretched exponential [7, 84] expressions. Investigations of the 'fast' resistance relaxation process are usually limited by the experimental setup due to the use of long (> 1 ms) magnetic field pulses. Therefore, for the application of manganite films for the development of fast magnetic field sensors operating at cryogenic temperatures, it is very important to determine mechanisms responsible for the resistance relaxation and to minimize the remnant resistivity.

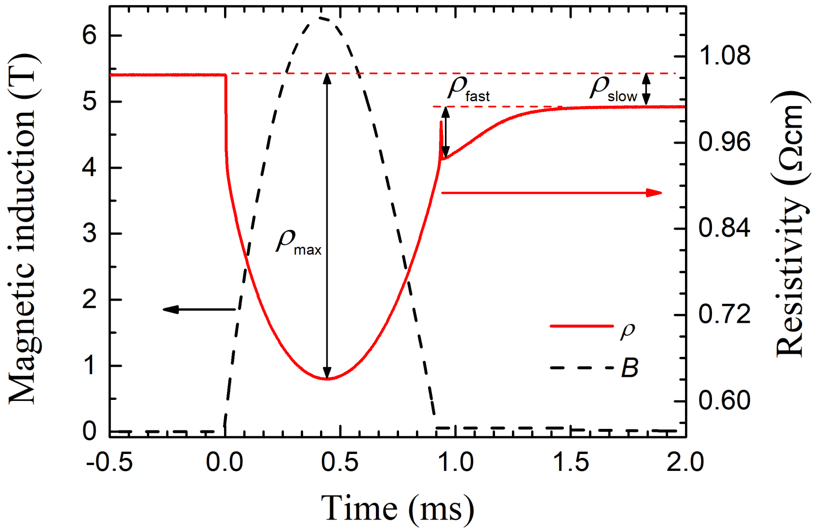

Figure 4.8: Magnetic field pulse (left scale) and resistivity change (right scale) during this pulse.

In this chapter the results of the investigation of the resistance relaxation phenomena in nanostructured $La_{1-x}Sr_xMnO_3$ and $La_{1-x}Ca_xMnO_3$ films are presented and analysed. The possibilities to minimize the remnant resistivity by changing the film composition or the deposition conditions are discussed.

The typical resistivity dynamics of manganite films after the application of a 0.9 ms duration magnetic field pulse with an amplitude of 6.5 T is presented in Fig.4.8. One can see that the relaxation processes occur in three different time scales: ultra-fast ($< 1\,\mu s$), which follows the magnetic field pulse; fast ($\sim 100\,\mu s$) and slow ($\geqslant 1\,ms$) which occur after the magnetic field pulse is switched off. For the development of magnetic field sensors, it is important to determine the conditions under which the 'fast' and 'slow' relaxation components can be minimized in order to ensure sufficient measurement accuracy. The results of this resistance (conductance) relaxation, namely, the temperature and magnetic field dependences of the characteristic time constants and remnant amplitudes of these processes, are presented and analysed below using the Kolmogorov-Avrami-Fatuzzo (KAF) and Kohlrausch-Williams-Watts (KWW) models discussed in Chapter 2.

4.2.1 'Fast' relaxation dynamics – KAF model

The typical conductivity relaxation of the La-Sr-Mn-O films, which was characterized as 'fast' and measured at low temperatures (ferromagnetic state) is presented in Fig.4.9. For the La-Ca-Mn-O films the relaxation kinetics were similar. The time instant $t = 0$ was chosen as the moment when the magnetic field pulse was switched off (see Fig.4.8.). Firstly, it was found that conventional Debye relaxation (exponential function) could not be applied to fit the experimental results. Then, after searching for possible solutions (as discussed in Chapter 2), a 'compressed' exponential decay provided within KAF model was chosen as the best fit function for parametrizing experimental results:

$$\sigma(t) = \sigma_{0fast} + \sigma_{fast} \exp[-(t/\tau_{fast})^{\beta}], \qquad 1 < \beta < 3 \tag{4.3}$$

where τ_{fast} is the time constant of the process, σ_{0fast} is the conductivity, when the 'fast' relaxation process is considered to be finished, and σ_{fast} is the remnant conductivity amplitude. The corresponding resistivity ($\rho_{fast} = 1/\sigma_{fast}$) is presented in Fig.4.8 for clarity.

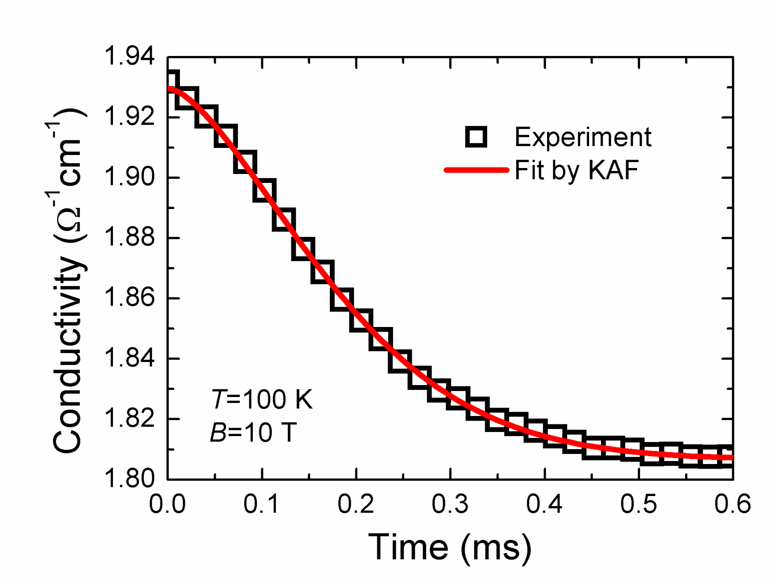

Figure 4.9: Conductivity of the 'fast' relaxation process of LSMO film. The squares are the experimental results, the curve represents the results when fitted to the KAF model. $\beta = 1.55$, $\tau_{fast} = 210\,\mu\mathrm{s}$.

The dependences of τ_{fast} and β on temperature that were obtained for two sets of the samples by fitting the experimental results using Eq.4.3, are presented in Fig.4.10.

For LSMO set S1 (slightly varied deposition temperature, Table 3.1) in Fig.4.10a one can see that at low temperatures ($\leqslant$ 120 K), the time constant is of the order of 200 µs and rapidly decreases with an increase of temperature. The values of exponent β show similar dependences: they are also higher at low temperatures (1.55 at 120 K), but approach $\beta = 1$ value when temperature is increased. At $T > T_m$ the amplitude σ_{fast} was below our measurement accuracy and thus we were not able to measure this time constant at higher temperatures.

LCMO set C1 (different doping levels, Table 3.2) presented in Fig.4.10b also show temperature dependences of time constant τ_{fast} and exponent β. One can see that these parameters decrease with increase of temperature in same manner as Sr-doped samples. This decrease becomes more abrupt in the phase-separation region of LCMO films where both ferromagnetic and paramagnetic phases coexist together [1, 85]. Paramagnetic part of the film increases when approaching T_m,

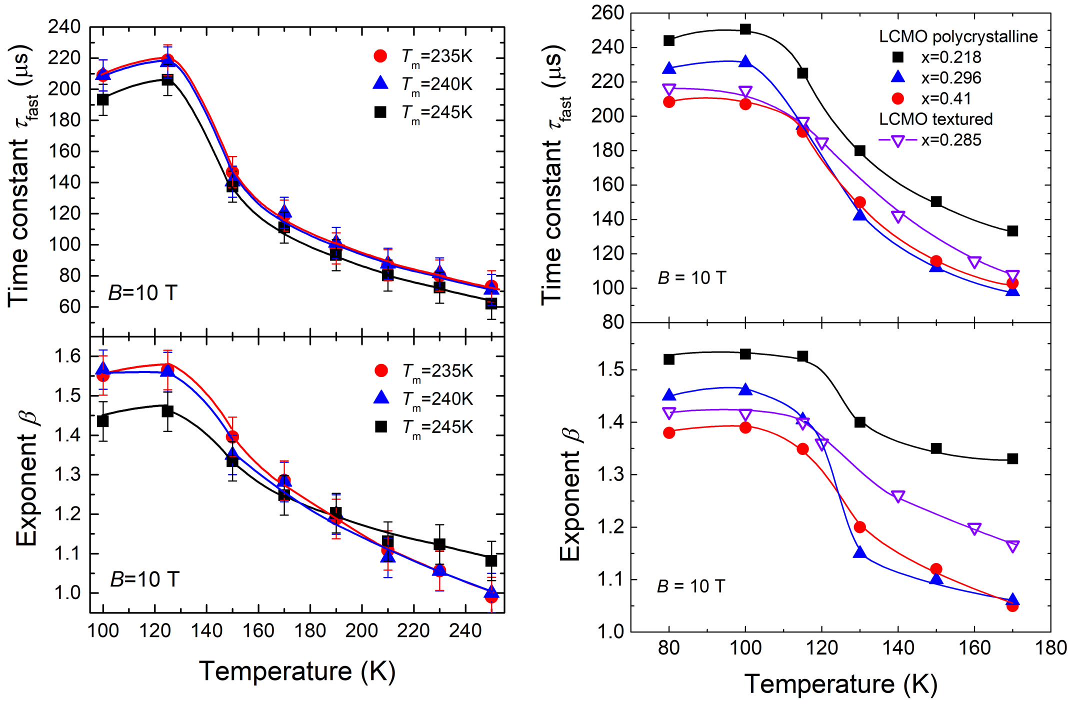

(a) LSMO samples. Set S1 in Table 3.1. (b) LCMO samples. Set C1 in Table 3.2.

Figure 4.10: Time constant τ_{fast} and exponent β dependences on temperature of 'fast' conductivity relaxation fitted to the KAF model for LSMO and LCMO samples. Symbols – experimental data, curves – fit to eyes.

therefore, the characteristic time of relaxation process decreases. The exponent β approaches value 1 (simple Debye exponent) close to T_m. Decay according to simple exponent indicates that relaxation process becomes uncorrelated at high temperatures.

These results can be explained as follows: In the paramagnetic state, the magnetization of the film is induced only by the application of the external magnetic field. The demagnetization process is determined by the thermal energy and follows in time the magnetic field pulse change. In the ferromagnetic state, the 'fast' relaxation process should be determined mostly by the reorientation (or collapse in slightly ferromagnetic manner) of the magnetic domains into their equilibrium state. It is known that for imperfect films, as in our case, the defects behave like pinning sites and, because of them, some reversed spins or domains firstly appear in the films. [7, 86]. These act as nuclei. Due to their short-range interaction, the adjacent spins reverse more often than others, and magnetic domains, once formed by external field pulse, start to collapse or change magnetization vector from these reversed spins. Such magnetization relaxation explanation rises from the Kolmogorov-Avrami (KA) model [12, 62] and was originally used by Fatuzzo (F) [51] to interpret the relaxation processes in ferroelectrics (for more details see Chapter 2). According to KAF model, it is worth mentioning two limiting cases: 1) when nuclei do not grow and relaxation follows the simple Debye exponent ($\beta = 1$); and 2) when domains grow extremely fast and relaxation takes place as a 'compressed' exponent $\sim \exp[-(t/\tau_{fast})^3]$. For the intermediate cases, it has been proposed that the experimental results can be fitted by means of Eq. 4.3 when exponent $1 < \beta < 3$. Our results gave the exponent values of $\sim 1 < \beta < 1.56$ for the measured temperature range 100–250 K (see Fig.4.10a). These β values indicate that the nucleation process is dominating in Sr-doped films and in Ca-doped films.

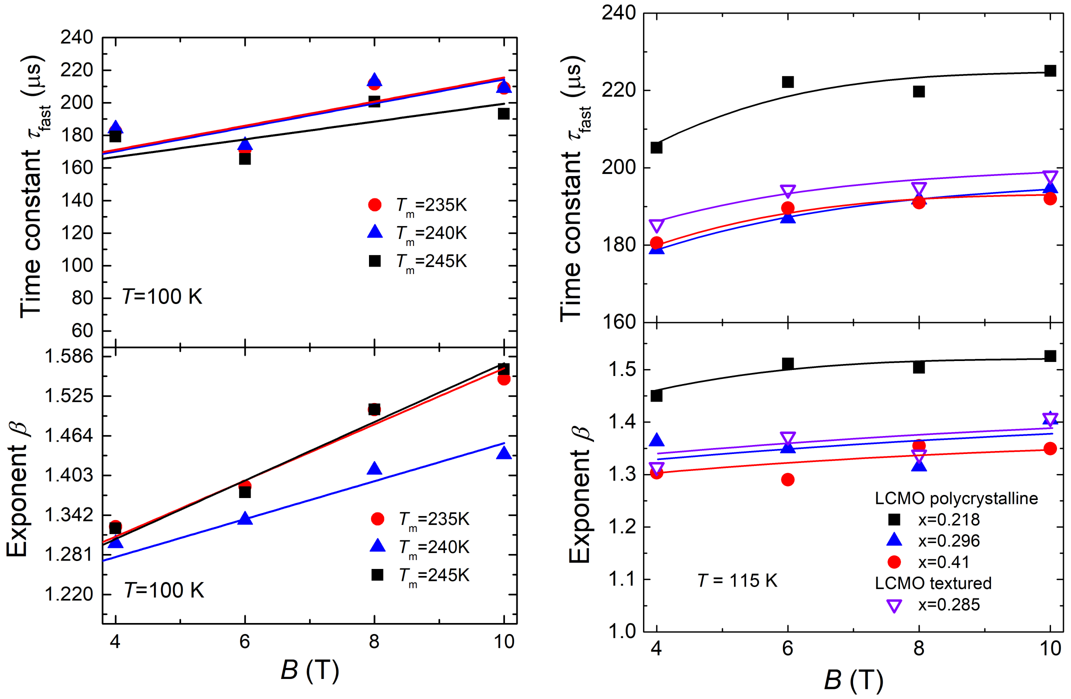

(a) LSMO samples. Set S1 in Table 3.1.

(b) LCMO samples. Set C1 in Table 3.2.

Figure 4.11: Time constant τ_{fast} and exponent β dependences on magnetic flux density (B) of 'fast' conductivity relaxation fitted to the KAF model for LSMO and LCMO samples. Symbols – experimental data, curves – fit to eyes.

Fig.4.11 presents dependences of fitting parameters τ_{fast} and β on magnetic flux density (B) at low temperatures (100–115 K). For Ca-doped samples one can see that characteristic time of the relaxation process is largest (220 µs) for the film with smallest $x = 0.218$ and highest T_m. This could be explained as follows. The relaxation measurement is performed at ferromagnetic state at a temperature ($T = 115$ K) far from the insulator-metal transition: $T/T_m = 0.5$. As a result, the relaxation of ferromagnetic domains in the crystallites of the film to their equilibrium state occurs more slowly if compare with the other films. Also, one can see that the τ_{fast} slightly increases with the magnetic field. This could be explained by better alignment of magnetic domains in higher magnetic field and thus longer time is needed for their magnetization relaxation. The parameter β, as predicted by KAF model [7, 87], is related to the ratio of domain wall propagation velocity during relaxation process versus the rate of nucleation (generation of nucleation centres). If the domain wall movement is predominant, the $\beta = 3$, if β is close to 1, the nucleation dominates [7, 87]. Small β values for all investigated samples show that the nucleation process is the predominant mechanism in the magnetic relaxation of LCMO films. The lower β values for films with lower T_m indicate that close to the phase transition temperature the domain wall movement is unlikely.

Dependences of fitting parameters τ_{fast} and β on magnetic flux density of LSMO films in Fig.4.11a show similar tendencies as Ca-doped samples, but are hardly comparable within the set. The variation of film growth conditions for set S1 was too small to give significant change in internal structure and, as a result, resistance and resistance relaxation measurements were inconclusive. In order to shed light upon the influence of disorder levels in LSMO film to 'fast' relaxation process, we investigated the relaxation effects on samples with the same chemical composition but varied film thickness d. Parameters obtained from fitting to KAF model are presented in Table 4.2. Here we also introduce the time $t_{1/2}$ parameter which is the time needed to relax half of the film remnant conductivity magnitude.

Table 4.2: Main parameters of 'fast' relaxation kinetics for LSMO films having different thickness.

Film thickness, nm	β	τ_{fast}	$t_{1/2}$
280	1.87	430	350
170	1.66	360	285
75	1.33	352	250

$t_{1/2}$ time is sometimes better as independent parameter to characterise the speed of relaxation compared to τ_{fast}, which is coupled with β. It was observed that relaxation parameters τ_{fast} and β tend to increase with gain in film thickness (if $d < 200$). As it was shown in Fig.4.12, the highest ρ_{max} is obtained for films of 75 nm thickness. It means that this film should have higher relative amount of disordered GB material. Indeed it is confirmed by SEM and TEM images of $d = 75$ nm and $d = 170$ nm samples in Fig.3.3. The TEM images demonstrated the complex structure of the films: column-shaped crystallites having width of 30–70 nm were separated by a 3–10 nm thickness grain boundaries (GBs) (evaluated by High-Resolution TEM). The thicker films were composed of rectangular shaped columns spread throughout the whole thickness of the films with their long axis perpendicular to the substrate, while the crystallites of thinner films were smaller and had rougher edges. One can see that the thinner is the film, the faster is relaxation process (smaller $t_{1/2}$). The exponent β is found to be closer to 1, when film thickness decreases. This dependence could be explained by the fact that thinner films have more defects and inhomogeneity compared to thicker films. The imperfections act as pinning centres providing more channels to return to equilibrium and, as a result, magnetic relaxation is faster. The main relaxation mechanism in thinnest films should be the domain nucleation.

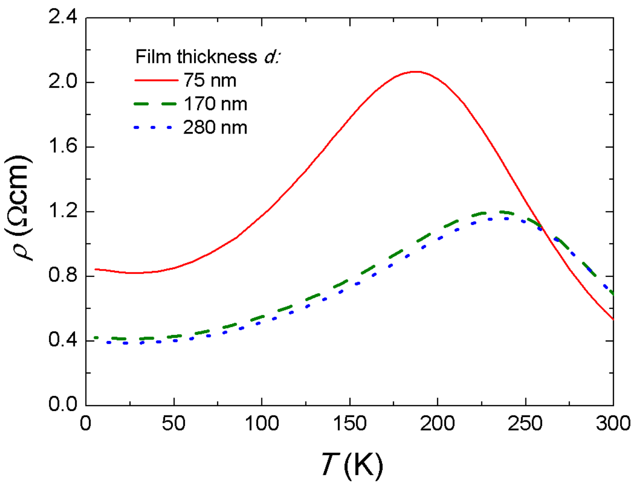

Figure 4.12: Resistivity characteristics of LSMO manganite samples with varied film thickness. See set S2 in Table 3.1.

4.2.2 Remnant resistivity of ‘fast’ relaxation

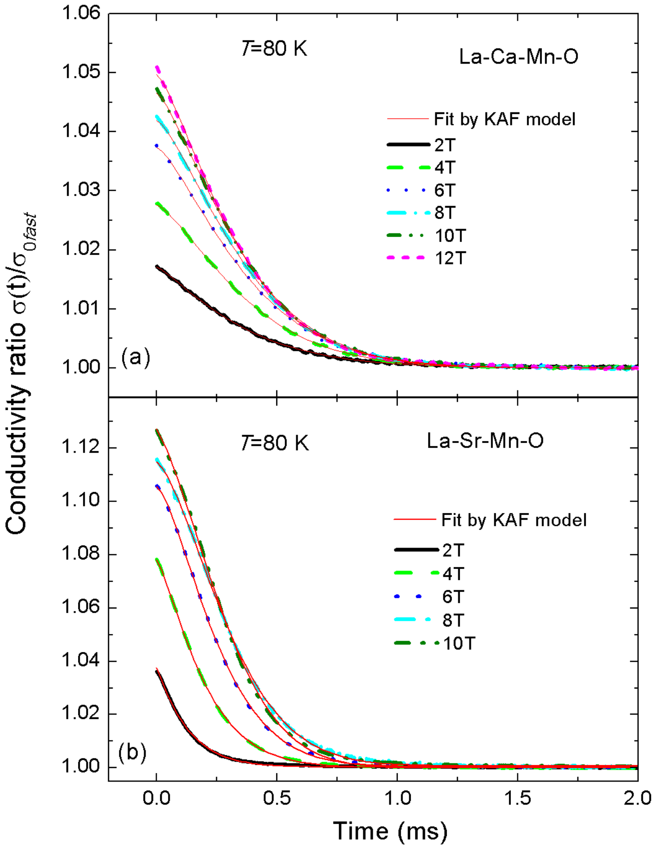

Figure 4.13: Remnant conductivity ratio kinetics of LCMO (a) and LSMO (b) films after removal of magnetic field pulses having different peak amplitudes. $T =$ 80 K.

It is very important for the development of magnetic field sensors that it has to be cleared up how exactly the remnant resistivity (after the magnetic field pulse is switched off, see Fig.4.8) depends on the magnetic field value and ambient temperature. We investigated the dependences of the absolute values as well as relative part of the ‘fast’ component in respect to the maximal resistivity change (see Fig.4.8).

In order to clear up the influence of external magnetic field magnitude on remnant relaxation process, we applied magnetic field pulses with different amplitudes in the range of 2–12 T. Fig.4.13 presents remnant relaxation ratio of the thickest investigated films having similar doping level ($x_{Sr} \approx 0.17$, $x_{Ca} \approx 0.2$) upon application of magnetic field in film plane direction: (a) 280 nm thickness La-Ca-Mn-O films; (b) 350 nm thickness La-Sr-Mn-O films. One can see that normalized remnant conductivity amplitude is higher for LSMO films in comparison with the LCMO ones and increases with increase of magnetic flux density. However the increase of magnitude of remnant conductivity is not linear: it has tendency of saturation at fields higher than 8-10 T. Such behaviour is probably related with nucleation and reorientation of magnetic domains in column-shaped crystallites (as seen in Fig.3.3c). Magnetoresistance of crystalline manganites has tendency to saturation at about 10 T, while nano-structured films having disordered grain boundaries show magnetoresistance increase with field up to megagauss [3].

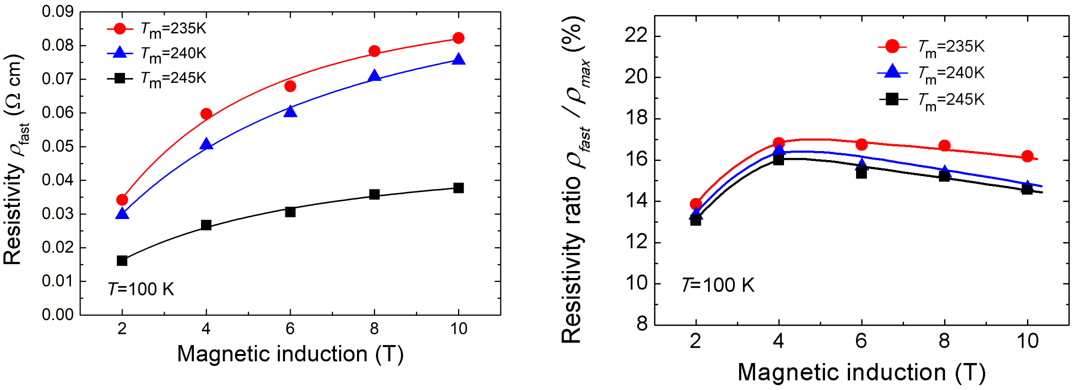

(a) Absolute resistivity.

(b) Relative resistivity.

Figure 4.14: Absolute and relative remanent resistivity dependences on magnetic field of 'fast' relaxation processes for LSMO samples with different T_m.

La-Sr-Mn-O films. The absolute values of the remnant resistivity of the 'fast' relaxation processes *vs.* magnetic inductance for LSMO set S1 are presented in Fig.4.14a. This component increases with an increase of the magnetic field and begins to saturate at fields higher than 10 T. Its relative part amounts to approximately 16 % of the whole resistivity change at 4 T and decreases only slightly with an increase of the magnetic field (Fig.4.14b). Since this component is assumed to be related to the reorientation of the magnetic domains starting with reversed spin nuclei formation at the pinning centres after the magnetic pulse is switched off, it follows that the higher the magnetic field that is applied, the higher is the magnetization induced by the pulse and the part of it which has to be reoriented after the pulse is switched off becomes larger. It should be noted that the relative part of the remnant resistivity of 'fast' relaxation component decreases with

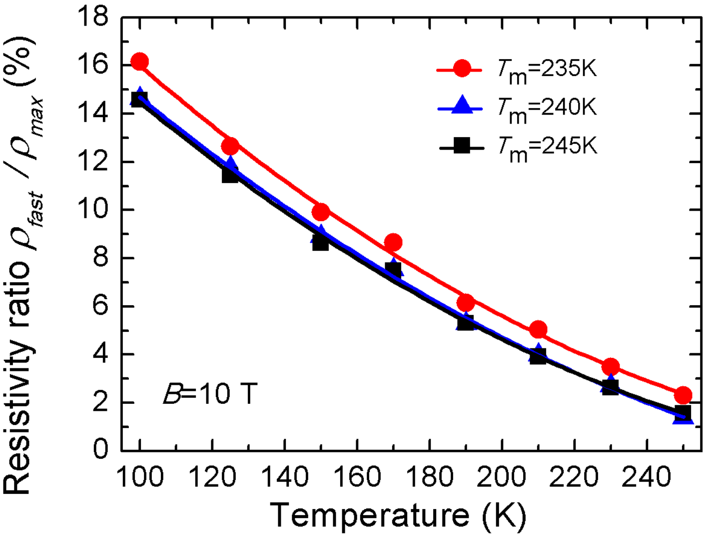

Figure 4.15: Temperature dependency of relative remnant resistivity of 'fast' relaxation process for three LSMO samples with different T_m.

temperature and is less than 2 % when approaching T_m (see Fig.4.15).

La-Ca-Mn-O films. It was found that the absolute values of the remnant resistivity of LCMO films also increases with magnetic flux density (Fig.4.16a) as in case of LSMO films (see Fig.4.14a). In order to compare the remnant resistivity of LCMO samples with different doping levels x, the dependences of normalized values *vs.* magnetic flux density were investigated (see Fig.4.16b). One can see that the normalized remnant resistivity increases with magnetic field and tends to saturation approaching 10 T, except for the textured film with $x = 0.285$ which increases almost linearly in the measured magnetic field range. It was obtained that remnant resistivity of 'fast' relaxation is proportional to the magnetoresistance ($MR = \rho_{max}/\rho_0$) of the films: the larger the MR, the larger ρ_{fast}/ρ_0 (see Fig.4.16b). The MR dependences on magnetic flux density are presented in Fig.4.17a. As a result, it was found that the ratio of remnant resistivity to the whole resistance change during the pulse is almost constant up to 10 T (as shown by Eq.4.4), except for the film with $x = 0.285$ (see Fig.4.17b).

$$\frac{\rho_{fast}}{\rho_0}/MR = \rho_{fast}/\rho_{max} \tag{4.4}$$

The obtained results could be explained as follows. It is known that for good

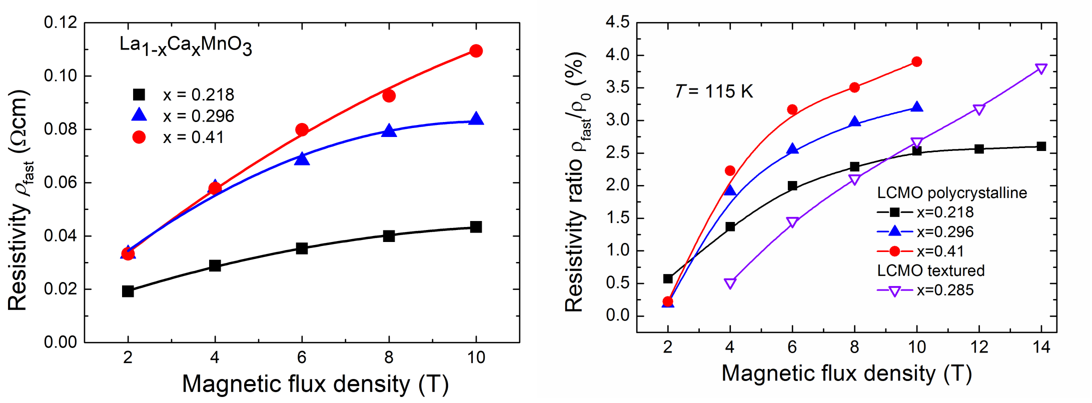

(a) Absolute resistivity

(b) Normalized resistivity

Figure 4.16: Absolute and relative remnant resistivity dependences on magnetic field of ‘fast’ relaxation processes for LCMO samples with different Ca content (x).

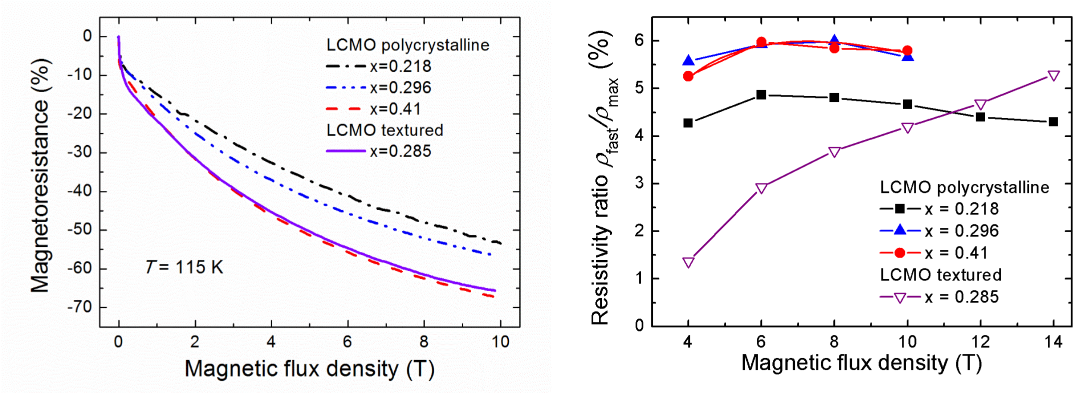

(a) MR

(b) ρ_{fast}/ρ_{max}

Figure 4.17: Magnetoresistance and remnant resistivity ratio *vs.* magnetic flux density for LCMO samples with different Ca content (x).

quality epitaxial manganite films magnetoresistance starts to saturate at ∼10 T [31], which means that almost all magnetic domains are aligned by the application of magnetic field. For the polycrystalline (nano-structured) films, the MR starts to saturate at much higher fields ($B > 50$ T [3]). Therefore, the amplitude of remnant resistivity is related with the magnetization and its relaxation of crystallites. At higher fields ($B > 10$ T) one can expect the decrease of ratio ρ_{fast}/ρ_{max} (see black square symbols in the Fig.4.17b). Such decrease was also observed for LSMO films at $B > 8$ T (see Fig.4.14b). The almost linear increase of relative

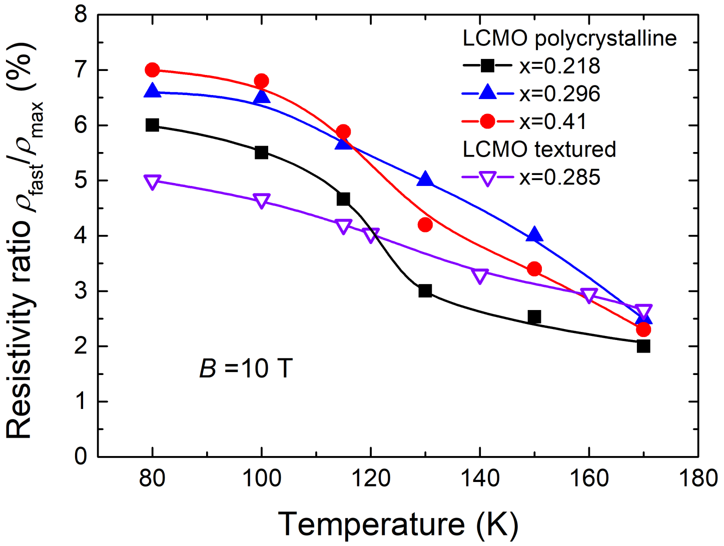

Figure 4.18: Relative remnant resistivity amplitude of fast relaxation processes *vs.* temperature for four samples with different Ca content (x). Set C1 in Table 3.1.

remnant resistivity for the film with $x = 0.285$ is more likely a result of highly inhomogeneous structure with small and large crystallite clusters having different magnetic properties. The smallest relative remnant resistivity at $B > 10$ T was obtained for the film with $x = 0.218$. This film exhibits and the smallest magnetoresistance. It is known that the smallest MR values in manganite films are usually obtained for the films having highest T_m values [88]. In our case this is the film with $x = 0.218$. Therefore, in order to minimize the magnetic memory effects in magnetic field sensors based on LCMO films and operating at cryogenic temperatures, the films with higher T_m have to be used. Despite the smaller MR in this case, it is still significant for the measurement of magnetic flux density in a wide temperature range. Fig.4.18 presents the temperature dependence of relative remnant resistivity at 10 T for all investigated films. The ratio ρ_{fast}/ρ_{max} for the film with $x = 0.218$ is 6 % at 80 K and decreases with increase of temperature what allows pulsed high magnetic field measurement in microsecond time scales with sufficient accuracy. The most significant decrease of relative remnant resistivity is observed at phase-separation region and temperatures close to T_m. It can be explained as follows. The relaxation of paramagnetic part of the films is very fast and is finished during decay of magnetic field pulse (~130 µs). As a result, after the pulse is switched-off we observe only the resistance relaxation of ferromagnetic part of the film, and this part decreases with temperature. The more slow change of the relative remnant resistivity for the textured film ($x = 0.285$) could be explained by highly inhomogeneous structure of this film resulting in very broad phase transition range.

Comparing LCMO and LSMO films at low temperatures in the context of possible sensor applications the LCMO film has an advantage due to lower remnant resistivity to MR ratio.

4.2.3 Anisotropy of 'fast' relaxation process

In this section, we present the results of an investigation of colossal magnetoresistance relaxation anisotropy in thin nano-structured La-Sr(Ca)-Mn-O films upon removal of pulsed magnetic field. As will be demonstrated, magnetic relaxation dynamics can reveal important information about possible relation between the film morphology and magnetic properties. The typical resistivity dynamics of the investigated manganite films after the application of a 0.9 ms duration magnetic field pulse with an amplitude of 10 T is presented in Fig.4.20 (LCMO film, left scale). The measurement is performed at temperature of 100 K when magnetic field is applied along three different directions in respect to the film plane and current direction (see Fig.4.19). The inset presents kinetics of remnant conductivity ratio $\sigma(t)/\sigma_{0fast}$. The time instant $t = 0$ was chosen as the moment when the magnetic field pulse was switched-off. This time instant corresponds to 0.9

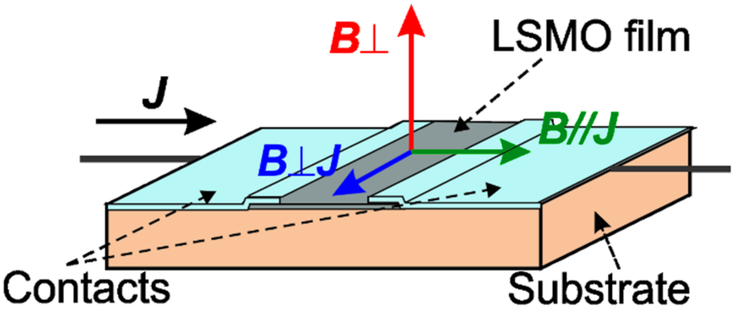

Figure 4.19: Three different directions of B applied in respect to the film plane and bias current J.

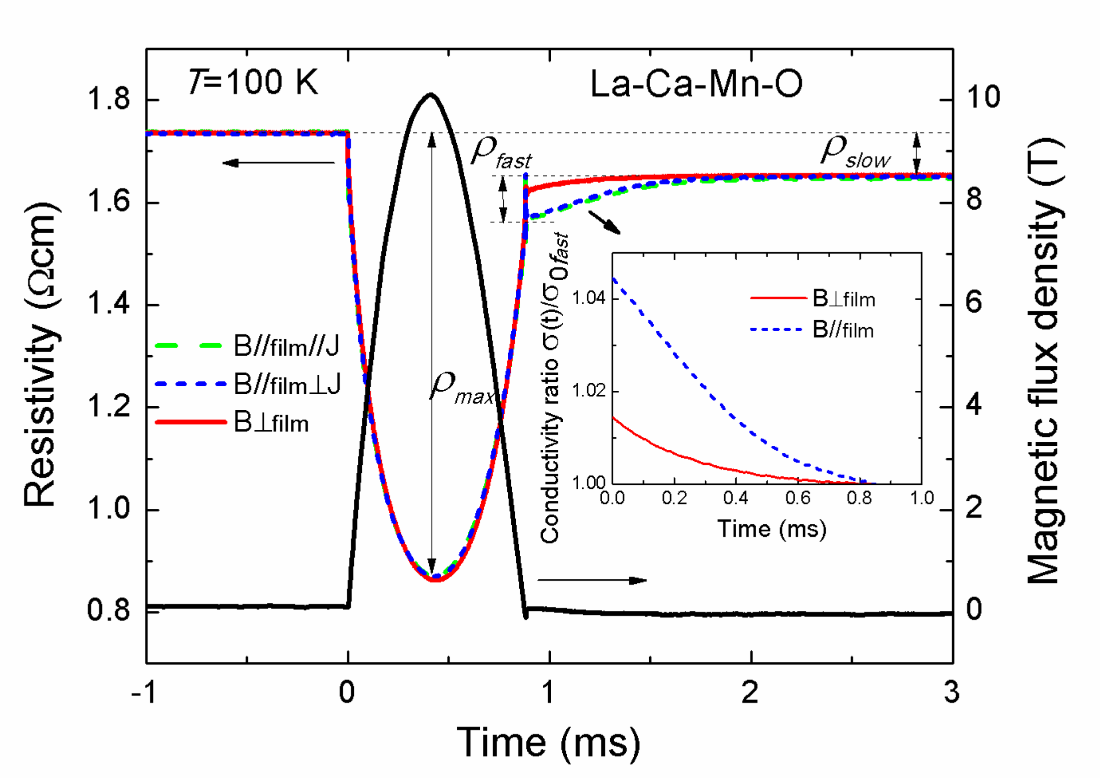

Figure 4.20: Magnetic field pulse (right scale) and resistivity response (left scale) for La-Ca-Mn-O film, when magnetic field is applied in three different directions in respect to film plane and current J. The inset presents corresponding conductivity dynamics ($t = 0$ when B is switched-off) for two B directions.

ms for the resistivity change pulse presented in Fig.4.20 (left scale). It was obtained that the 'fast' resistance relaxation processes are similar for both in-plane magnetic field directions (see Fig.4.20). However, when magnetic field is applied perpendicular to the film plane, the remnant resistivity is much smaller. It has to be noted, that anisotropy effect for 'slow' relaxation component was not observed. This result is important not only from fundamental point of view, but also for the application in magnetic sensing avoiding memory effects. For the development of magnetic field sensors operating at cryogenic temperatures, it is important to determine the conditions under which the remnant resistivity and characteristic time of the relaxation processes can be minimized to ensure sufficient measurement accuracy. The results of resistance (conductance) relaxation, namely, the dependences of remnant resistivity magnitudes and characteristic time constants of these processes on magnetic field magnitude and direction in respect to the film plane as well as influence of film structure and morphology on the mechanisms of relaxation, are presented and discussed below.

It is clearly seen that remnant conductivity amplitude is higher when magnetic field is applied in-plane. By fitting relaxation curves, it is possible to determine the parameter β and hence the predominant relaxation mechanism (magnetic domain propagation or nucleation). Also, one can extract the time $t_{1/2}$ needed to relax half of the film remnant conductivity magnitude. In order to compare times $t_{1/2}$ of relaxation processes for different films and magnetic field directions, we normalized the remnant conductivity $\Delta\sigma_{fast} = \sigma(t) - \sigma_{0fast}$ to its initial value σ_{fast}. Fig.4.21 presents the results for the LSMO and LCMO films ($d = 280$ nm) measured at 100 K temperature (ferromagnetic state). One can see that kinetics of

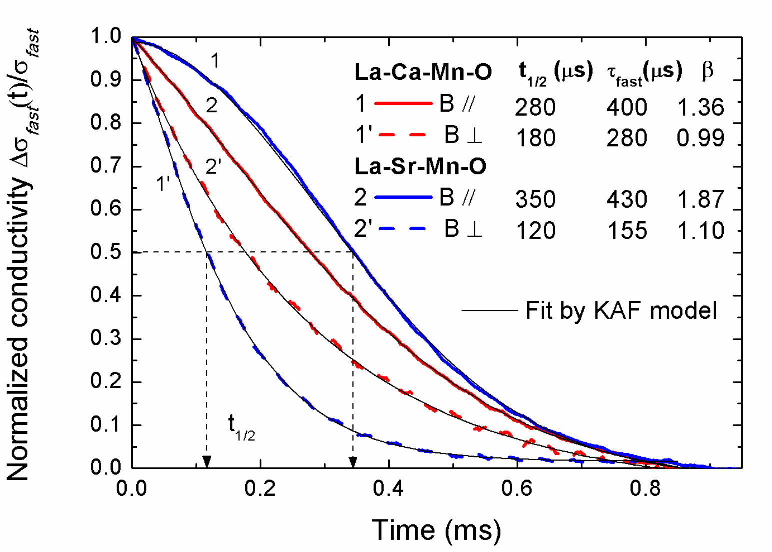

Figure 4.21: Normalized conductivity kinetics for LCMO and LSMO films ($d =$ 280 nm) when magnetic field is applied parallel or perpendicular to film plane. The inset presents half-magnitude times $t_{1/2}$, characteristic time constants τ_{fast} and exponent β values obtained by fitting experimental results to Eq.4.3. $T =$ 100 K; $B = 10$ T.

conductivity $\Delta\sigma_{fast}$ when magnetic field is applied in-plane has more pronounced S-shape and is longer ($t_{1/2} = 350\,\mu s$) for La-Sr-Mn-O films in comparison with the La-Ca-Mn-O films ($t_{1/2} = 280\,\mu s$). The characteristic time constant τ_{fast} and exponent β obtained by fitting the experimental results using Eq.4.3 are 430 µs and 1.87, respectively, for the LSMO films, and 400 µs and 1.36, respectively, for the LCMO films. For the case when magnetic field is applied perpendicular to the film plane, the process is faster if compared with the in-plane cases, however, for this case the process is faster for the LSMO film. The obtained results can be explained as follows. In the ferromagnetic state, the relaxation process is determined mostly by the reorientation of the magnetic domains into their equilibrium state. It is known that for polycrystalline or nano-structured films having disordered grain boundaries and not perfect crystallites with column width < 100 nm as in our case, various defects behave like pinning sites and, at first, some reversed spins or small domains appear in the films and act as nuclei. The β values obtained

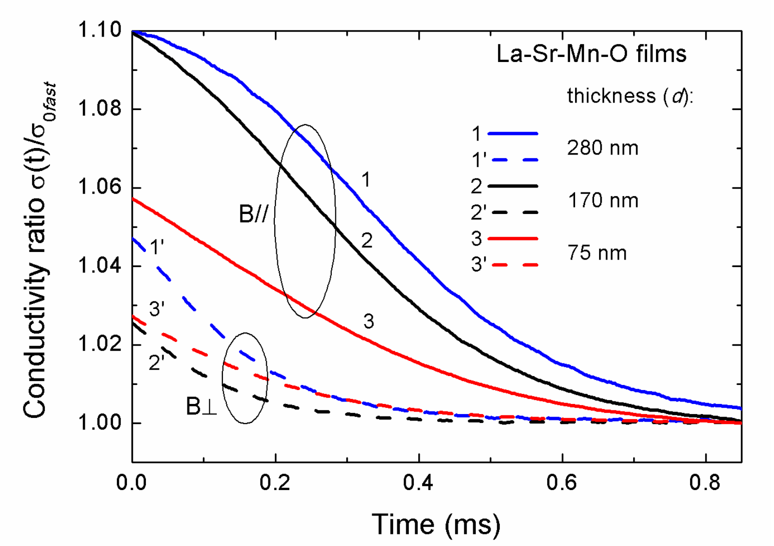

Figure 4.22: Remnant conductivity ratio kinetics of LSMO films having different thickness after removal of magnetic field applied parallel (solid lines) and perpendicular (dashed lines) to film plane. $B = 10$ T; $T = 100$ K.

by fitting experimental curves of our investigated films are presented in the inset of Fig.4.21. The higher β values for La-Sr-Mn-O films (1.87) in comparison with La-Ca-Mn-O films (1.36) for the in-plane magnetic field case ($B//$) indicate that nucleation process is faster in the latter case. Moreover, the crystallites of the nano-structured films are small enough and thus the domain wall propagation is limited. For the case when the film is magnetized perpendicular to the plane ($B\perp$), the faster decrease of remnant magnetization and, as a result, the faster decrease of remnant conductivity upon the removal of external magnetic field can be related to the rotation of magnetization vector towards the in-plane direction which coincides with easy-magnetization axis of our investigated films. It is known that the shape anisotropy of thin non-strained manganite films favours the magnetization to lie in-plane, while for strained epitaxial films it is very dependent on the level of tensile or compressive strain, which originates from the mismatch with the substrate [89]. Therefore, for our investigated nano-structured films the relaxation process is faster for out-of-plane direction: half-magnitude characteristic times $t_{1/2}$ are 120 µs and 180 µs for La-Sr-Mn-O and La-Ca-Mn-O films, respectively. Moreover, the demagnetizing field for out-of-plane magnetized films acts to reduce the domain nucleation field in respect to the in-plane case [90]. As a result, domain nucleation is easier for out-of-plane case and this makes out-of-plane relaxation nucleation dominated ($\beta \gtrsim 1$), while in the process of in-plane relaxation domain wall propagation acts together with the nucleation. The faster out-of-plane relaxation process results in the smaller remnant conductivity magnitude (approx. 3 times) in comparison with the in-plane case (see inset in Fig.4.20).

In order to clear up the influence of film morphology and microstructure on dominant magnetic relaxation mechanism, the relaxation processes in La-Sr-Mn-O films having different thickness were investigated. The Sr-doped films were chosen due to higher remnant amplitudes and more pronounced difference for in-plane and out-of-plane directions (see Fig.4.20). Fig.4.22 shows kinetics of normalized remnant conductivity ratio $\sigma(t)/\sigma_{0fast}$ for films with thickness of 75, 170 and 280 nm. One can see that similar to the LCMO case, the magnitudes of remnant conductivity of the LSMO films where external magnetic field was applied in-plane are also approximately 3 times smaller in comparison to the case where magnetic field was perpendicular to the film plane. Therefore, the anisotropy of the investigated films is mostly determined by the ‘shape’ (demagnetization) effect. It has to be pointed out that the observation of anisotropy effect only for the ‘fast’ relaxation process indicates that the ‘fast’ component is related with the magnetic relaxation phenomena occurring mostly in the crystallites of the nanostructured films.

4.2.4 'Slow' relaxation dynamics – KWW model

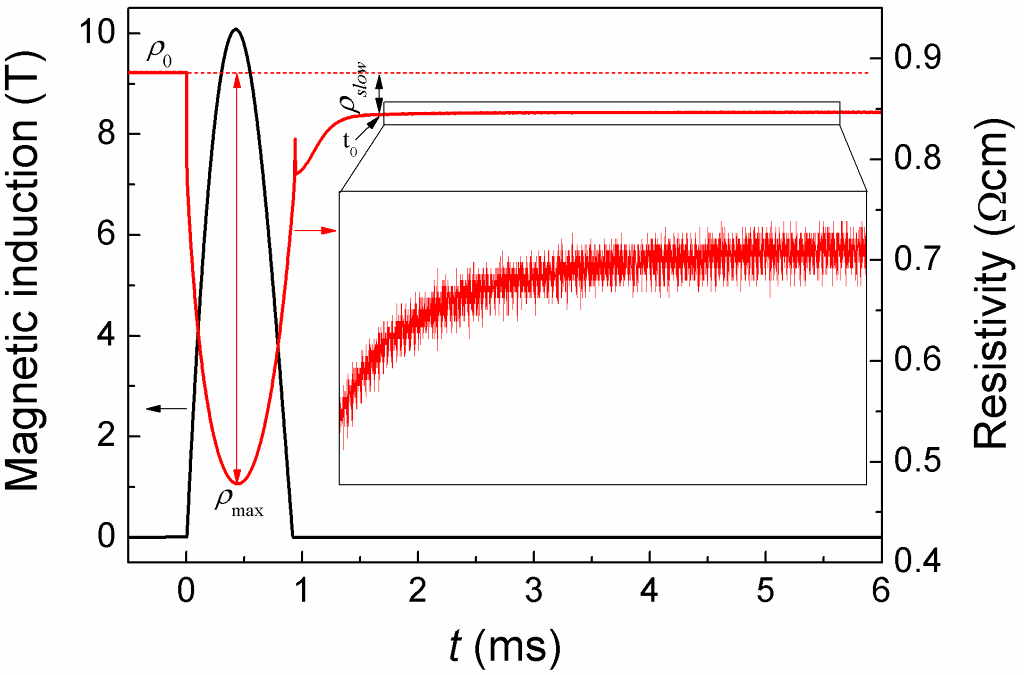

Figure 4.23: Magnetic field pulse (left scale) and resistivity change (right scale) during this pulse. Resistivity change is magnified in the inset picture.

In this section, the 'slow' magnetoresistance relaxation after removal of magnetic field pulse is studied in nanostructured $La_{0.83}Sr_{0.17}MnO_3$ films having grain boundaries with different level of disorder. We investigated the films where resistivity maximum ρ_m differs more than 50 times: 0.8, 1.8, 6.5, 53 Ωcm (Set S3 in Table 3.1). The experimental curves representing results for these films where marked accordingly: F-0.8, F-1.8, F-6.5, F-53. The obtained results are discussed in the frame of Kohlrausch–Williams–Watts model describing spin-glass-like materials. The typical resistivity dynamics for nanostructured manganite films after the application of a magnetic field pulse with an amplitude of 10 T is presented in Fig.4.23 (right scale). The major part of resistivity change follows the magnetic field pulse. In this section we focus on the 'slow' resistivity relaxation (marked as ρ_{slow}) which takes place after the 'fast' relaxation is finished and occurs in ms and longer time scales. The 'slow' conductivity relaxation of the La-Sr-Mn-O films measured while in their ferromagnetic state (T=100 K) is presented in Fig.4.24.

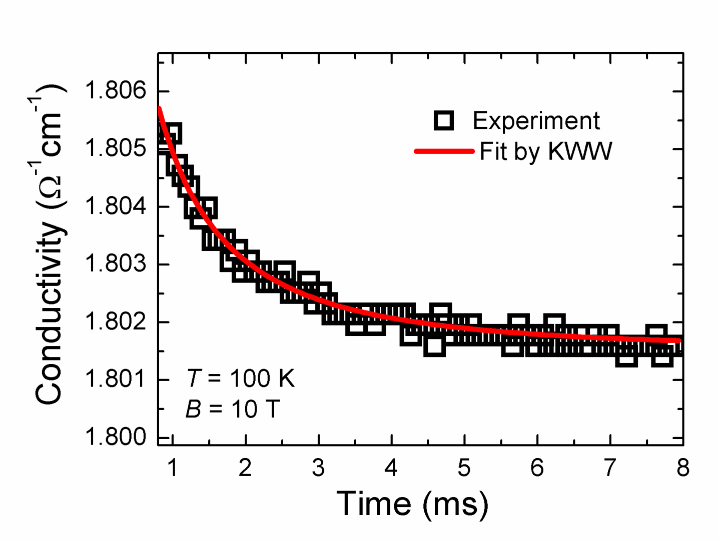

Figure 4.24: Electrical conductivity of the 'slow' relaxation process of the LSMO film from set S1. The squares are the experimental results, the curve represents the results when fitted to the KWW model. $\beta = 0.79$, $\tau_{slow} = 1.08\,\mathrm{ms}$.

The experimental results were fitted using 'stretched' exponential decay [7]:

$$\sigma(t) = \sigma_{0slow} + \sigma_{slow}\exp[-((t-t_0)/\tau_{slow})^{\beta}], \qquad 0 < \beta < 1 \tag{4.5}$$

where t_0 is the time instant at which the 'fast' relaxation process is considered to be finished (3 characteristic time constants and it was chosen to be the same for all investigated films), and the 'slow' relaxation process starts to be analysed, τ_{slow} is the time constant of the 'slow' process, σ_{0slow} and σ_{slow} are the conductivity when the 'slow' relaxation process is finished and remnant conductivity amplitude, respectively. The corresponding resistivity $\rho_{slow} = 1/\sigma_{slow}$ is presented in Fig.4.23.

The normalized time-varying resistivity changes in 'slow' relaxation time range for different samples are presented in Fig.4.25. The resistivity is normalized to the $\rho_{slow} = 1/\sigma_{slow}$ at time instant t_0 for three samples. The starting point of time-axis is chosen $t_0 = 0$. Due to high resistance (about $100\,\mathrm{k\Omega}$) of the sample F-53, the accuracy of its response signal was much lower and filtered signal is presented separately in the inset. One can see that its relaxation takes place in much longer time scales than our measurement range. Fig.4.25 demonstrates that the normalized remnant resistivity is higher for films with higher maximal resistivity, indicating that spin-glass relaxation is more prominent in films with higher

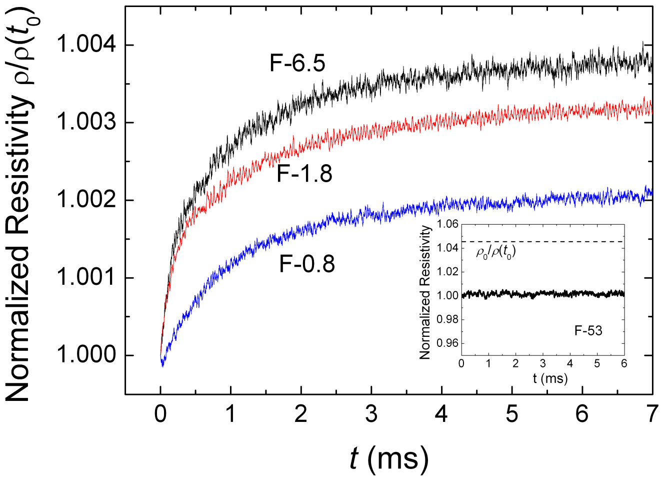

Figure 4.25: Normalised remnant resistivity changes in time of 'slow' relaxation process for films with different ρ_m (6.5 kΩ, 1.8 kΩ, 0.8 kΩ, 53 kΩ (inset)). See Set S3 in Table 3.1.

disorder of their grain boundaries. The dashed line marks the normalized initial resistivity before the action of magnetic field pulse: ρ_{0slow}/ρ_{slow}. The normalized initial resistivity values for the films F-0.8, F-1.8, F-6.5 were 1.043, 1.055 and 1.056, respectively. The similar tendency of increased remnant resistivity change with increased sample disorder was obtained by N. Kozlova *et al.* [48]. They found that slow logarithmic-type resistance relaxation in polycrystalline manganite films ($La_{0.7}Sr_{0.3}MnO_3$) is considerable at low temperatures, while in textured films of the same composition is by one order smaller, and in epitaxial ones is absent (at least two orders smaller). We also didn't observe the magnetoresistance relaxation of investigated epitaxial films of the same thickness (400 nm). M. Sirena *et al.* [10] showed that a large resistivity relaxation and magnetic viscosity ratios are measured when thickness of manganite film is decreased from 300 nm down to 10 nm and explained it with increase of structural disorder of the thinner films due to lattice mismatch.

The results of experiments performed at various temperatures using LSMO samples of set S1 are summarized in Fig.4.26. One can see that the time constant of this process at low temperatures (100 K) is approximately 1.05 ms and decreases with temperature. Due to low measurement accuracy it was not possible to distinguish different behaviour for three investigated films. The obtained β values of

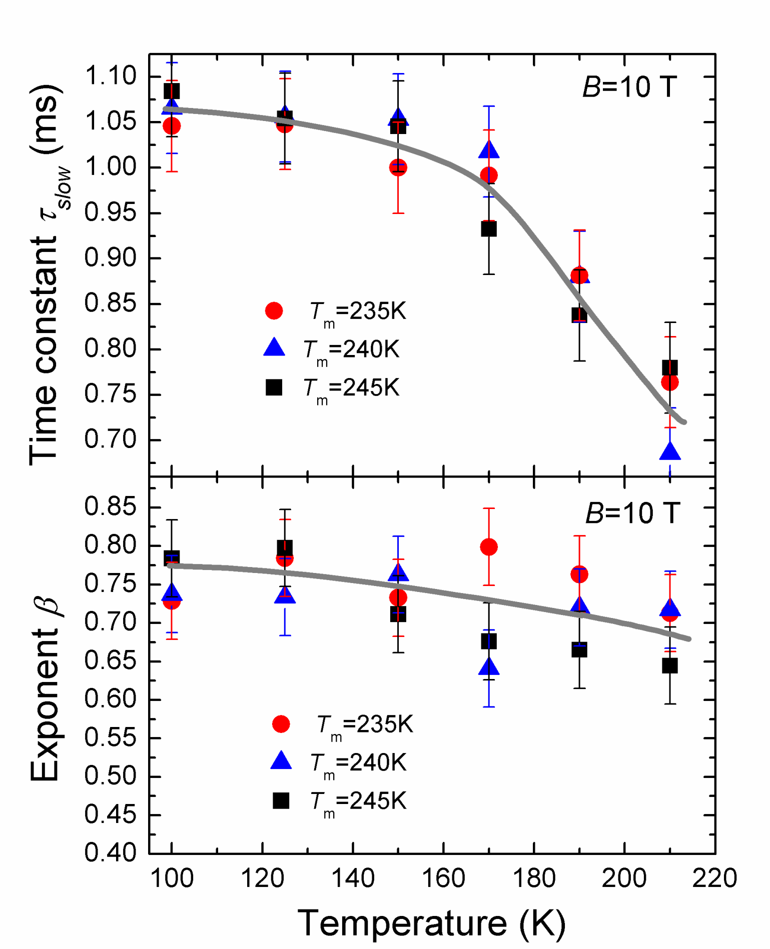

Figure 4.26: Time constant τ_{slow} and exponent β dependences on the temperature of 'slow' conductivity relaxation fitted to the KWW model for three samples with different T_m. See Set S1 in Table 3.1. Curves represent fit to eyes.

the 'stretched' exponent were in the interval $0.65 \leqslant \beta \leqslant 0.8$ and only slightly decrease with increase of temperature (Fig.4.26, lower part). The 'stretched' exponential relaxation, first studied by Kohlrausch in 1847 [91] and later by Williams and Watts in 1970 [71], is often used to fit the experimental curves. The β values obtained through our investigations ($0.65 \leqslant \beta \leqslant 0.8$) indicate that the 'slow' relaxation process in the investigated manganite films takes place through one relaxation channel and is related to short-range interactions in the defected grain boundaries. It was observed (see Fig.4.26) that with rising temperature β is showing tendency to approach the 'magic' value of 0.6 (see [58, 60]) at $T \geqslant T_m$ what indicates that films in paramagnetic state become more homogeneous (considering their transport properties).

4.2.5 Remnant resistivity of 'slow' relaxation

We obtained that the absolute amplitudes of remnant resistivity ρ_{slow} almost does not depend on magnetic field value in the range of 2–10 T for both sets S1 and S3 of LSMO films as seen in figures 4.27a and 4.28a. LCMO films also show similar tendency in Fig.4.29a. It may be explained by saturation of magnetic flux pinned in various defects and dislocations at fields lower than 2 T. It has to be noted that for high magnetic field sensors applications the 'slow' relaxation component relative to maximal resistance change (ρ_{max} or magnetoresistance) is less than 10 % for magnetic fields higher than 8 T and becomes insignificant in high magnetic fields (see figures 4.27b and 4.28b). For sample having smallest clusters and highest resistivity (F-53), this value is smaller (8% at 8 T), probably due to much larger magnetoresistance value. The MR in the magnetic field of 10 T was found to be -73 % for film F-53, -50 % for F-6.5 and -45 % for F-1.8 and F-0.8 films.

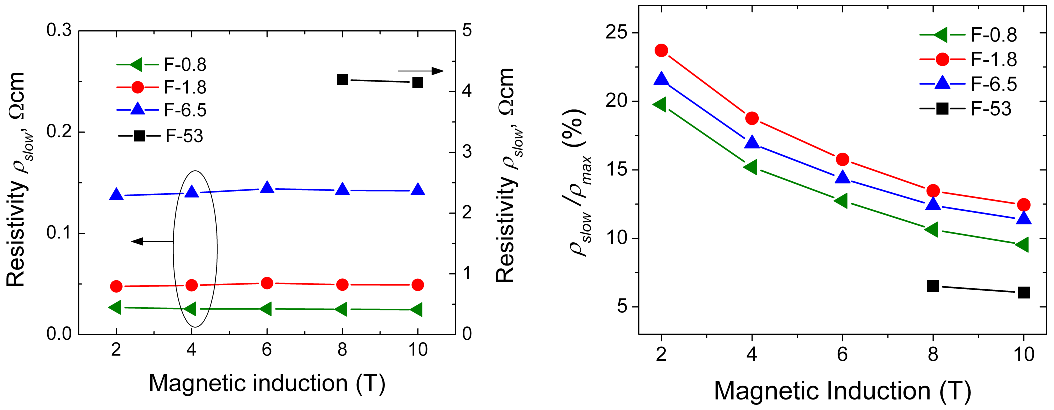

(a) Absolute resistivity.

(b) Relative resistivity.

Figure 4.27: Absolute and relative remnant resistivity dependences on magnetic field of 'slow' relaxation processes for set S3 of LSMO samples with different ρ_m.

For LCMO set C1 the relative remnant resistivity of the 'slow' relaxation process at low temperatures (80 K) amounts to 12–19% at a magnetic flux density of 2 T (see Fig.4.29b) and decreases with increasing of the magnetic field. The results are similar to those of LSMO films. The smallest relative part of the remnant resistivity is obtained for films with smallest dimensions of crystallites (smallest x).

Relative remnant resistivity of 'slow' relaxation process for all investigated films

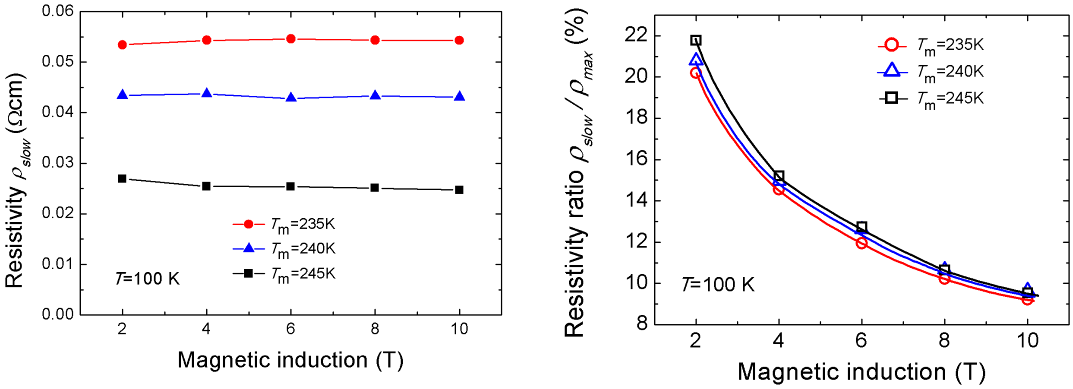

(a) Absolute resistivity.

(b) Relative resistivity.

Figure 4.28: Absolute and relative remnant resistivity dependences on magnetic field of ‘slow’ relaxation processes for set S1 of LSMO samples with different T_m.

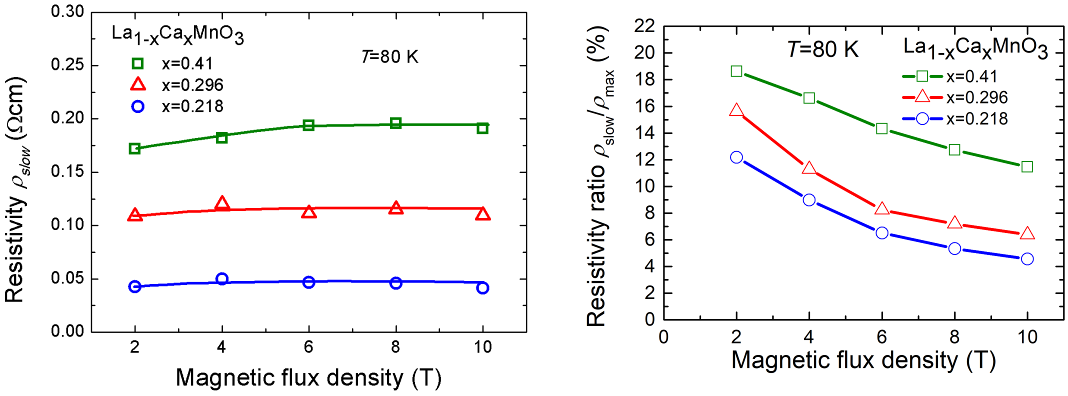

(a) Absolute resistivity.

(b) Relative resistivity.

Figure 4.29: Absolute and relative remnant resistivity dependences on magnetic field of ‘slow’ relaxation processes for set C1 LCMO samples with different x.

drops linearly with rising temperature as seen in Fig.4.30.

It has to be concluded that the ‘fast’ relaxation process is related with magnetic domain nucleation in column like crystallites while ‘slow’ relaxation phenomenon is determined by the process occurring in the disordered grain boundary regions. For measurements of high magnetic fields ($>$ 10 T) with duration longer than milliseconds both magnetic relaxation components play insignificant role.

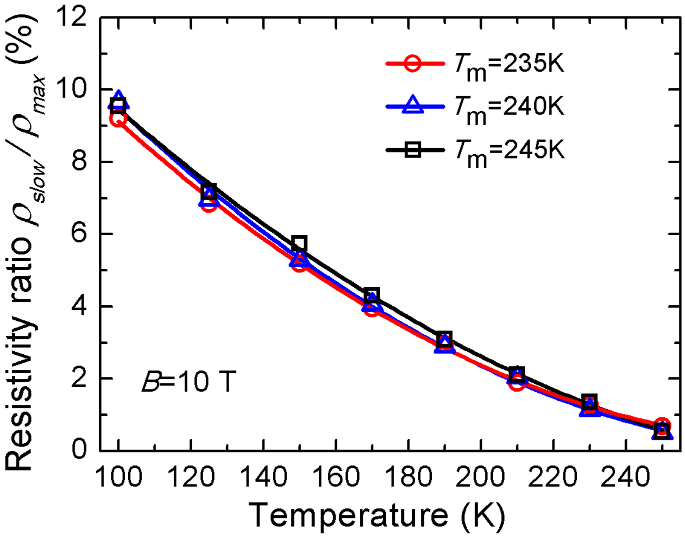

Figure 4.30: Temperature dependency of relative remnant resistivity of 'slow' relaxation process for three LSMO samples with different T_m.

4.3 Ageing of nanostructured manganite films

A significant colossal magnetoresistance (CMR) effect in the investigated nanostructured manganite films makes them perspective materials for the magnetic field sensors. Operation of such sensors is based on the change of the film resistivity depending on the applied magnetic field magnitude. However, both the initial resistance and the sensitivity to magnetic field depend on ambient temperature. This imposes a problem in applications for magnetic field measurements as temperature compensation mechanism is required. In case of pulsed magnetic fields it can be solved by measuring initial resistance of the sensor at zero magnetic field and using calibration curves obtained in advance [4]. For this reason, it is very important to know the exact value of the initial resistance at fixed ambient temperature. It was shown [64] that this resistance of the film exhibits drift in time (ageing phenomenon). This ageing influences the life time of the sensor and requires its frequent recalibration. It was found that in order to minimize these effects a protecting cover have to be used [64]. However, the influence of this cover and thermal treatment of manganite film, which accompanies the processing of this cover, was not investigated. Moreover, the treatment by additional accelerated ageing has to be applied in order to stabilize parameters of the sensors. In this case the stability of the electrical resistance and magnetoresistance over the time plays an important role in the development of these devices. However, it was observed that the structurally imperfect manganite films, such as polycrystalline [64] or very thin epitaxial [65], may undergo dramatic changes of their resistance with time which could limit their technological applicability.

Much work in the past decade has been focused on the investigation of the ageing phenomenon in polycrystalline manganese oxides [66, 68–70] which were used as negative temperature coefficient (NTC) thermistors or common cathode materials for solid oxide fuel cells. Thin nanostructured La-Sr(Ca)-Mn-O manganite films, which are used for the development of the CMR-B-scalar sensors, also can be attributed to this type of materials: randomly oriented nano-crystallites are separated by structurally and magnetically disordered GBs. Therefore, the measurement of ageing kinetics and its analysis can provide an excellent method for the investigation of the ageing mechanisms in these films.

In this section, we focus on the long-term stability of resistivity, magnetoresistance and magnetoresistance anisotropy of thin nanostructured $La_{0.83}Sr_{0.17}MnO_3$ films. For these purposes the accelerated ageing by annealing the uncovered and covered films at different temperatures is applied, and the effects induced by this annealing on ageing peculiarities are investigated and discussed.

4.3.1 The ageing effects of uncovered manganite films

The ageing influence on the resistivity. The accelerated ageing of the manganite samples was performed by their cycled annealing during 1 h at different temperatures T_a (50, 100, 150, 200 and 250 °C) in argon atmosphere. For simplification the samples were numbered according to the annealing temperature (S_{50}–S_{250}). Sample which was kept at room temperature without additional annealing was used as a reference (S_r). For more details see Ageing Measurement Setup in Chapter 3. The stability of resistivity of nanostructured LSMO films over the time was investigated by applying accelerated ageing procedure. The prepared LSMO samples were annealed at different temperatures T_a for a number of cycles (one cycle − 1 h of annealing at a certain temperature). The relative change of resistivity $(\rho_t - \rho_0)/\rho_0$ in time caused by annealing is presented in Fig.4.31. The

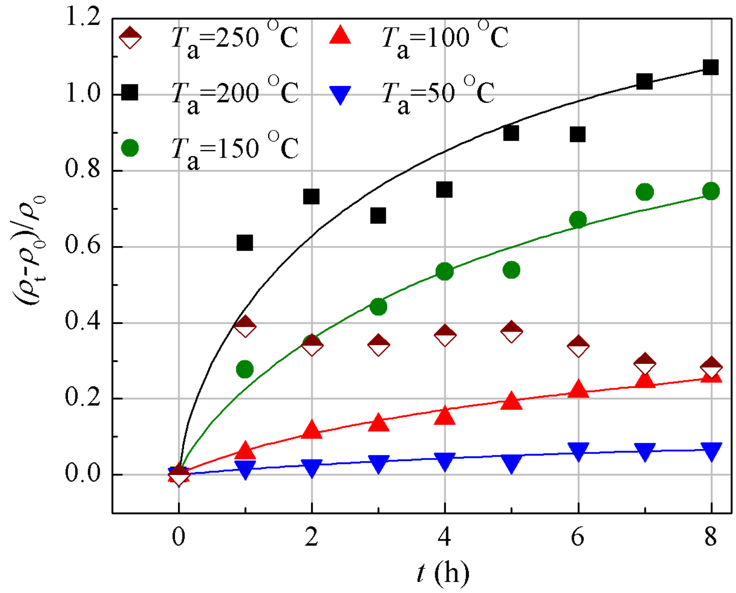

Figure 4.31: The relative resistivity change in time during annealing treatment at various temperatures. Measurements performed at 20 °C. Points – experimental results, curves – fitting to Eq.4.6.

measurements are performed at 293 K temperature. Here ρ_0 is the initial value of the resistivity measured before annealing process, ρ_t – resistivity value after annealing during time period t. One can see that a significant increase of the resistivity is observed during the first hours of annealing, followed by saturation effect. For the sample annealed at 250 °C (S_{250}) the resistivity increase was observed only after the 5 h of thermal treatment. All later cycles only reduced the resistivity. Therefore, the results of the samples annealed at this temperature were not taken into consideration in later analysis. The resistivity change in time during accelerated ageing (annealing at different temperatures) was analysed using the method proposed in [69], where ageing kinetics in ceramic manganite-based negative temperature coefficient thermistors was studied (see Ageing behaviour of manganites in Chapter 2 for more details).

$$\frac{\rho_t-\rho_0}{\rho_0}=\frac{\rho_\infty-\rho_0}{\rho_0}(1-\exp[-(\frac{t}{\tau})^k]) \tag{4.6}$$

For the analysis of results obtained during annealing of the samples at different temperatures, the fitting according to Eq. 4.6 was used. The fitting parameters $(\rho_\infty-\rho_0)/\rho_0$, τ and k are presented in Table 4.3, while the approximation curves

Table 4.3: The parameters of fitting according to Eq.4.6.

Temperature of treatment, °C	$(\rho_\infty - \rho_0)/\rho_0$	τ, h	k
50	0.11	8.4	0.88
100	0.36	6.6	0.83
150	1	5.6	0.74
200	1.32	3.8	0.66

are shown in Fig.4.31. One can see that all parameters depend on the annealing temperature. This indicates that at least few relaxation mechanisms with different characteristic times take place. Moreover, these mechanisms might have different threshold levels for activation energy. It should be noted that mechanisms of degradation processes in topologically disordered systems can be quite different, however, two main groups can be identified among them. The first group explores mechanisms in disordered structures under dispersive transport conditions [68, 70]. Character defects in these structures responsible for deviation from the thermodynamic equilibrium take place in multiple capture-elimination acts of excited carriers before being finally stabilized within degradation tests. The quantitative parameters of elementary capture and elimination acts form the continuous spectra in agreement with structural peculiarities of the disordered solid. The model of hierarchically limited relaxation dynamics [60, 69] is in a basis of the second group of mechanisms. Within this model, each individual relaxation act in disordered solid is possible after previous relaxation events formed favourable conditions for its realization (for example, free-volume space formation). The values of stretched exponent ratio for the first group of mechanisms are between 0.43 and 0.6 [60, 68]. In the case of the second group of mechanisms the stretched exponent ratio shows the tendency to increase up to values in the range of 0.8–0.9 [68, 69]. As it was mentioned in the introduction, in our case the investigated nanostructured LSMO thin films consist of crystallites (column-shaped grains) having almost perfect structure of manganite lattice and inter-granular areas (grain boundaries, GBs), i.e. it is typical topologically-disordered system. The obtained k values (0.66–0.88) and their change with annealing temperature testify that mechanisms of relaxation processes are related with hierarchically limited relaxation dynamics. The possible explanation of these processes will be discussed below. Additionally, the accelerated ageing during longer time period (24 h) was performed on S_{100} samples. The fitting of experimental results obtained on the sample $S_{100(24)}$ annealed at 100 °C during 24 hours showed increased value of the parameter $(\rho_\infty - \rho_0)/\rho_0$, however, the obtained k value was similar (0.8).

Long-term ageing. The influence of annealing temperature on the resistivity change during long-term ageing after the thermal treatment of the samples was studied keeping them at room temperature in a silica gel filled desiccator for almost two years. Fig.4.32 presents the normalized resistivity change of the samples during this period (675 days). The resistivity is normalized to the initial

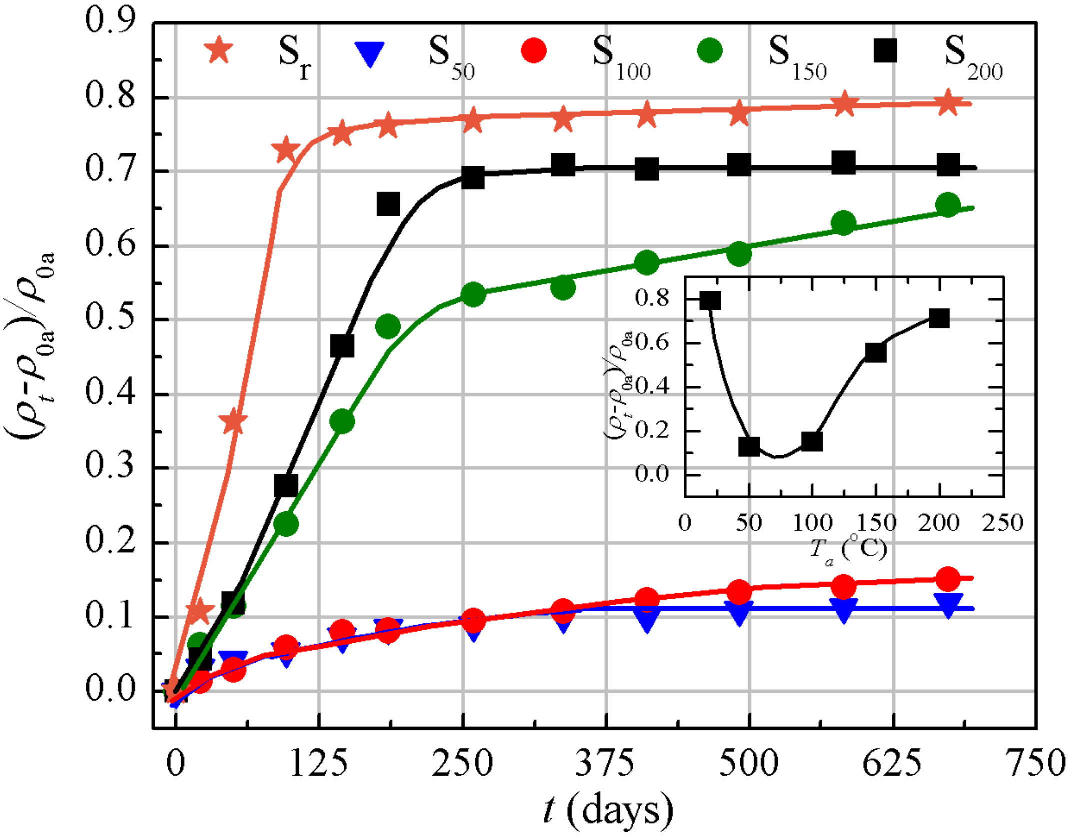

Figure 4.32: The relative resistivity changes during long-term ageing after 8 h of annealing at different temperatures. The resistivity was measured at room temperature (20 °C). The ρ_{0a} is the resistivity of the samples at the beginning of long-term ageing (final value after the accelerated ageing for 8 h). Points – experimental results, curves – fit to eye. Inset presents dependence of relative resistivity at the end of long-term ageing (675 days) on temperature of annealing (the first point corresponds to reference sample S_r stored at room temperature).

value (ρ_{0a}) before the long-term ageing was started (final resistivity values obtained during accelerated ageing). Such relative resistivity change $(\rho_t - \rho_{0a})/\rho_{0a}$ in time characterizes stability of the samples after accelerated ageing. It can be seen that the samples which were annealed at lower temperatures (50 °C and 100 °C) show the best stability: their relative resistivity changes are smaller in comparison with non-annealed (as prepared) reference sample (S_r). However, the samples annealed at higher temperatures (150 °C and 200 °C) showed the higher resistivity change in comparison with the samples annealed at lower temperatures. The inset in Fig.4.32 summarizes the results found during long-term ageing: the minimum resistance changes during almost two years could be obtained by annealing the samples in advance for 8 h at temperatures of 50–100 °C. The results presented in Fig.4.32 indicate that during annealing at temperatures higher than 150 °C additional physical processes can take place. One of the explanations found in literature [92] could be various time-dependent crystallographic structure transformations and other complex electrical conductivity degradation processes in glassy-type grain boundaries which need different energies to be realized. However, our X-ray studies did not show any structural changes after annealing. This may be because the volume of grain boundaries is much smaller than grains and in this case X-ray studies cannot give any result. X-ray diffraction patterns in grazing incidence geometry for $La_{0.83}Sr_{0.17}MnO_3$ film are presented in Chapter 3, Fig.3.1.

The other possible processes could be the following. During annealing of the samples in Ar atmosphere at low enough temperatures ($\lesssim$ 100 °C), only oxygen which is bonded with low binding energies in the disordered grain boundaries could be released. It is known that oxygen deficiencies could cause resistivity increase in manganites because of the effect of decreasing hole carriers [93, 94]. During long-term ageing at room temperature such oxygen may leave the film by diffusion to the surface using the GBs like channels with higher diffusion coefficient [95, 96]. The increase of oxygen diffusion coefficient in GBs in respect to the bulk was observed both in polycrystalline samples with micrometer-sized grains [95] and thin films with nanometer-sized (10–20 nm) grains [96], and it was experimentally evaluated as approximately five orders (at about 700 °C) in the former case and up to six orders in the latter case (at temperature 500 °C).

The higher the annealing temperature, the smaller amount of weekly bonded oxygen is left in the GBs during the treatment and thus the smaller resistivity changes are observed during long-term ageing at room temperature (see inset in Fig.4.32, temperature range 20–100 °C). The higher increase of the resistivity during long-term ageing after annealing of the samples for 8 h at higher temperatures (150–200 °C) can be explained by acting of several mechanisms related with oxygen migration from crystallites to grain boundaries during annealing and by sufficiently higher release of oxygen from grain boundaries at higher annealing temperatures. In this case the oxygen migration from crystallites having better structural quality and thus higher oxygen bonding energies could take place only when annealing temperature is increased. The results presented in the inset of Fig.4.32 indicate that 8 h period is too short to deplete fully the GBs from migrating oxygen, therefore, this process continues during long-term ageing at room temperature through the GBs acting as channels for oxygen diffusion to the film surface. Therefore, the optimal annealing temperature used for accelerated ageing of thin manganite films has to be around 100 °C. It has to be noted that temperature of operation of magnetic field sensors based on LSMO films is up to 40 °C, therefore, the accelerated ageing by annealing at 50 °C is not recommended. Summarizing the results presented in the inset of Fig.4.32, one can see that 8 h of accelerated ageing at 100 °C is not enough for stabilizing the resistivity of the prepared samples. For example, the resistivity of the sample, which was annealed at 100 °C (S_{100}) for 8 h before the long-term storage, has changed approximately 12 % during the first year, while during the second year only 3%. For practical use of the samples as magnetic field sensors this resistivity change during two years is still too high and limits the accuracy of the measurements. The long-term ageing of the sample annealed at 100 °C during 24 h ($S_{100(24)}$) gave better results for the resistivity stability: keeping the sample at room temperature for almost two years the resistivity drift during this period was only 1.5 %. It seems that in this case the most amount of weekly bonded oxygen is released from the GBs during 24 h, therefore, we do not observe significant changes of the film's resistivity during long-term ageing. The measurement of resistivity *vs.* temperature dependencies after annealing the S_{100} samples up to 28 h supports this conclusion: the resistivity significantly changes only after annealing up to 24 h (See Fig.4.33).

Ageing influence on electrical transport mechanisms. In order to clarify the ageing influence on electrical transport mechanisms in the investigated films, the resistivity dependences on temperature were investigated after each cycle of thermal treatment. Several ρ *vs.* T dependences of sample annealed at 100 °C during various time periods are presented in Fig.4.33. One can see that resistivity maximum ρ_m has changed 80% after annealing up to 28 hours, while transition temperature from metal-like to an insulator-like state T_m corresponding to ρ_m remained unchanged. For practical applications of manganite films as active elements of magnetic field sensors operating at room temperatures, the high-temperature region is more important. Therefore, the resistivity *vs.* temperature dependences of the prepared LSMO samples were studied in paramagnetic state at temperatures $T > T_m$. It was obtained that the experimental data can be well described by Mott's variable range hopping (VRH) or small polaron hopping models [32], unfortunately the studied temperature range (265–310 K) was too narrow to allow the distinction between these mechanisms. Our ρ *vs.* T analysis of similar LSMO films having lower T_m (160 K) and thus allowing measurements in a wider temperature range ($T > T_m$) revealed better agreement with the VRH model. These films were prepared at lower deposition temperature (650 °C) and due to higher level of structural disorder their metal-insulator transition temperature T_m is lower [11, 97]. Therefore, VRH model was used to analyse the influence of the ageing process on the electrical properties of the investigated samples. It

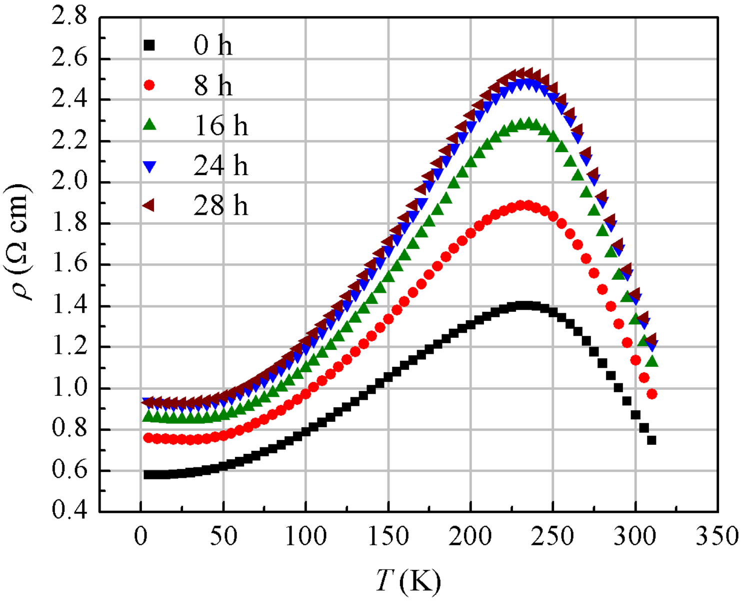

Figure 4.33: The resistivity *vs.* temperature dependences of nanostructured LSMO sample S_{100} annealed at 100 °C for different time periods.

is assumed that using the double exchange mechanism to explain electrical transport in manganites, the e_g electrons are localized by the random spin-dependent potential above the Curie temperature and there is a competition between the potential energy difference and the hopping distance [32, 34]. According to Mott's VRH model the expression for electrical resistivity in three dimensional hopping can be written as [32, 33]

$$\rho = \rho_{res} \exp(T_0/T)^{1/4}, \tag{4.7}$$

where ρ_{res} is residual resistivity and T_0 is the Mott's characteristic temperature, which can be expressed as follows:

$$T_0 = 18/[a^3 k_B N(E_F)], \tag{4.8}$$

where a is the localization length, k_B is the Boltzmann's constant and $N(E_F)$ is the density of states at the Fermi level. The mean hopping distance, $R_h(T)$, and hopping energy, $E_h(T)$, can be expressed at a given temperature T, as [32, 34]:

$$R_h(T) = (3/8)a(T_0/T)^{1/4}, \tag{4.9}$$

$$E_h(T) = (1/4)k_B T^{3/4} T_0^{1/4}. \tag{4.10}$$

The value of the parameter T_0 can be a measure of the strength of the lattice distortion and is inversely proportional to the spatial extent of the localized wave function (a) and density of states $N(E_F)$ (see Eq. 4.8). Following Viret *et al.* [32], the variation of localisation length during the accelerated and the long-term ageing of the films was evaluated. For this purpose the resistivity data of the samples in the temperature range $T > T_m$ were fitted using Mott's VRH model by varying the parameters ρ_{res} and T_0. As an example, the fitted data for sample annealed at 100 °C is shown in Fig.4.34. This experimental data fits well to the Eq. 4.7 at temperatures higher than 280 K. It suggests that the conduction mechanism in the temperature range $T > T_m$ is determined by the Mott's variable range hopping of localized charge carriers. It has to be noted that at lower temperatures ($T < T_m$) the resistivity follows a law describing electron-electron scattering mechanism, however, for the sensors application we focused on the high temperature range. Using the fitted values of T_0, the values of localization length a were calculated

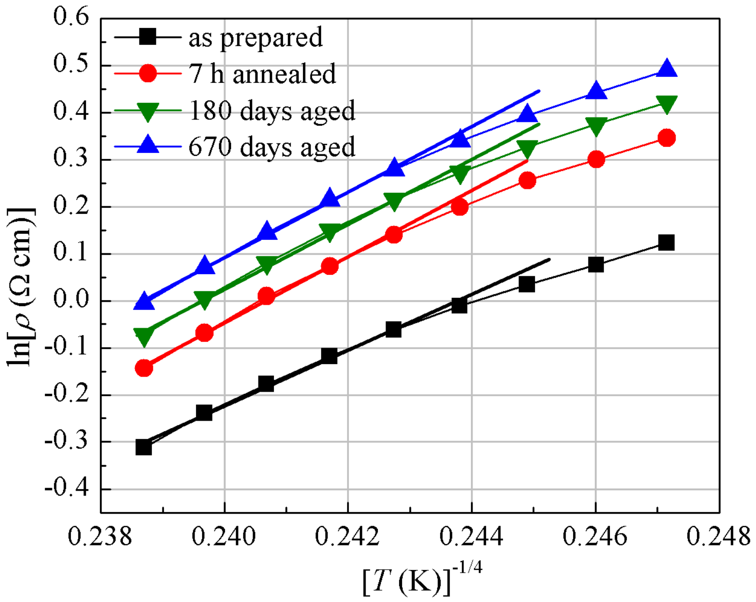

Figure 4.34: Plots of ln ρ versus $T^{-1/4}$ for sample S_{100} annealed at 100 °C.

according to Eq. 4.8. In this case the density of states $N(E_F) = 6 \times 10^{26}$ m^{-3} eV^{-1} was adopted from [32] for investigated manganite films with Sr content $x = 0.17$.

Fig.4.35 presents the changes of localization length values a during annealing (Fig.4.35(a)) and long-term ageing (Fig.4.35(b)) processes for different samples. It has to be noted that the highest change of localization length in the samples is obtained during the first hour of the annealing followed by saturation at longer times. During long-term ageing the changes are small and practically stable value of a is achieved. However, it has to be mentioned that the calculated values of the localization length seem to be incompatible with conventional variable-range hopping, as it was also mentioned in [32], because the localization length has to exceed the Mn-Mn distance and the hopping distance should be several times greater. Such result could be explained by incorrect value of density of states which decreases at $T > T_m$. However, despite of these values not mapping to actual localization lengths, we considered the dependence of the localization length parameter on the ageing temperature and time, and analysed the reasons of its decrease. The main reason of this decrease of the localization length parameter and the resistivity increase of the manganite samples after the ageing process could be mainly related to the creation of oxygen deficiency due to annealing. This result

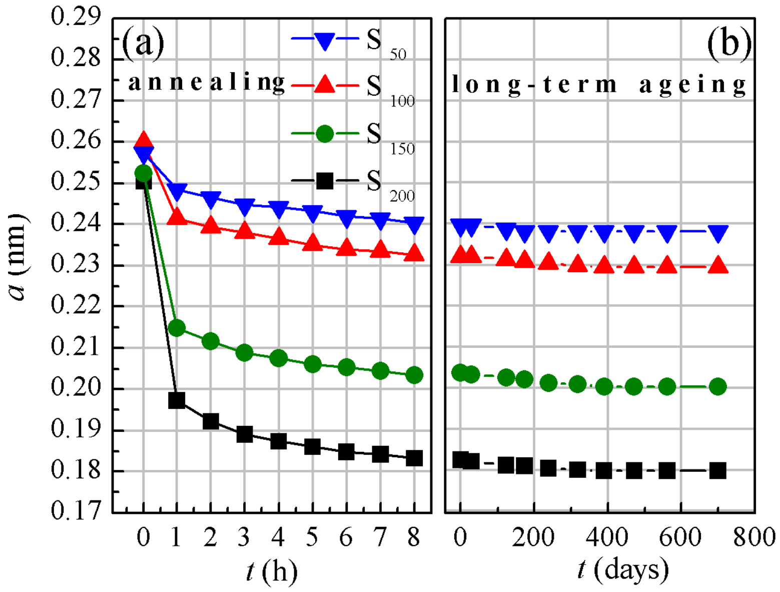

Figure 4.35: The localisation length change in time during annealing (a) and long-term ageing (b) procedures.

would additionally confirm our previous assumptions that oxygen deficiency is responsible for resistivity increase during annealing and long-term ageing.

Ageing influence on the magnetoresitance. The accelerated ageing influence on the magnetoresistance of the samples was investigated in low and high magnetic field ranges. Figure 4.36 shows the magnetoresistance *vs.* magnetic flux density dependences in the low field range of the sample S_{100} at 80 K (a) and 290 K (b) temperatures after different times of annealing. The MR measurements were performed by applying magnetic field parallel and perpendicular to the film plane. Very small MR values in the range of 0–0.3 T when magnetic field is perpendicular to the film plane (Fig.4.36a) are related to the demagnetization effect (‘shape’ effect) which is observed in thin magnetic films. At higher magnetic fields the MR change is more abrupt. It can be clearly seen that accelerated ageing makes influence on MR dependence *vs.* magnetic field, especially at low temperatures when magnetic field is perpendicular to the surface of the film. For the sample which was annealed for 16 hours in comparison to as-prepared sample, the demagnetization field is more than 2 times smaller and MR values at the same magnetic field are higher. When magnetic field is parallel to the plane, the coercive field

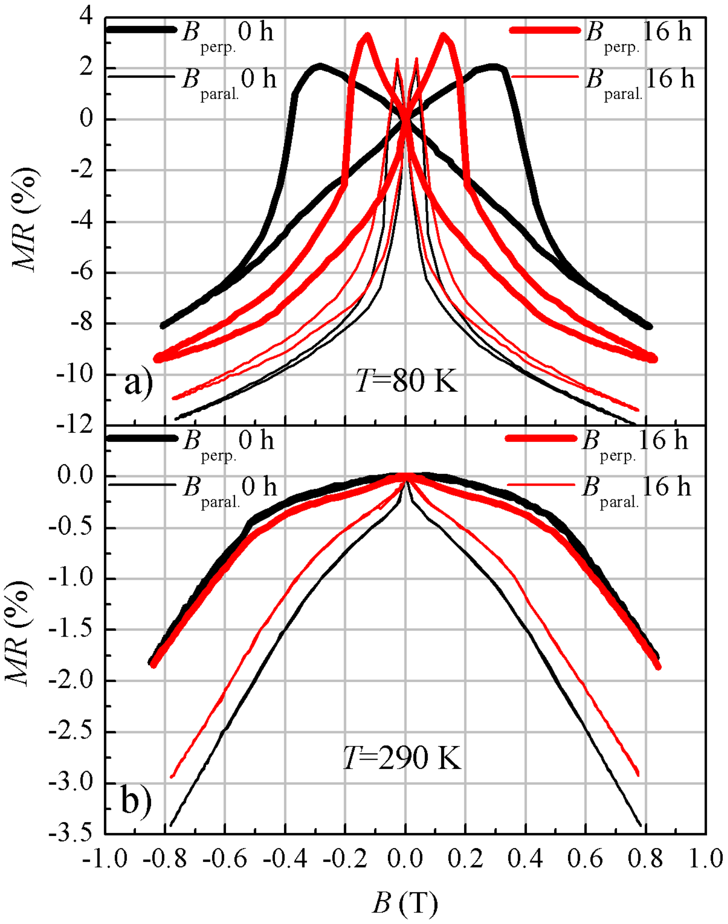

Figure 4.36: The magnetoresistance *vs.* magnetic flux density dependences of the sample S_{100} at 80 K (a) and 290 K (b) temperatures after different annealing times.

value after annealing remains the same, but the film has lower magnetoresistance. Therefore, the magnetoresistance anisotropy (difference of values in parallel and perpendicular to the plane magnetic fields) is decreased. The similar effects are observed at higher temperatures (Fig.4.36b). Such behaviour of magnetoresistance can be explained by weakening of magnetic coupling between the grains after annealing. It should be noted that the grains having perfect magnetic order and grain boundaries with reduced magnetization cannot be considered as entirely independent. The lattice defects (oxygen vacancies) and deviations from magnetic order can be coupled rather strongly and be interdependent [98]. Due to loss of oxygen and decrease of localization length the long range interaction of the film in its plane becomes weaker and so called 'shape' effect (demagnetization) no longer dominates in the MR vs. B dependence. The similar changes in low magnetic fields were observed for films annealed at different temperatures. These results show the possibility to lower anisotropy of magnetic field sensor's response at low magnetic fields by applying accelerated ageing procedure. Fig.4.37 shows magnetoresistance vs. magnetic induction measured at 10 °C, 20 °C, 30 °C and 40 °C before and after annealing during different time period (7, 16, 24 h) at 100 °C. Change of MR vs. annealing time at magnetic induction of 2.3 T is shown in the inset of Fig.4.37. It can be seen that during annealing the magnitude of negative MR decreases insignificantly.

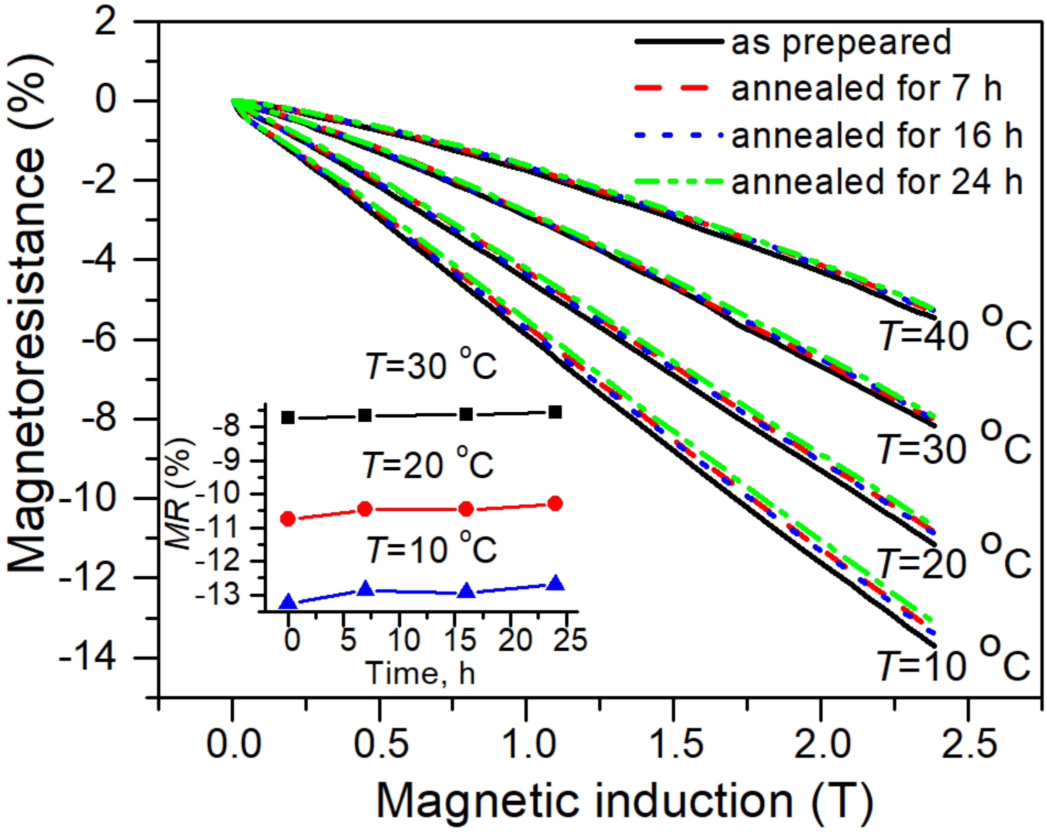

Figure 4.37: Magnetoresistance vs. magnetic induction of the sample S_{100} before and after annealing during different time (7, 16, 24 h) at 100 °C measured at different temperatures. Inset shows changing of MR (at magnetic induction 2.3 T) vs. time of annealing.

The further long-term ageing tests of the magnetoresistance showed that all samples exhibit sufficiently small (less than 0.5 % in amplitude at 2 T) MR change during the total long-term ageing process. Such results could be explained taking into account that the MR of polycrystalline manganite films could be analysed considering contributions of both crystallites and grain boundaries [3]. In general, at temperatures close to Curie temperature, the magnetoresistance of crystallites having perfect structure is supposed to be higher in comparison with grain boundaries having reduced magnetic order. In order to induce magnetization of such disordered material we need to apply very high magnetic fields. Assuming that the ageing process has more influence on grain boundary material due to oxygen deficiency, we can conclude that this is the main reason why the ageing has insignificant influence on the total magnetoresistance of the films at 2 T. The similar results were obtained at high pulsed magnetic fields up to 20 T (see Fig.4.38): the ageing influence on MR values was insignificant (< 2 %). Therefore, despite the changes of grain boundary resistance during annealing and long-term ageing, the total magnetoresistance change is very small. Similar tendencies were observed during the investigation of the ageing influence to resistance relaxation upon removal of magnetic field. As seen in figure 4.39 the normalized remnant resistivity amplitude of 'fast' relaxation is virtually the same in the range of B = 2–10 T for control sample and other 2 samples annealed for different time periods. To sum up, the resistivity increases during ageing process, but the ratio ρ_B/ρ_0 for normalized remnant resistivity as well as the MR remains almost unchanged. The obtained results of relaxation and MR change (or lack of thereof) during accelerated ageing are important for the development of magnetic field sensors which

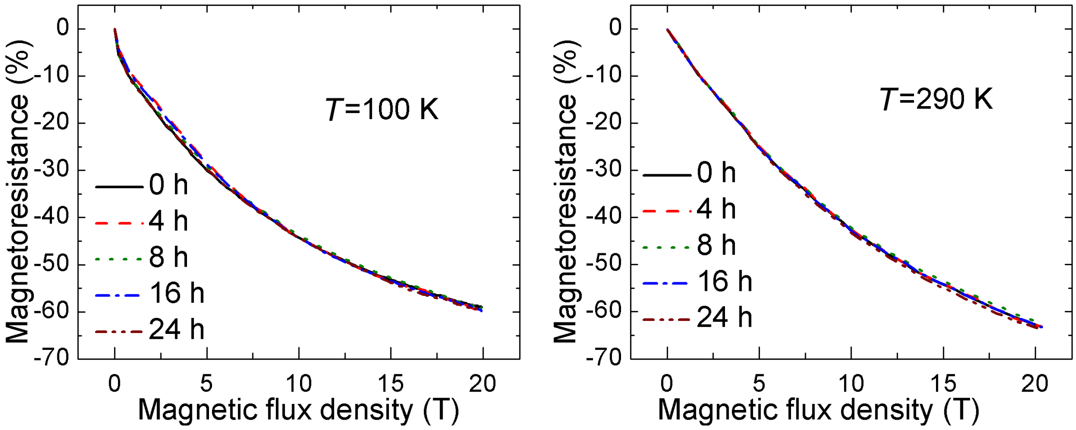

Figure 4.38: Magnetoresistance change of samples in strong magnetic field measured at 100 K and 290 K temperatures during accelerated ageing.

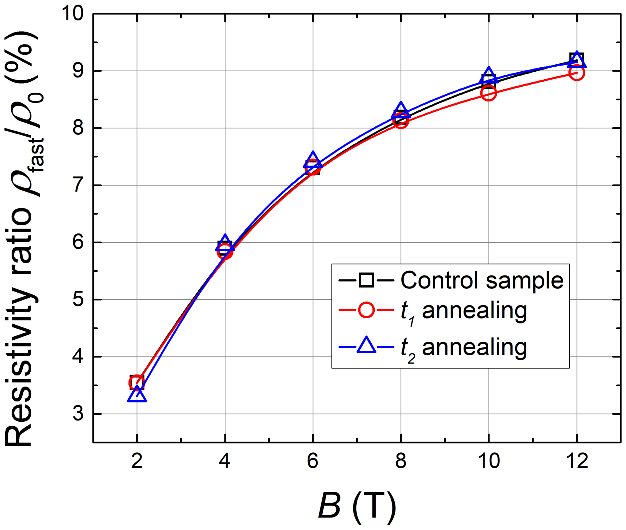

Figure 4.39: Normalized remnant resistivity amplitude *vs.* magnetic flux density for LSMO samples with different annealing durations. $t_1 = 1$ h, $t_2 = 2$ h.

operate at room temperatures and high magnetic fields. Despite the large changes of zero-field resistance during ageing, the insignificant change of magnetoresistance enables to ensure the stability of magnetic field sensors' measurement accuracy during time period of several years.

4.3.2 Influence of a hot-melt adhesive coating on manganite sample ageing

Applications of the manganite films as magnetic field sensors require basic protection of the active surface from the environment. Coating of the samples with chemically inert polymers is one of the possible ways and it was applied as shown in Chapter 3, Fig.3.12. Figure 4.40 presents relative resistance change of coated and uncoated samples with conventional hot melt adhesive (polyethylene). At first both uncoated samples were annealed for 20 hours at 100 °C. Then, one of them was covered with the adhesive and annealing was continued. Resistance measurements performed at 20 °C show a rapid drop followed by a new saturation value after another 20 hours. The uncoated sample reached maximum resistance sooner, just after 38 h. This suggests that the adhesive is not sufficiently inert and reacts

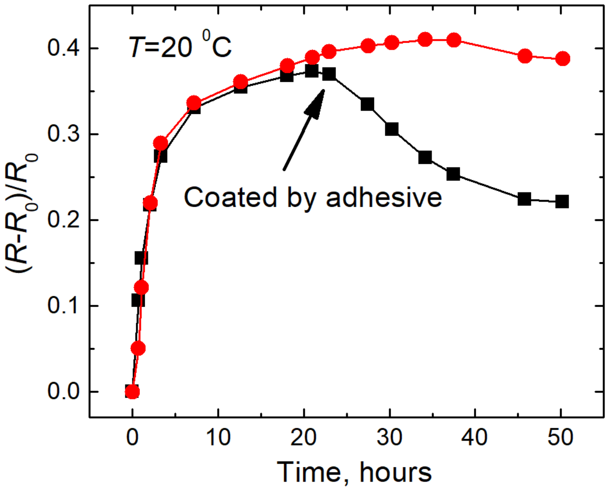

Figure 4.40: Relative resistance change of the samples annealed at 100 °C. One of the samples (black squares) was coated with hot melt adhesive after 20 hours and annealing was continued. The other one was not coated throughout the treatment (red circles). Resistance was measured at 20 °C.

with the manganite film. In the next experiment illustrated by figure 4.41 the samples were coated before the annealing step and its relative resistivity change was compared to uncoated control. The main differences in coated *vs.* uncoated samples is that the relative resistance change is much lower for uncoated samples and it requires less annealing time to reach the steady state. Such decrease of resistance drift can be explained by simultaneous action of the ageing process and reaction to the coating material, since the former effect causes increase of resistance and the latter one – its decrease (Fig.4.40). As in the case of uncoated samples, the resistance of the coated samples reached different saturation values depending on the annealing temperature. Fig.4.42 presents the results of relative resistance change in time when the annealing process was stopped (after ~50 h of annealing). The resistance drift of the sample, which was covered but not annealed, is also presented in this figure. The samples were kept at room temperature for seven months (~5040 hours) while the resistance was measured at 20 °C. It can be seen that the most stable state was reached after annealing at 100 °C for about 50 hours. After such thermal treatment, the resistance changes only about 1.5 % per year. On the other hand, the resistance of the samples treated at lower or higher temperatures continued to increase or decrease, respectively during approximately four months. At the same time, as was mentioned earlier,

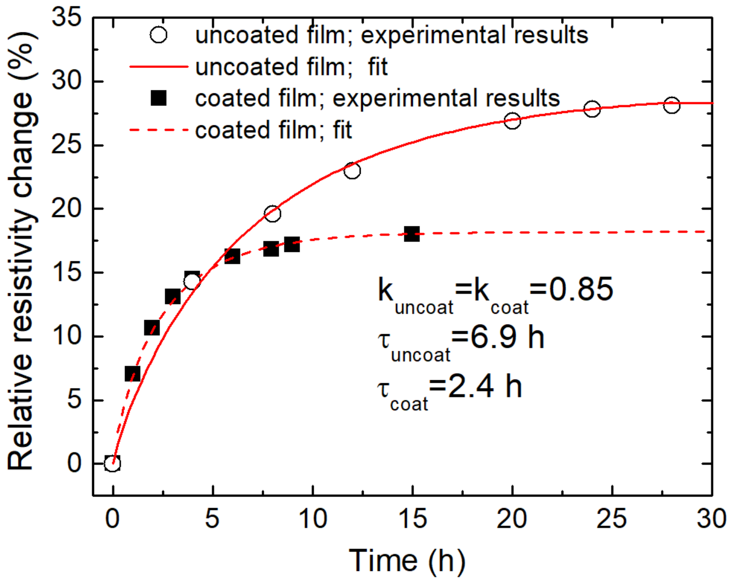

Figure 4.41: Relative resistivity change measured at temperature 293 K during accelerated ageing process of LSMO coated and uncoated samples (T_a = 100 °C). Points – experimental results, curves – fits with Eq. 4.7.

the resistance drift of untreated sample takes place up to two years.

Coating of the sensor surface is used to prevent the surface interaction with environment; however, it cannot prevent the intrinsic ageing processes. Various coatings have been used traditionally for the neutralization of the semiconductor surface like SiO_2 or Si_3N_4. However, it was shown in [99, 100] that coating of the manganites with siliceous materials sufficiently changes their magnetic properties. Various coatings used in electronics (epoxy resins, varnish and others materials) can be adapted for coating of the manganite samples. In previous study [64] it was already shown that epoxy adhesives caused unacceptable increase of resistance of the LSMO films. Polyamides and polyethylene are often used for coating the surface of the MEMS devices [101]. From the results obtained in this section, we can see that the polyethylene hot-melt adhesive is a good candidate according to all parameters. The solidification point of this adhesive is about 150 °C, it has high electrical resistance and good adhesion.

Results presented in Fig.4.40 indicate that during the annealing of coated layers, there is a drop of resistance. Perhaps it is caused by the penetration of the atoms of adhesive into the GBs regions of the film. EDS analysis of the surface

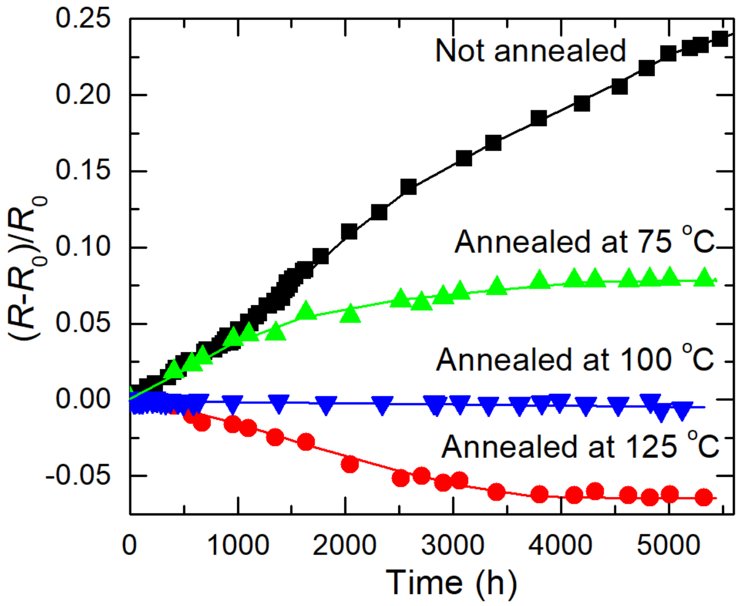

Figure 4.42: Relative resistance drift of coated sample, which was not thermally treated, and coated samples after thermal treatment at different temperature during 48 hours. All measurements were done at 20 °C.

chemical composition of the samples coated by adhesives was performed. For this purpose the samples were covered by adhesive, heated at 100 °C during 7 h, then the adhesive was removed and EDS analysis was performed. As a result, only a small increase of carbon intensity above the background signal in the EDS signal was obtained. Such result can be explained as follows. It can be assumed that during coverage of the surface by adhesive some mutual molecular interactions with the surface of the manganite film take place. Therefore, after the removal of hot-melt adhesive due to its high adhesion properties small amount of it can be left on the surface of the film and, as a result, carbon can be observed by the EDS. However, such small amount of carbon cannot explain the significant resistance decrease during heating of the film covered by hot-melt adhesive (see Fig.4.40). One of the possible reasons of resistance change can be the oxygen release from the adhesive and its introduction into the film, because the hot melt adhesive contains polyethylene as a base and some additive co-polymer which contains carbonyl or hydroxyl groups. In such case, the enrichment with oxygen can cause the decrease of film resistance. However, additional investigations have to be performed to clarify these mechanisms.

The obtained results show that suggested method of coating and annealing treatment at 100 °C allows to accelerate the ageing process and to significantly reduce the drift of the sensor characteristics. As a result, magnetic field sensors which keep their electrical resistance and sensitivity to magnetic field stable for several years can be produced.

Chapter 5

General Conclusions

1. Magnetoresistance of nanostructured manganite films strongly depends on the morphology and chemical composition of the films and can be analysed using modified Mott's hopping model taking into account contributions of both crystallites and grain boundaries. Its dependence on magnetic flux density scales with the sum of corresponding Brillouin functions $\mathcal{B}(\chi_C) + \mathcal{B}(\chi_{GB})$ in ferromagnetic state and with the sum of $\mathcal{B}^2$ in paramagnetic state.

2. Resistance relaxation in nanostructured manganite films after magnetic field is switched off takes place in two different time scales: fast ($\sim$ 100 µs), and slow ($\geqslant$ 1 ms). The characteristic time constants and relative parts of the remnant resistivity of the 'slow' and 'fast' components decrease rapidly with an increase of temperature and are negligible in the paramagnetic state of the films.

   2.1 The 'fast' magnetic relaxation process could be analysed using the Kolmogorov-Avrami-Fatuzzo model describing its kinetics by a compressed exponential expression. The obtained exponent parameter β in the range of 1.3–1.5 indicates that the predominant mechanism is nucleation and reorientation of magnetic domains into their equilibrium state. This relaxation depends on microstructure of the films and is several times faster when magnetic field is applied perpendicular to the film plane in comparison with in-plane case due to 'shape' (or demagnetization) effect of the films.

2.2 The remnant resistivity of the 'fast' relaxation process is proportional to the magnetoresistance of the films and non-linearly increases with magnetic field. The relative part of the 'fast' component in respect to the whole resistance change during magnetic field pulse could be decreased by using films with larger crystallites. For the measurement of high-pulsed magnetic fields with durations longer than several milliseconds, this component plays an insignificant role.

2.3 The 'slow' magnetic relaxation process could be analysed using the Kohlrausch-Williams-Watts model considering the interaction of the magnetic moments in disordered grain boundaries having spin-glass properties. Its kinetics is well described by the stretched exponent with exponent parameter β values in the range of 0.6–0.8.

2.4 The absolute value of the remnant resistivity of the 'slow' component is proportional to the resistivity of the film and is almost independent on magnetic field magnitude. Thus the relative part of it decreases with an increase of the magnetic field and at high fields (60 T) is less than 5 % at cryogenic temperatures.

3. Nanostructured $La_{1-x}Sr_xMnO_3$ films having a higher sensitivity at room temperature in comparison with $La_{1-x}Ca_xMnO_3$ films should be favoured for the application at appropriate high temperatures, while the $La_{1-x}Ca_xMnO_3$ films which at cryogenic temperatures exhibit higher magnetoresistance values and smaller relative remnant resistivity than $La_{1-x}Sr_xMnO_3$ ones are preferred for the magnetic field sensors operating at low temperatures.

4. Treatment of nanostructured manganite films by annealing them in an argon atmosphere at temperatures of 100–200 °C accelerates their ageing process and stabilizes their resistance and magnetoresistance.

4.1 The ageing kinetics leads to a significant increase of the film resistivity which can be explained by the model of hierarchically limited relaxation dynamics with stretched exponential dependence typical for topologically-disordered systems, and is related with oxygen depletion and its diffusion in the grain boundaries of the nanostructured manganite films.

4.2 The accelerated ageing process decreases the demagnetization field of manganite films thus decreasing magnetoresistance anisotropy at low (< 1 T) magnetic fields. In high magnetic fields (> 1 T) the ageing processes have insignificant (< 2 %) influence on the magnetoresistance.

4.3 The stability of electrical parameters of nanostructured manganite films (change of resistivity and magnetoresistance < 2% during two years) could be obtained by the accelerated ageing of the samples annealing them for approximately 24–28 h at temperature close to 100 °C. The annealing of the manganite samples coated by a hot-melt adhesive increases the accelerated ageing process by almost three times and stabilizes their resistivity and magnetoresistance.

Bibliography

[1] C. Israel, M. J. Calderón, and N. D. Mathur, “The current spin on manganites,” *Materials Today*, vol. 10, no. 10, pp. 24–32, 2007.

[2] T. Stankevič, L. Medišauskas, V. Stankevič, S. Balevičius, N. Žurauskienė, O. Liebfried, and M. Schneider, “Pulsed magnetic field measurement system based on colossal magnetoresistance-B-scalar sensors for railgun investigation,” *Review of Scientific Instruments*, vol. 85, no. 4, p. 044704, 2014.

[3] S. Balevičius, N. Žurauskienė, V. Stankevič, S. Keršulis, V. Plaušinaitienė, A. Abrutis, S. Zherlitsyn, T. Herrmannsdörfer, J. Wosnitza, and F. Wolff-Fabris, “Nanostructured thin manganite films in megagauss magnetic field,” *Applied Physics Letters*, vol. 101, no. 9, p. 092407, 2012.

[4] M. Schneider, O. Liebfried, V. Stankevic, S. Balevicius, and N. Zurauskiene, “Magnetic diffusion in railguns: Measurements using CMR-based sensors,” *IEEE Transactions on Magnetics*, vol. 45, no. 1, pp. 430–435, 2009.

[5] T. L. Haran, R. B. Hoffman, and S. E. Lane, “Diagnostic capabilities for electromagnetic railguns,” *IEEE Transactions on Plasma Science*, vol. 41, no. 5, pp. 1526–1532, 2013.

[6] S. Balevičius, N. Žurauskienė, V. Stankevič, T. Herrmannsdörfer, S. Zherlitsyn, Y. Skourski, F. Wolff-Fabris, and J. Wosnitza, “CMR-B-scalar sensor application for high magnetic field measurement in nondestructive pulsed magnets,” *IEEE Transactions on Magnetics*, vol. 49, no. 11, pp. 5480–5484, 2013.

[7] H. Xi, K.-Z. Gao, J. Ouyang, Y. Shi, and Y. Yang, “Slow magnetization relaxation and reversal in magnetic thin films,” *Journal of Physics: Condensed Matter*, vol. 20, no. 29, p. 295220, 2008.

[8] M. Dominiczak, A. Ruyter, P. Limelette, I. Monot-Laffez, F. Giovannelli, M. D. Rossell, and G. Van Tendeloo, “Relaxation phenomena at the metal-to-insulator transition in La 0.8 Sr 0.2 MnO 3 single crystals,” *Solid State*

Communications, vol. 148, no. 7, pp. 340–344, 2008.

[9] S. Balevičius, B. Vengalis, F. Anisimovas, J. Novickij, R. Tolutis, O. Kiprianovič, V. Pyragas, and E. Tornau, "Dynamics of resistivity response of La 0.67 Ca 0.33 MnO 3 films in pulsed high magnetic fields," *Journal of Magnetism and Magnetic Materials*, vol. 211, no. 1, pp. 243–247, 2000.

[10] M. Sirena, L. Steren, and J. Guimpel, "Magnetic relaxation in bulk and film manganite compounds," *Physical Review B*, vol. 64, no. 10, p. 104409, 2001.

[11] N. Zurauskiene, S. Balevicius, V. Stankevic, S. Kersulis, M. Schneider, O. Liebfried, V. Plausinaitiene, and A. Abrutis, "B-scalar sensor using CMR effect in thin polycrystalline manganite films," *IEEE Transactions on Plasma Science*, vol. 39, no. 1, pp. 411–416, 2011.

[12] A. N. Kolmogorov, "On the statistical theory of the crystallization of metals," *Bull. Acad. Sci. USSR, Math. Ser*, vol. 1, pp. 355–359, 1937.

[13] J. Coey and M. Viret, "Mixed-valence manganites," *Advances in Physics*, vol. 48, no. 2, pp. 167–293, 1999.

[14] J. F. Mitchell, D. Argyriou, C. Potter, D. Hinks, J. Jorgensen, and S. Bader, "Structural phase diagram of La 1-x Sr x MnO 3+δ: Relationship to magnetic and transport properties," *Physical Review B*, vol. 54, no. 9, p. 6172, 1996.

[15] K. Dörr, "Ferromagnetic manganites: spin-polarized conduction versus competing interactions," *Journal of Physics D: Applied Physics*, vol. 39, no. 7, p. R125, 2006.

[16] Y. Okimoto, T. Katsufuji, T. Ishikawa, A. Urushibara, T. Arima, and Y. Tokura, "Anomalous Variation of Optical Spectra with Spin Polarization in Double-Exchange Ferromagnet: La 1-x Sr x MnO 3," *Physical Review Letters*, vol. 75, no. 1, p. 109, 1995.

[17] E. Dagotto, T. Hotta, and A. Moreo, "Colossal magnetoresistant materials: the key role of phase separation," *Physics reports*, vol. 344, no. 1, pp. 1–153, 2001.

[18] P. Schiffer, A. Ramirez, W. Bao, and S. Cheong, "Low temperature magnetoresistance and the magnetic phase diagram of La 1-x Ca x MnO 3," *Physical Review Letters*, vol. 75, no. 18, p. 3336, 1995.

[19] Y. Moritomo, T. Akimoto, A. Nakamura, K. Ohoyama, and M. Ohashi, "Antiferromagnetic metallic state in the heavily doped region of perovskite manganites," *Physical Review B*, vol. 58, no. 9, p. 5544, 1998.

[20] Y. Tomioka, A. Asamitsu, H. Kuwahara, Y. Moritomo, and Y. Tokura, "Magnetic-field-induced metal-insulator phenomena in Pr 1-x Ca x Mn O 3 with controlled charge-ordering instability," *Physical Review B*, vol. 53, no. 4, p. R1689, 1996.

[21] H. Hwang, S. Cheong, P. Radaelli, M. Marezio, and B. Batlogg, "Lattice effects on the magnetoresistance in doped LaMnO 3," *Physical review letters*, vol. 75, no. 5, p. 914, 1995.

[22] C. Zener, "Interaction between the d shells in the transition metals," *Physical Review*, vol. 81, no. 3, p. 440, 1951.

[23] C. Zener, "Interaction between the d-shells in the transition metals. II. Ferromagnetic compounds of manganese with perovskite structure," *Physical Review*, vol. 82, no. 3, p. 403, 1951.

[24] A. Haghiri-Gosnet and J. Renard, "CMR manganites: physics, thin films and devices," *Journal of Physics D: Applied Physics*, vol. 36, no. 8, p. R127, 2003.

[25] P. W. Anderson and H. Hasegawa, "Considerations on double exchange," *Physical Review*, vol. 100, no. 2, p. 675, 1955.

[26] P.-G. De Gennes, "Effects of double exchange in magnetic crystals," *Physical Review*, vol. 118, no. 1, p. 141, 1960.

[27] J. De Teresa, M. Ibarra, P. Algarabel, C. Ritter, *et al.*, "Evidence for magnetic polarons in the magnetoresistive perovskites," *Nature*, vol. 386, no. 6622, p. 256, 1997.

[28] T. Palstra, A. Ramirez, S. Cheong, B. Zegarski, P. Schiffer, and J. Zaanen, "Transport mechanisms in doped LaMnO3: Evidence for polaron formation," *Physical Review B*, vol. 56, no. 9, p. 5104, 1997.

[29] D. Worledge, G. J. Snyder, M. Beasley, T. Geballe, R. Hiskes, and S. DiCarolis, "Anneal-tunable Curie temperature and transport of La0.67Ca0.33MnO3," *Journal of Applied Physics*, vol. 80, no. 9, pp. 5158–5161, 1996.

[30] T. Kasuya, "Mobility of the antiferromagnetic large polaron," *Solid State Communications*, vol. 8, no. 20, pp. 1635–1638, 1970.

[31] P. Wagner, I. Gordon, L. Trappeniers, J. Vanacken, F. Herlach, V. Moshchalkov, and Y. Bruynseraede, "Spin dependent hopping and colossal negative magnetoresistance in epitaxial Nd 0.52 Sr 0.48 MnO 3 films in fields up to 50 T," *Physical Review Letters*, vol. 81, no. 18, p. 3980, 1998.

[32] M. Viret, L. Ranno, and J. D. Coey, “Magnetic localization in mixed-valence manganites,” *Physical Review B*, vol. 55, no. 13, p. 8067, 1997.

[33] S. Ravi and M. Kar, “Study of magneto-resistivity in La 1-x Ag x MnO 3 compounds,” *Physica B: Condensed Matter*, vol. 348, no. 1, pp. 169–176, 2004.

[34] H. Ahmed, S. Khan, W. Khan, R. Nongjai, and I. Khan, “Adiabatic to non adiabatic change in conduction mechanism of Zn doped La 0.67 Sr 0.33 MnO 3 perovskite,” *Journal of Alloys and Compounds*, vol. 563, pp. 12–17, 2013.

[35] G. J. Snyder, R. Hiskes, S. DiCarolis, M. Beasley, and T. Geballe, “Intrinsic electrical transport and magnetic properties of La 0.67 Ca 0.33 MnO 3 and La 0.67 Sr 0.33 MnO 3 MOCVD thin films and bulk material,” *Physical Review B*, vol. 53, no. 21, p. 14434, 1996.

[36] Y. Jia, L. Lu, K. Khazeni, D. Yen, C. Lee, and A. Zettl, “Pr-doping of the high-magnetoresistance perovskite Nd 2/3 Sr 1/3 MnO 3,” *Solid State Communications*, vol. 94, no. 11, pp. 917–920, 1995.

[37] M. Uehara and S.-W. Cheong, “Relaxation between charge order and ferromagnetism in manganites: Indication of structural phase separation,” *EPL (Europhysics Letters)*, vol. 52, no. 6, p. 674, 2000.

[38] S. Jin, T. H. Tiefel, M. McCormack, R. Fastnacht, R. Ramesh, L. Chen, *et al.*, “Thousandfold change in resistivity in magnetoresistive La-Ca-Mn-O films,” *Science-AAAS-Weekly Paper Edition-including Guide to Scientific Information*, vol. 264, no. 5157, pp. 413–414, 1994.

[39] H. Hwang, S. Cheong, N. Ong, and a. B. Batlogg, “Spin-polarized intergrain tunneling in La 2/3 Sr 1/3 MnO 3,” *Physical Review Letters*, vol. 77, no. 10, p. 2041, 1996.

[40] A. Gupta, G. Gong, G. Xiao, P. Duncombe, P. Lecoeur, P. Trouilloud, Y. Wang, V. Dravid, and J. Sun, “Grain-boundary effects on the magnetoresistance properties of perovskite manganite films,” *Physical Review B*, vol. 54, no. 22, p. R15629, 1996.

[41] B. Vengalis, G. Grigaliūnaitė-Vonsevičienė, A. Maneikis, J. Klimantavičius, R. Juškėnas, and K. Mažeika, “Low-field magnetoresistance and switching behavior of polycrystalline $La_{0.66}Sr_{0.34}MnO_3$ 3/ysz (001) films with columnar grain structure,” *Thin Solid Films*, vol. 625, pp. 42–48, 2017.

[42] J. Evetts, M. Blamire, N. Mathur, S. Isaac, B. Teo, L. Cohen, and

J. Macmanus-Driscoll, “Defect-induced spin disorder and magnetoresistance in single-crystal and polycrystal rare-earth manganite thin films,” *Philosophical Transactions-Royal Society of London Series A: Mathematical Physical and Engineering Sciences*, pp. 1593–1616, 1998.

[43] N. Mathur, G. Burnell, S. Isaac, T. Jackson, B. Teo, J. MacManus-Driscoll, L. Cohen, J. Evetts, and M. Blamire, “Large low-field magnetoresistance in La (0.7) Ca (0.3) MnO (3) induced by artificial grain boundaries,” *Nature*, vol. 387, no. 6630, p. 266, 1997.

[44] S. Lee, H. Hwang, B. I. Shraiman, I. WD Ratcliff, and S. Cheong, “Intergrain magnetoresistance via second-order tunneling in perovskite manganites,” *Physical Review Letters*, vol. 82, no. 22, p. 4508, 1999.

[45] N. Kozlova, K. Dörr, D. Eckert, T. Walter, and K.-H. Müller, “Intergrain magnetoresistance of La 0.7 Sr 0.3 MnO 3 in pulsed magnetic fields up to 50 T,” *Journal of Magnetism and Magnetic Materials*, vol. 261, no. 1, pp. 48–55, 2003.

[46] R. Gross, L. Alff, B. Büchner, B. Freitag, C. Höfener, J. Klein, Y. Lu, W. Mader, J. Philipp, M. Rao, *et al.*, “Physics of grain boundaries in the colossal magnetoresistance manganites,” *Journal of Magnetism and Magnetic Materials*, vol. 211, no. 1, pp. 150–159, 2000.

[47] L. Balcells, J. Fontcuberta, B. Martinez, and X. Obradors, “High-field magnetoresistance at interfaces in manganese perovskites,” *Physical Review B*, vol. 58, no. 22, p. R14697, 1998.

[48] N. Kozlova, T. Walter, K. Dörr, D. Eckert, A. Handstein, Y. Skourski, K.-H. Müller, and L. Schultz, “Intergrain magnetoresistance and resistance relaxation of La 0.7 Sr 0.3 MnO 3 thin films in pulsed magnetic fields up to 60T,” *Physica B: Condensed Matter*, vol. 346, pp. 74–78, 2004.

[49] P. Mandal, K. Bärner, L. Haupt, A. Poddar, R. Von Helmolt, A. Jansen, and P. Wyder, “High-field magnetotransport properties of La 2/3 Sr 1/3 MnO 3 and Nd 2/3 Sr 1/3 MnO 3 systems,” *Physical Review B*, vol. 57, no. 17, p. 10256, 1998.

[50] J. Coey, M. Viret, L. Ranno, and K. Ounadjela, “Electron localization in mixed-valence manganites,” *Physical Review Letters*, vol. 75, no. 21, p. 3910, 1995.

[51] E. Fatuzzo, “Theoretical considerations on the switching transient in ferroelectrics,” *Physical Review*, vol. 127, no. 6, p. 1999, 1962.

[52] N. Kozlova, K. Dörr, D. Eckert, A. Handstein, Y. Skourski, T. Walter, K.-H. Müller, and L. Schultz, “Slow relaxation of grain boundary resistance in a ferromagnetic manganite,” *Journal of Applied Physics*, vol. 93, no. 10, pp. 8325–8327, 2003.

[53] M. Ulrich, J. García-Otero, J. Rivas, and A. Bunde, “Slow relaxation in ferromagnetic nanoparticles: Indication of spin-glass behavior,” *Physical Review B*, vol. 67, no. 2, p. 024416, 2003.

[54] J. Phillips and J. Vandenberg, “Subensembles and kohlrausch relaxation in electronic and molecular glasses,” *Journal of Physics: Condensed Matter*, vol. 9, no. 18, p. L251, 1997.

[55] K. Trachenko and M. T. Dove, “Local events and stretched-exponential relaxation in glasses,” *Physical Review B*, vol. 70, no. 13, p. 132202, 2004.

[56] M. Hundley, M. Hawley, R. Heffner, Q. Jia, J. Neumeier, J. Tesmer, J. Thompson, and X. Wu, “Transport-magnetism correlations in the ferromagnetic oxide La0.7Ca0.3MnO3,” *Applied Physics Letters*, vol. 67, no. 6, pp. 860–862, 1995.

[57] V. Petrauskas, “Modelling of grain boundary resistance in thin films of lanthanum manganites,” *Lithuanian Journal of Physics and Technical Sciences*, vol. 46, pp. 191–198, 2006.

[58] J. Phillips, “Microscopic theory of atomic and electronic stretched exponential relaxation in high temperature superconductors,” *Physica C: Superconductivity*, vol. 340, no. 4, pp. 292–298, 2000.

[59] K. De, S. Das, A. Roy, P. Dhak, M. Willinger, J. Amaral, V. Amaral, S. Giri, S. Majumder, C. J. Silva, *et al.*, “Enhanced ferromagnetism and glassy state in phase separated La0.95Sr0.05MnO3+ δ,” *Journal of Applied Physics*, vol. 112, no. 10, p. 103907, 2012.

[60] J. Phillips, “Stretched exponential relaxation in molecular and electronic glasses,” *Reports on Progress in Physics*, vol. 59, no. 9, p. 1133, 1996.

[61] J. Vogel, J. Moritz, and O. Fruchart, “Nucleation of magnetisation reversal, from nanoparticles to bulk materials,” *Comptes Rendus Physique*, vol. 7, no. 9-10, pp. 977–987, 2006.

[62] M. Avrami, “Kinetics of phase change. II Transformation-time relations for random distribution of nuclei,” *The Journal of Chemical Physics*, vol. 8, no. 2, pp. 212–224, 1940.

[63] K. Daoudi, T. Tsuchiya, and T. Kumagai, “Growth and characterization

of epitaxial La 0.7 Ca 0.3 MnO 3 thin films by metal-organic deposition on (LaAlO 3) 0.3 (SrAlTaO 6) 0.7 substrates," *Thin Solid Films*, vol. 516, no. 18, pp. 6325–6329, 2008.

[64] L. Žurauskaitė, S. Balevičius, N. Žurauskienė, S. Keršulis, V. Stankevič, Č. Šimkevičius, J. Novickij, and S. Tolvaišienė, "Ageing effects on electrical resistivity and magnetoresistance of nanostructured manganite films," *Lithuanian Journal of Physics*, vol. 52, no. 3, 2012.

[65] M. Egilmez, M. Saber, M. Abdelhadi, K. Chow, and J. Jung, "Anomalous aging and strain induced time dependent phenomena in ultra-thin La 0.65 Ca 0.35 MnO 3 films," *Physics Letters A*, vol. 375, no. 45, pp. 4049–4052, 2011.

[66] R. Metz, "Electrical properties of NTC thermistors made of manganite ceramics of general spinel structure: Mn3- x- x′ MxNx′ O4 (0≤ x+ x′≤ 1; M and N being Ni, Co or Cu). Aging phenomenon study," *Journal of Materials Science*, vol. 35, no. 18, pp. 4705–4711, 2000.

[67] H. Klym, V. Balitska, O. Shpotyuk, and I. Hadzaman, "Degradation transformation in spinel-type functional thick-film ceramic materials," *Microelectronics Reliability*, vol. 54, no. 12, pp. 2843–2848, 2014.

[68] V. Balitska, B. Butkievich, O. Shpotyuk, and M. Vakiv, "On the analytical description of ageing kinetics in ceramic manganite-based NTC thermistors," *Microelectronics Reliability*, vol. 42, no. 12, pp. 2003–2007, 2002.

[69] M. Vakiv, O. Shpotyuk, V. Balitska, B. Butkiewicz, and L. Shpotyuk, "Ageing behavior of electrical resistance in manganite NTC ceramics," *Journal of the European Ceramic Society*, vol. 24, no. 6, pp. 1243–1246, 2004.

[70] E. Emelianova, P. Hertogen, V. Arkhipov, and G. Adriaenssens, "A model of photoinduced anisotropy in chalcogenide glasses," *Journal of Non-Crystalline Solids*, vol. 266, pp. 954–958, 2000.

[71] G. Williams and D. C. Watts, "Non-symmetrical dielectric relaxation behaviour arising from a simple empirical decay function," *Transactions of the Faraday society*, vol. 66, pp. 80–85, 1970.

[72] M. Potuzak, R. C. Welch, and J. C. Mauro, "Topological origin of stretched exponential relaxation in glass," *The Journal of Chemical Physics*, vol. 135, no. 21, p. 214502, 2011.

[73] A. Abrutis, V. Plausinaitiene, V. Kubilius, A. Teiserskis, Z. Saltyte, R. Butkute, and J. Senateur, "Magnetoresistant La 1-x Sr x MnO 3 films by

pulsed injection metal organic chemical vapor deposition: effect of deposition conditions, substrate material and film thickness," *Thin Solid Films*, vol. 413, no. 1, pp. 32–40, 2002.

[74] S. Balevičius, V. Stankevič, N. Žurauskienė, Č. Šimkevičius, O. Liebfried, M. Löffler, M. Schneider, A. Abrutis, and V. Plaušinaitienė, "Thin film manganite-metal interconnection and "loop effect" studies in cmr-based high magnetic field sensors," *Acta Physica Polonica A*, vol. 6, no. 115, pp. 1133–1135, 2009.

[75] O. Liebfried, M. Loffler, M. Schneider, S. Balevicius, V. Stankevic, N. Zurauskiene, A. Abrutis, and V. Plausinaitiene, "B-scalar measurements by CMR-based sensors of highly inhomogeneous transient magnetic fields," *IEEE Transactions on Magnetics*, vol. 45, no. 12, pp. 5301–5306, 2009.

[76] J. Novickij, R. Kačianauskas, A. Kačeniauskas, S. Balevičius, N. Žurauskienė, and V. Stankevič, "Axial magnetic field measurements of pulsed solenoids," *Elektronika IR Elektrotechnika*, vol. 51, no. 2, 2004.

[77] F. Herlach, G. Landwehr, G. M. N. M. D. Montgomery, and M. M. L. R. C. Schinkel, "Strong and ultrastrong magnetic fields," *Topics in Applied Physics*, vol. 57, 1985.

[78] M. Ziese, "Extrinsic magnetotransport phenomena in ferromagnetic oxides," *Reports on Progress in Physics*, vol. 65, no. 2, p. 143, 2002.

[79] J. Colino and A. De Andrés, "Huge magnetoresistance in ultrathin La0.7Ca0.3 MnO 3 films: The role of superparamagnetic clusters and domain walls," *Applied Physics Letters*, vol. 87, no. 14, p. 142509, 2005.

[80] P. Mandal, P. Choudhury, K. Bärner, R. von Helmolt, and A. Jansen, "Magnetotransport properties of La 2/3 Sr 1/3 MnO 3 thin film," *Journal of Applied Physics*, vol. 91, no. 9, pp. 5940–5944, 2002.

[81] A. C. Jones and M. L. Hitchman, *Chemical vapour deposition: precursors, processes and applications.* Royal Society of Chemistry, 2009.

[82] P. Lu, H. Li, S. Sun, and B. Tuttle, "Novel single-solid-source metalorganic chemical vapor processing of PT and PZT thin films," *Journal of Crystal Growth*, vol. 171, no. 3-4, pp. 453–457, 1997.

[83] A. Bartasyte, R. Bouregba, E. Dogheche, M. Boudard, G. Poullain, O. Chaix-Pluchery, C. Jimenez, V. Plausinaitiene, D. Remiens, A. Abrutis, *et al.*, "Ferroelectric PbTiO 3 films grown by pulsed liquid injection MOCVD," *Surface and Coatings Technology*, vol. 201, no. 22, pp. 9340–

9344, 2007.

[84] J. Macdonald and J. Phillips, "Topological derivation of shape exponents for stretched exponential relaxation," *The Journal of Chemical Physics*, vol. 122, no. 7, p. 074510, 2005.

[85] E. Dagotto, S. Yunoki, C. Şen, G. Alvarez, and A. Moreo, "Recent developments in the theoretical study of phase separation in manganites and underdoped cuprates," *Journal of Physics: Condensed Matter*, vol. 20, no. 43, p. 434224, 2008.

[86] M. Czapkiewicz, T. Stobiecki, and S. van Dijken, "Thermally activated magnetization reversal in exchange-biased [Pt/ Co] 3/ Pt/ Ir Mn multilayers," *Physical Review B*, vol. 77, no. 2, p. 024416, 2008.

[87] M. Labrune, S. Andrieu, F. Rio, and P. Bernstein, "Time dependence of the magnetization process of RE-TM alloys," *Journal of Magnetism and Magnetic Materials*, vol. 80, no. 2-3, pp. 211–218, 1989.

[88] V. H. Crespi, L. L. Y. Jia, K. Khazeni, A. Zettl, and M. L. Cohen, "Thermopower of single-crystal Nd 1-x (Sr, Pb) x MnO 3-δ," *Physical Review B*, vol. 53, no. 21, p. 14303, 1996.

[89] S. R. Bakaul, B. Miao, W. Lin, W. Hu, A. David, H. Ding, and T. Wu, "Domain-related origin of magnetic relaxation in compressively strained manganite thin films," *Applied Physics Letters*, vol. 101, no. 1, p. 012408, 2012.

[90] R. Cowburn, J. Ferré, S. Gray, and J. Bland, "Domain-wall dynamics, pinning, and nucleation in ultrathin epitaxial Fe films," *Physical Review B*, vol. 58, no. 17, p. 11507, 1998.

[91] F. Kohlrausch, "Experimental-untersuchungen über die elastische nachwirkung bei der torsion, ausdehnung und biegung," *Annalen der Physik*, vol. 234, no. 7, pp. 337–375, 1876.

[92] V. Prokhorov, G. Kaminsky, V. Komashko, Y. Lee, J. Park, and H. Ri, "Oxygen-deficiency-activated phase transition in a long-aged La 0.8 Sr 0.2 MnO 3 film," *Applied Physics Letters*, vol. 80, no. 15, pp. 2707–2709, 2002.

[93] J. Mira, J. Rivas, M. Breijo, M. S. Rodrıguez, and R. Sánchez, "Effects of aging on the electrical resistivity of La 1-x B x CoO 3 perovskites (B= Sr, Ca, Ba; 0.20$\leq$ x$\leq$ 0.30)," *Sensors and Actuators A: Physical*, vol. 81, no. 1, pp. 23–26, 2000.

[94] N. Abdelmoula, K. Guidara, A. Cheikh-Rouhou, E. Dhahri, and J. Joubert,

"Effects of the oxygen nonstoichiometry on the physical properties of $La_{0.7}Sr_{0.3}MnO_{3-\delta}$ manganites ($0\leq \delta\leq 0.15$)," *Journal of Solid State Chemistry*, vol. 151, no. 1, pp. 139–144, 2000.

[95] R. De Souza, J. Kilner, and J. Walker, "A SIMS study of oxygen tracer diffusion and surface exchange in $La_{0.8}Sr_{0.2}MnO_{3+\delta}$," *Materials Letters*, vol. 43, no. 1, pp. 43–52, 2000.

[96] A. M. Saranya, D. Pla, A. Morata, A. Cavallaro, J. Canales-Vázquez, J. A. Kilner, M. Burriel, and A. Tarancón, "Engineering mixed ionic electronic conduction in $La_{0.8}Sr_{0.2}MnO_{3+\delta}$ nanostructures through fast grain boundary oxygen diffusivity," *Advanced Energy Materials*, vol. 5, no. 11, 2015.

[97] N. Žurauskienė, S. Balevičius, P. Cimmperman, V. Stankevič, S. Keršulis, J. Novickij, A. Abrutis, and V. Plaušinaitienė, "Colossal magnetoresistance properties of $La_{0.83}Sr_{0.17}MnO_3$ thin films grown by mocvd on lucalox substrate," *Journal of Low Temperature Physics*, vol. 159, no. 1-2, pp. 64–67, 2010.

[98] B. Belevtsev, V. Krasovitsky, D. Naugle, K. Rathnayaka, A. Parasiris, S. Surthi, R. Pandey, and M. Rom, "Transport and magnetic anisotropy in cmr thin film $La_{1-x}Ca_xMnO_3$ ($x \approx 1/3$) induced by a film-substrate interaction," *ArXiv Preprint cond-mat/0103493*, 2001.

[99] M. Takemoto, K. Yamagiwa, Y. Umeshita, and H. Ikawa, "Magnetoresistance of Manganite Ceramics Sintered with SiO2 as Additive," in *Key Engineering Materials*, vol. 216, pp. 145–148, Trans Tech Publ, 2002.

[100] V. Uskoković, A. Košak, and M. Drofenik, "Silica-coated lanthanum–strontium manganites for hyperthermia treatments," *Materials Letters*, vol. 60, no. 21, pp. 2620–2622, 2006.

[101] R. Ghodssi and P. Lin, *MEMS materials and processes handbook*, vol. 1. Springer Science & Business Media, 2011.

Publications by the Author

Periodic

P1. N. Žurauskienė, S. Balevičius, D. Pavilonis, V. Stankevič, S. Keršulis, J. Novickij (2013) Magnetoresistance Relaxation in Thin La-Sr-Mn-O Films Exposed to High-Pulsed Magnetic Fields, IEEE Transactions on Plasma Science, VOL. 41, NO. 10: 2830-2835.

P2. N. Žurauskienė, S. Balevičius, D. Pavilonis, V. Stankevič, V. Plaušinaitienė, S. Zherlitsyn, T. Herrmannsdörfer, J. M. Law, J. Wosnitza (2014) Magnetoresistance and Resistance Relaxation of Nanostructured La-Ca-MnO Films in Pulsed Magnetic Fields, IEEE Transactions on Magnetics, VOL. 50, NO. 11: 1-4

P3. D. Pavilonis, N. Žurauskienė (2014) Slow relaxation of resistance in nanostructured $La_{0.83}Sr_{0.17}MnO_3$ films induced by pulsed magnetic fields, Lithuanian Journal of Physics, VOL. 54: 37–40.

P4. V. Stankevič, Č. Šimkevičius, S. Keršulis, S. Balevičius, N. Žurauskienė, D. Pavilonis, S. Tolvaišienė (2015) Improvement in the long-term stability of parameters of encapsulated magnetic field sensors based on La-Sr-Mn-O thin films. Sensors and Actuators A, VOL. 228: 112–117.

P5. Č. Šimkevičius, S. Keršulis, V. Stankevič, D. Pavilonis, N. Žurauskienė, S. Balevičius, S. Tolvaišienė (2015) Accelerated ageing effects in nanostructured $La_{0.83}Sr_{0.17}MnO_3$ films. Thin Solid Films, VOL. 589: 331–337.

P6. N. Žurauskienė, D. Pavilonis, S. Balevičius, V. Stankevič, A. Maneikis, V. Plaušinaitienė, J. Novickij (2015) Fast Resistance Relaxation in Nanostructured La-Ca-Mn-O Films in Pulsed Magnetic Fields. IEEE Transactions on Plasma Science, VOL. 43 NO. 10: 3445-3450.

P7. N. Žurauskienė, D. Pavilonis, J. Klimantavičius, S. Balevičius, V. Stankevič, R. Vasiliauskas, V. Plaušinaitienė, A. Abrutis, M. Skapas, R. Juškėnas (2017) Magnetoresistance Relaxation Anisotropy of Nanostructured La-Sr(Ca)-Mn-O Films Induced by High-Pulsed Magnetic Fields. IEEE Transactions on Plasma Science, VOL. 45 NO. 10: 2773-2779.

P8. N. Žurauskienė, D. Pavilonis, J. Klimantavičius, S. Balevičius, V. Stankevič, S.Keršulis, V. Plaušinaitienė, A. Abrutis, R. Lukošė, M. Skapas, R. Juškėnas, B. Knašienė, E. Naujalis, J. M. Law (2017) Influence of MOCVD Growth Pressure on Magnetoresistance of Nanostructured La-Ca-Mn-O Films Used for Magnetic Field Sensors. IEEE Transactions on Plasma Science, VOL. 45 NO. 10: 2780-2786.

Peer reviewed conference publications

PC1. N. Žurauskienė, S. Balevičius, D. Pavilonis, V. Stankevič, S. Keršulis, J. Novickij, Magnetoresistance Relaxation in Thin La-Sr-Mn-O Films Exposed to High Pulsed Magnetic Fields, 4th Euro-Asian Pulsed Power Conf. / 19th Intern. Conf. on High-Power Particle Beams, Karlsruhe, Germany, Sept. 30–Oct. 4, 2012 : EAPPC 2012/BEAMS 2012 / Proceedings, pp. 181-1-4, 2012.

PC2. N. Žurauskienė, S. Balevičius, D. Pavilonis, V. Stankevič, V. Plaušinaitienė, Sergei Zherlitsyn, Thomas Herrmannsdoerfer, Joseph Law, Joachim Wosnitza (2014) Magnetoresistance and Resistance Relaxation of Nanostructured La-Ca-MnO Films in Pulsed Magnetic Fields,IEEE International magnetic conference INTERMAG-2014 Digest Book: 1568-1569.

Summary in Lithuanian (Santrauka)

Polikristaliniai La-Sr(Ca)-Mn-O manganitų sluoksniai, pasižymintys milžiniškos magnetovaržos (CMR) reiškiniu yra perspektyvūs, kuriant stipraus impulsinio magnetinio lauko matuoklius. Jie turi pasižymėti pakankamu jautriu plačiame magnetinių laukų ruože (0,1–100 T) bei didele sparta (dešimčių kHz dažnių ruožas). Todėl svarbu išsiaiškinti, kaip polikristalinių (nanostruktūrizuotų) manganitų sluoksnių cheminė sudėtis ir nevienalytė struktūra lemia magnetovaržos dydį (jutiklio jautrumą) plačiame temperatūrų ir magnetinių laukų ruože, bei ištirti magnetovaržos atminties efektus, kurie riboja matuoklio spartą. Šio darbo tikslas – ištirti magnetovaržos ir elektrinės varžos relaksacijos reiškinius nanostruktūrizuotuose La-Sr(Ca)-Mn-O manganitų sluoksniuose, išsiaiškinti juos lemiančius mechanizmus ir nustatyti pagrindines sluoksnių savybes, tinkamas sparčių magnetinio lauko jutiklių, veikiančių kambario bei kriogeninių temperatūrų ruožuose, kūrimui.

Disertacinio darbo metu buvo nustatyta, kad nanostruktūrizuotų manganitų sluoksnių magnetovarža ženkliai priklauso nuo sluoksnių morfologijos ir cheminės sudėties ir plačiame magnetinių laukų bei temperatūrų ruože gali būti aprašoma, naudojant modifikuotą Mott'o šuolinio laidumo modelį, įskaitant kristalitų ir tarpkristalitinių sričių įnašus. Darbe parodyta, kad pasibaigus magnetinio lauko impulsui, stebimas elektrinės sluoksnio varžos atsistatymo į pradinę vertę procesas, kurio metu galima išskirti dviejų skirtingų trukmių ruožus: „greitąją“ ($\sim 100\,\mu$s) ir „lėtąją“ ($\geqslant$ 1 ms) relaksaciją. Buvo nustatyti nanostruktūrizuotų manganitų sluoksnių „greitosios“ ir „lėtosios“ varžos relaksacijos procesų komponenčių charakteringųjų laiko konstantų ir santykinės liekamosios varžos verčių kitimo dėsningumai plačiame temperatūrų ir magnetinių laukų ruože. Parodyta, kad „greitoji“ relaksacijos proceso komponentė yra gerai aprašoma Kolmogorov-Avrami-Fatuzzo modeliu su suspaustąja eksponente, ir dominuojantis šios relaksacijos mechanizmas yra magnetinių domenų užuomazgų susiformavimas ir persiorientavimas į pusiausvyrinę būseną. Tuo tarpu „lėtoji“ magnetinės relaksacijos proceso komponentė yra gerai aprašoma Kohlrausch-Williams-Watts modeliu su ištemptąja eksponente, nagrinėjant magnetinių momentų sąveiką netvarkiose tarpkristalitinėse srityse.

Remiantis gautais tyrimų rezultatais buvo pasiūlyti impulsinio magnetinio lauko jutikliai, veikiantys kambario bei kriogeninių temperatūrų ruožuose. Nustatyta, kad aukštų temperatūrų ruožui yra perspektyvūs nanostruktūrizuoti La-Sr-Mn-O sluoksniai, tuo tarpu kriogeninėse temperatūrose yra tinkamesni La-Ca-Mn-O sluoksniai, pasižymintys didesne magnetovarža ir mažesnėmis liekamosios varžos vertėmis žemose temperatūrose. Magnetinės relaksacijos tyrimų rezultatai leido įvertinti galimus impulsinio magnetinio lauko jutiklių veikimo laiko ruožus: matuojant ilgesnės nei milisekundė trukmės impulsus, „greitoji“ relaksacijos komponentė neturi įtakos matavimo tikslumui, tuo tarpu „lėtąją“ komponentę, pasireiškiančią milisekundžių trukmių ruože, galima sumažinti daugiau nei du kartus, naudojant La-Ca-Mn-O sluoksnius su aukštesne fazinio virsmo temperatūra.

Taip pat disertaciniame darbe buvo tiriami nanostruktūrizuotų manganitų sluoksnių senėjimo laikui bėgant procesai ir ieškoma būdų, kaip stabilizuoti šių sluoksnių pagrindinius parametrus. Parodyta, kad tokių sluoksnių atkaitinimas argono dujų atmosferoje 100–200 °C temperatūrose pagreitina sluoksnių senėjimo procesą ir stabilizuoja jų varžą bei magnetovaržą. Nustatyta, kad sluoksnių padengimas specialia pasyvuojančia medžiaga - karštojo lydymo klijais - pagreitina sendinimo procesą beveik tris kartus. Parodyta, kad varžos kinetiką sluoksnių senėjimo proceso metu gerai aprašo hierarchiškai apribotos relaksacinės dinamikos modelis su ištemptąja eksponente, o žymų varžos padidėjimą galima paaiškinti dėl atkaitinimo vykstančiu deguonies koncentracijos sumažėjimu ir difuzija tarpkristalitinėse sluoksnių srityse.

Disertacijos tema yra atspausdinti aštuoni moksliniai straipsniai žurnaluose, įtrauktuose į *Thomson Reuters Web of Science* duomenų bazę, ir du straipsniai tarptautinių konferencijų medžiagoje. Disertacijoje atliktų mokslinių tyrimų rezultatai buvo pristatyti septyniose mokslinėse konferencijose Lietuvoje ir užsienyje.